



Enhancing the Light Output of Solid State Emitters

Christopher Stephen Woodhead

Department of Physics

Lancaster University

25 October 2017

This thesis is submitted in partial fulfilment of the requirements for the degree of Doctor of Philosophy

Preface

This thesis is the result of work which I performed at Lancaster University, between October 2013 and August 2017. Except where otherwise stated the contents of this thesis is the result of my own work, and is not the same as any others I have already submitted, or in the process of submitting, for any degree at any university or institution. The word count on this thesis does not exceed the maximum limit of 80,000 words.

A handwritten signature in black ink, reading "C. S. Woodhead". The signature is written in a cursive style with a long, sweeping underline that ends in a small arrowhead pointing to the right.

C. S. Woodhead
Wednesday, 25 October 2017

*“The road goes ever on and on,
Out from the door where it began.
Still round the corner there may wait,
A new road or a secret gate,
And though I oft have passed them by,
A day will come at last when I,
Shall take the hidden paths that run,
West of the Moon, East of the Sun.”*

JRR Tolkien

Acknowledgements

Throughout my four years as a PhD student I have had the opportunity to work with a wide range of people, without many of whom, this thesis would not have been possible. The most important of which is my supervisor Robert Young, who has been one of the best supervisors that a student could ask for. Thank you, Rob, for letting me be a part of your research, and be a member of the ever-growing family which is your research group.

I would like to thank the collaborators that made Chapter 5 possible by growing the samples and performing some of the initial measurements; these include Jonathan Orchard, David Mowbray, Jian Wu, Mingchu Tang, Richard Beanland and Huiyun Liu. A big thank you especially to Jonathan and David for developing and organising the project. In the same vein, I would also like to thank the collaborators that made Chapter 4 possible including Robert Young, E. P Smakman, and Manus Hayne, who all helped in either the growth or cross-sectional imaging of the QRs. However, my biggest thank you for this chapter goes to Matt Young, who I worked with closely throughout this project. I wish you all the luck for the future Matt, and I hope one day to sit in a pub drinking an ale that you have masterfully brewed.

I would also like to extend my thanks to the amazing technical staff at Lancaster, who's hard work and friendly attitude helps to make the research that we do here truly special. I especially would like to thank Graham Chapman from the mechanical workshop, who has spent many hours designing and building my SIL mounting devices, as well as numerous smaller jobs that have been essential to obtaining the results included in this thesis.

My fellow group members also require recognition, so my thanks also extend to Yasir Noori, Jonathan Roberts, Ramon Bernardo-Gavito, Yameng Cao and Alex Robson. Your support and assistance in the lab, combined with your friendship outside the lab have been invaluable. I would also like to thank my past housemates Marcin Szyniszewski, Matt Wilkinson and Hannah Jenkins for all your support.

No acknowledgement is complete without mentioning my friends and family, who have kept me sane for these last 4 years. Thanks to my closest friends Michael Lindsay, Laura Hodgkinson and Ingrida Semenec; for cheering my weekends up, and being part of some wonderful adventures. I look forward to many more adventures in the future.

Last but certainly not least, the most important dedication goes to my family. Any attempt to express my gratitude in writing to you would be utterly incomplete, so I will end with simply saying that I love you all and this thesis is dedicated to you.

List of Publications

Y. Cao, A.J. Robson, A. Alharbi, J. Roberts, **C. Woodhead**, Y. Noori, R. Bernardo Gavito, D. Shahrjerdi, U. Roedig, I. E. Bagci, V. Falko and R.J. Young, “*Optical identification using imperfections in 2D materials*”, arXiv.org. 1706.07949 (Submitted to 2D materials June 2017).

R. Bernardo Gavito, I.E. Bagci, J. Roberts, J. Sexton, B. Astbury, H. Shokeir, T. Mcgrath, Y. Noori, **C. Woodhead**, M. Missous, U. Roedig, R.J. Young, “*Extracting random numbers from quantum tunnelling through a single diode*”, arXiv:1706.07348 (Submitted to Nature electronics June 2017).

J. R. Orchard, **C. Woodhead**, J. Wu, M. Tang, R. Beanland, Y. Noori, H. Liu, R.J. Young, D.J. Mowbray, “*Silicon-based Single Quantum Dot Emission in the Telecoms C-band*”, *ACS Photonics* **4**, 1740-1746, (2017).

C. S. Woodhead, J. Roberts, Y. J. Noori, Y. Cao, R. Bernado-Gavito, P. Tovee, A. Kozikov, K. Novoselov and R. J. Young, “*Direct Light Extraction from 2D Materials Using Liquid Formed Microlenses*”, *2D Materials* **4**, 015032, (2017).

Y. J. Noori, Y. Cao, J. Roberts, **C. S. Woodhead**, R. Bernado-Gavito, P. Tovee and R. J. Young, “*Photonic Crystals for Enhanced Light Extraction from 2D Materials*”, *ACS Photonics* , **3**, 2515-2520, (2016).

J. Orchard, **C. Woodhead**, S. Shutts, J. Wu, A. Sobiesierski, R.J. Young, R. Beanland, H. Liu, P. Smowton, P. D. Mowbray, “*Analysing radiative and non-radiative recombination in InAs quantum dots grown on Si substrates for integrated laser applications*”, *Proceedings of SPIE*. 9758, 975809, 7, (2016).

J. Roberts, I. E. Bagci, M. A. M. Zawawi, J. Sexton, N. Hulbert, Y. J. Noori, M. P. Young, **C. S. Woodhead**, M. Missous, M. A. Migliorato, U. Roedig and R. J. Young, “*Atomic-scale Authentication with Resonant Tunneling Diodes*”, *MRS Advances*, **5** (2016).

J. Roberts, I. E. Bagci, M. A. M. Zawawi, J. Sexton, N. Hulbert, Y. J. Noori, M. P. Young, **C. S. Woodhead**, M. Missous, M. A. Migliorato, U. Roedig and R. J. Young, “*Using Quantum Confinement to Uniquely Identify Devices*”, *Scientific Reports*, 16456 (2015).

M. P. Young, **C. S. Woodhead**, J. Roberts, Y. J. Noori, M. T. Noble, A. Krier, E. P. Smakman, P. M. Koenraad, M. Hayne and R. J. Young, “*Photoluminescence Studies of Individual and Few GaSb/GaAs Quantum Rings*”, *AIP Advances*, **4**, 117127 (2014).

Abstract

The work in this thesis focuses on improving the light output of room temperature emitting materials, and nanostructures as a stepping stone for use as single photon sources.

The primary nanostructures studied are III-V based type-II emitting quantum dots/quantum rings (QDs/QR's), which emit at telecom wavelengths either in the O-band (GaSb/GaAs QRs) or the C-band (InAs/GaAs QDs capped with GaAsSb). Individual exciton emission at low temperature was observed in these samples using micro-photoluminescence for what we believe is the first time. This was achieved by reducing the excitation area of the sample using micropillars and gold aperture masks, combined with increasing the extraction efficiency of light using a solid immersion lens. The observation of individual exciton emission enabled their contribution to the power dependent blueshift of type-II quantum dots to be studied.

The integration of the InAs/GaAs QDs with silicon was explored by studying their emission when they are grown on both GaAs and silicon substrates. Studies such as this are an important step towards integrating QDs with on-chip communications.

Finally, solid immersion lenses formed from a UV-curable epoxy are explored as a method for increasing light out of 2D materials. It was found that for Tungsten Diselenide (WSe_2) the solid immersion lens increased the intensity of the emitted photoluminescence, as well as preventing the monolayer from degrading. This method could prove to be an excellent method for increasing the light output of 2D material based LED's, especially WSe_2 based single photon sources.

Table of Contents

Preface.....	ii
Acknowledgements.....	iv
List of Publications.....	v
Abstract.....	vi
1 Chapter 1.....	1-1
1.1 Quantum and Classical light.....	1-1
1.2 Single photons.....	1-1
1.2.1 Types of single photon sources.....	1-2
1.3 Thesis Outline.....	1-3
1.4 References.....	1-5
2 Chapter 2.....	2-1
2.1 Semiconductor background.....	2-1
2.1.1 Introduction to semiconductor bands.....	2-1
2.1.2 Fermi-Dirac distribution.....	2-2
2.1.3 Direct and indirect semiconductors.....	2-3
2.2 Artificial Atoms.....	2-5
2.2.1 Excitons.....	2-5
2.2.2 Excitonic Confinement.....	2-7
2.2.3 Quantum dots.....	2-8
2.2.4 Properties of Type-II QDs.....	2-9
2.2.5 Quantum Yield.....	2-10
2.3 Light emitting 2D materials.....	2-10
2.3.1 Properties of TMD's.....	2-11
Enhancing light.....	2-12
2.3.2 The Solid Immersion Lens.....	2-12
2.3.3 Purcell Effect.....	2-15

2.3.4	Plasmonic enhancement	2-16
2.4	References	2-17
3	Chapter 3	3-1
3.1	Optical Spectroscopy	3-1
3.1.1	Photoluminescence	3-1
3.1.2	Raman Spectroscopy	3-3
3.2	Fabrication	3-3
3.2.1	Exfoliation of 2D materials	3-3
3.2.2	Fabricating epoxy SILs	3-3
3.2.3	Electron Beam Lithography	3-5
3.2.4	Plasma Etching	3-6
3.2.5	Deposition	3-6
3.3	Imaging techniques	3-7
3.3.1	Scanning Electron Microscope (SEM)	3-7
3.3.2	Scanning Probe Microscopy (SPM)	3-8
3.4	References	3-10
4	Chapter 4	4-1
4.1	Introduction	4-1
4.2	Isolating individual Quantum rings	4-3
4.2.1	Modifying the sample surface	4-4
4.2.2	μ PL Results	4-7
4.3	Power dependent blueshift	4-8
4.4	Conclusions	4-12
4.5	References	4-13
5	Chapter 5	5-1
5.1	Introduction	5-1
5.2	Sample structure details	5-3
5.3	Macro- PL results	5-4
5.4	Isolating individual dots	5-6

5.4.1	Micropillars.....	5-6
5.4.2	Apertures.....	5-7
5.4.3	Power Dependence	5-9
5.5	Conclusion.....	5-11
5.6	References.....	5-12
6	Chapter 6.....	6-1
6.1	Introduction.....	6-1
6.2	Fabricating SILs onto different surfaces.....	6-2
6.2.1	Embedded GaSb/GaAs Quantum rings.....	6-2
6.2.2	Delicate surfaces.....	6-3
6.3	Fabricating SILs onto 2D materials.....	6-5
6.3.1	Enhancement of a Tungsten Diselenide (WSe ₂) monolayer	6-7
6.3.2	Resolution Enhancement and stability.....	6-8
6.3.3	Photoluminescence enhancement.....	6-11
6.3.4	Issues with Molybdenum Disulphide (MoS ₂)	6-12
6.3.5	Increase in longevity	6-14
6.4	Conclusions.....	6-14
6.5	Further work.....	6-16
6.5.1	Increasing the emission of 2D materials.....	6-16
6.5.2	Etching TMD's.....	6-20
6.6	References.....	6-24
7	Chapter 7.....	7-1
7.1	Conclusions.....	7-1
7.2	References.....	7-5
8	Glossary of terms/abbreviations.....	8-1

Chapter 1

Introduction

1.1 Quantum and Classical light

Technologies involving the generation of light are becoming increasingly important in our everyday lives. We rely on telecom lasers to transfer our data, when we want to access the internet^{1,2}, energy efficient LEDs to light our homes^{3,4} and recently organic/2D materials are enabling ultra-thin flexible LED's and smart phone screens^{5,6}. All these examples are classical light sources; they emit a large number of photons which can be considered as a classical wave, with a higher intensity corresponding to the square of the amplitude of the wave increasing.

Quantum light sources by contrast are sources that can emit photons in a controlled way such that the individual particle-like nature of the photon becomes observable. This can lead to many interesting effects that arise from being in a quantum state such as superposition and entanglement. Many of these effects have interesting future applications in quantum information processing with revolutionary technologies such as quantum computing⁷⁻⁹, and quantum cryptography^{10,11} recently receiving heavy research interest¹². Quantum cryptography is an especially important application as schemes such as quantum key distribution (QKD) can help to make communication 100% secure¹³, which is a step towards reducing cybercrime. At the time of writing, the previous year (2016) showed a record 40% increase in data breaches in the USA alone¹⁴, with 2017 being already on-track to surpass it¹⁵. As a result, the worldwide spending on digital security software and services for that year was estimated at over \$73.7 billion, and is expected to rise to \$90 billion by 2018. Quantum cryptography can help to play a role in reducing this expenditure, making it an important technology to develop.

1.2 Single photons

An efficient single photon source (SPS), i.e. a light source that can produce a stream of individual, and indistinguishable particles of light one at a time; is essential for quantum cryptography applications such as QKD. These are relatively more difficult to create compared to a classical light

source; and to be successfully used in an application like QKD several requirements must be met. The first is that a SPS is deterministic, producing an on-demand series of photons in an easily controllable manner. A true single photon source when prompted by the user should also have a 100% chance of outputting a single photon but a 0% chance of producing either multiple photons or no photons. Another requirement is that every photon is indistinguishable from the next, allowing quantum interference between two or more photons to occur^{16,17}. For any useful implementation of QKD, it is essential for the SPS to have a high photon repetition rate, hence allowing high key distribution bit rates, even at large distances where bit losses are inevitable.

As well as the primary requirements for a SPS discussed above there are other factors that must be considered to enable their large-scale implementation, such as the cost and size. A SPS that operates at low temperatures for example will inevitably be expensive and bulky due to it requiring a dedicated cooling system. A less perfect single photon source which can operate at room temperatures may in some implementations become a more viable alternative. The compatibility of the SPS with silicon and telecom fibres is also important to enable integration into modern communication systems. A silicon based SPS operating at telecoms wavelengths is easy to manufacture due to how established the silicon industry is, and would as a result remove multiple market barriers for QKD and other quantum information based technologies.

Single photon sources are not just valuable for quantum information processing. They are important in metrology enabling better standards of detectors, and enhancements in optical measurements¹⁸. They are also useful for low light sensing in fields such as surveillance, medical imaging and astronomy¹⁹. Additionally, entangled photons can create interference patterns with resolution higher than the diffraction limit of classical light, enabling super-resolution imaging and lithography^{20,21}.

1.2.1 Types of single photon sources

The most common, and arguably the easiest way to create a SPS is by attenuating a pulsed laser beam sufficiently, so that on average the number of photons in the pulse is < 1 . This has the advantage of being very cheap and easy to manufacture. However, because the emission characteristics of an attenuated laser pulse exhibits a Poissonian distribution, there is a probability that a prompted pulse of light will contain more than one photon or no photons. In applications like QKD this is often unacceptable as a pulse having more than one photon makes the scheme vulnerable to number splitting attacks²². This limitation can be overcome using decoy states, and attenuating the laser beam more heavily, however both of these methods significantly reduce the bit-rate. Lasers can also be used in parametric down conversion to create 2 photons, with one

photon being measured to herald the existence of the other. However, this also suffers from low bit rates due to a low generation efficiency and large losses.²³

An ideal source of single photons would be a single trapped atom; however this is a fairly impractical SPS to commercialise due to the cost, and complexity involved in building and operating an atom trap²⁴. The emission of a two-level system, with significant confinement of electrons could be considered an “artificial atom.” In a semiconductor, these atom-like optical conditions can be created by growing what is known as a Quantum dot (QD)²⁵. Quantum dots have thus received significant research interest and InAs QDs especially have been shown to be very effective single photon emitters²⁵⁻²⁹. However, these QDs only emit at low temperature, meaning that any practical single photon source using these requires a cryostat. Furthermore, they are not easily integrated into silicon and they do not emit at typical telecoms wavelengths. Therefore, growing and isolating room temperature emitting QDs, that can operate at telecoms wavelengths and are easily integrated into silicon is an important avenue of research.

1.3 Thesis Outline

The work in this thesis focuses on improving the light emission of QDs and other QD-like emitting nanostructures that are capable of emitting at room temperature, as a stepping stone for use as single photon sources.

It starts by studying a room temperature telecoms emitter (GaSb/GaAs QDs), and attempts to isolate individual excitons at low temperature. The thesis then looks at how InAs/GaAs QD based room temperature emitters, can be grown on silicon substrates, for better integration with silicon electronics. Finally, techniques for increasing the coupling of light into a system are explored using epoxy based solid immersion lenses. Increasing the internal efficiency of these emitters is also discussed in the further works section. The chapters covering these topics are outlined below:

Chapter 2 introduces some of the general background to semiconductor physics, including 2D materials and exciton confining structures called Quantum dots (QD). The differences between type-I and a type-II QDs are presented, and the possible mechanisms behind the power dependent blue shift observed in a type-II QDs spectra discussed. This chapter finally gives details on how light out of these semiconductors can be enhanced.

Chapter 3 provides information on the different methods used for testing these semiconductors. The methods used to detect light emission, and image the surface of these samples are presented, along with information on their fabrication. Additionally, the fabrication of epoxy solid immersion lenses (SILs) onto 2D materials performed in chapter 6 is presented in this chapter.

Chapter 4 introduces GaSb/GaAs Quantum Ring's (QRs), which are toroidal shaped QDs that emit in the telecoms O-band (1260-1360 nm). We use micro-photoluminescence combined with a glass SIL and a gold aperture mask to reduce the excitation/emission area and increase the collected light, enabling the observation of individual exciton emissions from the QRs. The individual exciton lines observed were then used to gain a better understanding of the power dependent blueshift observed in their macro-photoluminescence spectra.

Chapter 5 introduces another type-II QD system, composed of InAs/GaAs QDs capped with GaAsSb. These samples emitting in the telecoms C-band (1530-1565 nm), and can be grown on silicon substrates making them ideal for on-chip telecoms. The effectiveness of the growth on silicon was analysed by comparing the active regions emission to that of identically grown QDs on a GaAs substrate. Individual excitons were isolated using micropillars, and their contribution to the power dependent type-II blueshift was analysed.

Chapter 6 introduces a set of 2D materials which emit light called transition metal dichalcogenides (TMDs). A novel approach involving epoxy based liquid formed SILs is used to increase the light extraction from these materials. These SILs were fabricated on-top of a flake containing a monolayer of WSe₂ a TMD material known to show single photon emission³⁰. Photoluminescence maps showing the enhancement of light emission due to the epoxy are presented, and the impact of the SIL on the monolayers rate of degradation explored. It then goes on to explore preliminary work involving plasmonic structures and selective dry etching method, that can be used in conjunction with the SIL to enhance 2D materials.

Finally, chapter 7 concludes this work by summarising the results obtained in the previous chapters and highlights future directions of research for each emitter.

1.4 References

- 1 Renner, D. Long-wavelength semiconductor lasers. *IEEE J. Quantum Electron.* **23**, 641-641, (1987).
- 2 Arafin, S., Morrison, G. B., Mashanovitch, M. L., Johansson, L. A. & Coldren, L. A. Compact Low-Power Consumption Single-Mode Coupled Cavity Lasers. *IEEE Journal of Selected Topics in Quantum Electronics* **23**, 1-9, (2017).
- 3 Anikeeva, P. O., Halpert, J. E., Bawendi, M. G. & Bulović, V. Quantum Dot Light-Emitting Devices with Electroluminescence Tunable over the Entire Visible Spectrum. *Nano Letters* **9**, 2532-2536, (2009).
- 4 Shirasaki, Y., Supran, G. J., Bawendi, M. G. & Bulovic, V. Emergence of colloidal quantum-dot light-emitting technologies. *Nat Photon* **7**, 13-23, (2013).
- 5 Ahn, J.-H. & Hong, B. H. Graphene for displays that bend. *Nat Nano* **9**, 737-738, (2014).
- 6 Han, T.-H. *et al.* Extremely efficient flexible organic light-emitting diodes with modified graphene anode. *Nat Photon* **6**, 105-110, (2012).
- 7 Kok, P. *et al.* in *Rev. Mod. Phys.* Vol. 79 135-174 (2007).
- 8 Rae, A. I. M. *Quantum mechanics*. 5th ed. edn, (New York : Taylor & Francis, 2008).
- 9 Ladd, T. D. *et al.* Quantum computers. *Nature* **464**, 45, (2010).
- 10 Mishra, V. K. *An introduction to quantum communication*. (2016).
- 11 Fehr, S. Quantum Cryptography. *Found. Phys.* **40**, 494-531, (2010).
- 12 Economist. The Economist. Technology Quarterly: Here, there and everywhere. <<http://www.economist.com/news/essays/21717782-quantum-technology-beginning-come-its-own>> (2017).
- 13 Lo, H.-K., Curty, M. & Tamaki, K. Secure quantum key distribution. *Nature Photonics* **8**, 595-604, (2014).
- 14 Identity Theft resource center. Data breach reports: 2016 end of year report. <http://www.idtheftcenter.org/images/breach/2016/DataBreachReport_2016.pdf> (2017).
- 15 information is beautiful. World's Biggest Data Breaches. <<http://www.informationisbeautiful.net/visualizations/worlds-biggest-data-breaches-hacks/>> (2017).
- 16 O'Brien, J. L. Optical Quantum Computing. *Science* **318**, 1567-1570, (2007).
- 17 Santori, C., Fattal, D., Vuckovic, J., Solomon, G. S. & Yamamoto, Y. Indistinguishable photons from a single-photon device. *Nature* **419**, 594-597, (2002).
- 18 McIntosh, A. & Itzler, M. Single-Photon Detection, Generation, and Applications. *Optical Engineering* **53**, 081901-081901, (2014).
- 19 Chunnilall, C. J., Degiovanni, I. P., Kück, S., Müller, I. & Sinclair, A. G. Metrology of single-photon sources and detectors: a review. *Optical Engineering* **53**, 081910-081910, (2014).

- 20 Rozema, L. A. *et al.* Scalable Spatial Superresolution Using Entangled Photons. *Physical Review Letters* **112**, 223602, (2014).
- 21 Israel, Y., Tenne, R., Oron, D. & Silberberg, Y. Quantum correlation enhanced super-resolution localization microscopy enabled by a fibre bundle camera. **8**, 14786, (2017).
- 22 Brassard, G., Lütkenhaus, N., Mor, T. & Sanders, B. C. Limitations on practical quantum cryptography. *Physical Review Letters* **85**, 1330-1333, (2000).
- 23 Aharonovich, I., Englund, D. & Toth, M. Solid-state single-photon emitters. *Nat Photon* **10**, 631-641, (2016).
- 24 Ferlino, F. Molecular physics: Complexity trapped by simplicity. *Nature* **512**, 261-262, (2014).
- 25 Unitt, D. C. *et al.* Quantum dots as single-photon sources for quantum information processing. *Journal of Optics B: Quantum and Semiclassical Optics* **7**, S129, (2005).
- 26 Unitt, D. *Enhanced single photon emission from a quantum dot in a semiconductor microcavity*, Cambridge, (2005).
- 27 Kazimierczuk, T. *et al.* Single-photon emission from the natural quantum dots in the InAs/GaAs wetting layer. *Physical Review B* **84**, (2011).
- 28 Sonia, B., Kelley, R. & Jelena, V. Engineered quantum dot single-photon sources. *Rep. Prog. Phys.* **75**, 126503, (2012).
- 29 Bennett, A. J., Unitt, D. C., Atkinson, P., Ritchie, D. A. & Shields, A. J. High-efficiency single-photon sources based on InAs/GaAs quantum dots in pillar microcavities. *Physica E: Low-dimensional Systems and Nanostructures* **26**, 391-394, (2005).
- 30 Koperski, M. *et al.* Single photon emitters in exfoliated WSe₂ structures. *Nat Nano* **10**, 503-506, (2015).

Chapter 2

Background and Theory

2.1 Semiconductor background

This section addresses some of the key concepts in solid state physics that are important to understand when considering the light emission of a semiconductor.

2.1.1 Introduction to semiconductor bands

A semiconductor is a type of material that exists somewhere between an insulator and a metal (Figure 2.1), due to its small energy bandgap. This bandgap is a region of disallowed states, where no carriers can exist and consequently the density of states in the region is zero. To conduct electricity an electron needs to become unbound from its parent atom and move through the lattice, (i.e. move into the conduction band). In a metal, this is relatively easy as the valence and conduction bands overlap, so electrons in the top of the valence band are free to move. In an insulator, the conduction and valence bands are separated by a very large bandgap and electrons need a lot of energy to jump the gap leading to a negligible population of the conduction band even at high temperatures (e.g. room temperature) preventing any type of conduction. Semiconductors are somewhere in between these extremes, they have a small bandgap (typically around 1 eV)¹, which means that electrons require only a small amount of energy to jump into the conduction band.

The dashed line in Figure 2.1 illustrates the Fermi level; this represents the energy which has a 50% chance of being occupied when the system is in thermodynamic equilibrium. The semiconductor in Figure 2.1 has its Fermi level in the centre of the bandgap which illustrates that it is intrinsic. The Fermi level can be moved via the use of doping (intentionally adding an impurity into the crystal) so that it moves closer to either the valence or conduction band. This arises from the dopant material having a different number of electrons to the surrounding material. When interacting with the bulk crystal it either donates an electron moving the Fermi level closer to the conduction band, or accepts an electron moving the Fermi level towards the valence band. This repositioning of the Fermi level can greatly affect the electrical properties of the sample, a Fermi level close to the conduction band will allow electrons to easily populate the conduction band and is known as an n-type semiconductor, whereas a Fermi level close to the valence band makes it more likely the upper

states of the valence band will be empty and is known as a p-type semiconductor. Two of these different types of semiconductors placed next to each other is what is known a pn junction, and is widely used in electronics to electrically excite structures by getting electrons to flow from the n-type to the p-type.

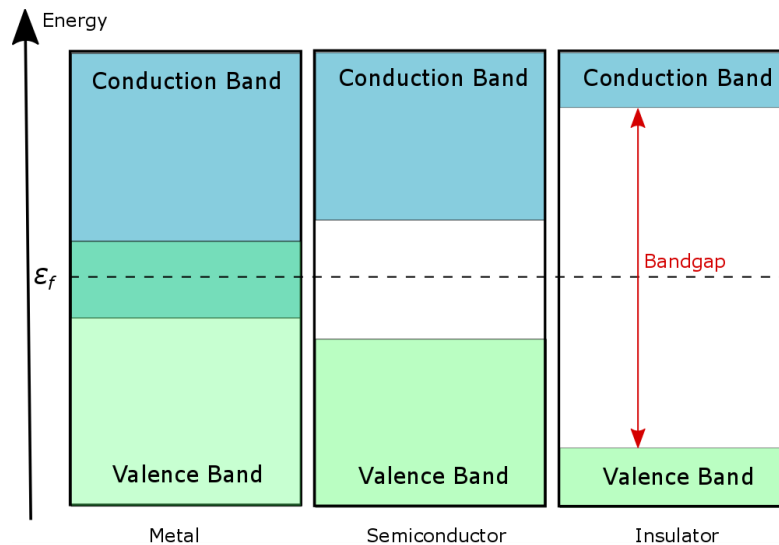


Figure 2.1: A simplified diagram showing how the valence and conduction bands vary with respect to metals, semiconductors and insulators.

2.1.2 Fermi-Dirac distribution

Electrons can be excited across the bandgap in a semiconductor at zero kelvin by gaining energy, which can be done either via electromagnetic radiation or via electrons being electrically injected into the conduction band. However, as the temperature increases there is a higher probability that electrons can be thermally excited across the bandgap and thus can populate the conduction band. This probability can be described using the Fermi-Dirac function $F(\epsilon)$, which describes the probability that an individual electron will exist in an energy state at a given temperature (T), and is given in the following equation (2.1), where ϵ is the electron's Energy, ϵ_f is the Fermi energy and k is Boltzmann's constant:

$$F(\epsilon) = \frac{1}{e^{(\epsilon - \epsilon_f)/kT} + 1} \quad (2.1)$$

This function is shown by the dashed green line in Figure 2.2, where at low temperature it exists up to the Fermi level only, meaning that the probability of an electron existing below the Fermi level is 1 and above zero. At higher temperatures, the Fermi function shifts and a small amount of it exists in the conduction band, meaning that a small fraction of the electrons in the crystal can bridge the energy gap (this proportionally reduces the amount in the valence band as there are only a finite number of electrons). The implications of this is that an intrinsic semiconductor at zero kelvin acts

as an insulator as it contains no free electrons. However at temperatures just under the materials melting point the same semiconductor will act like metal with a high number of electrons existing in the conduction band. This effect is especially important when optically characterising a semiconductor that emits light, as measurements often must be performed at low temperature to ensure that only the area excited can have carriers in the conduction band. This helps to resolve the emission from the conduction bands lowest energy states, due to them not being filled by thermally excited electrons.

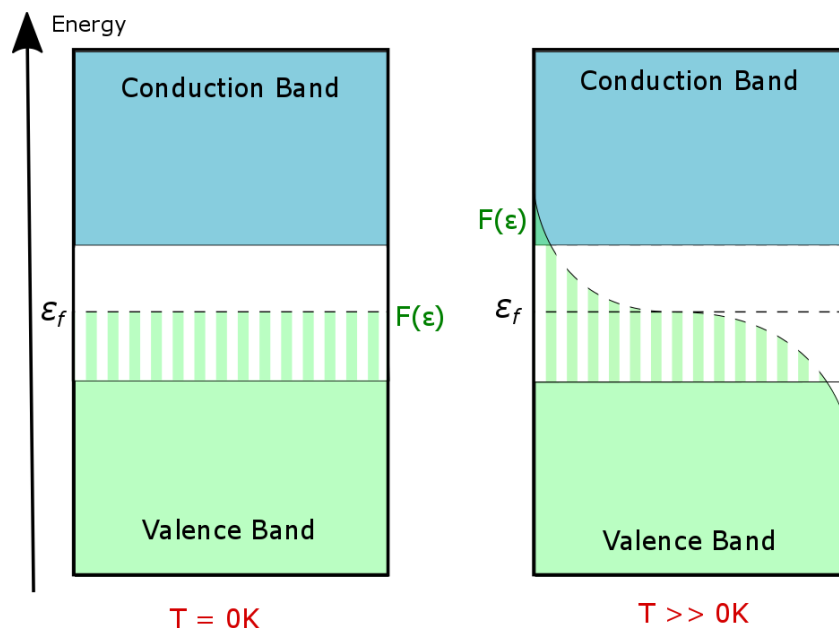


Figure 2.2: Band diagram illustrating the Fermi function ($F(\epsilon)$) at both low temperature and a high temperature.

The Fermi function gives the probability of an electron existing in a state, however the actual population $N(\epsilon)$ also depends on the density of states $\rho(\epsilon)$, and can be calculated by the following product:

$$N(\epsilon)d\epsilon = \rho(\epsilon)f(\epsilon)d\epsilon \quad (2.2)$$

This means that despite having a probability of being in the bandgap no carriers will exist there due to the density of states in the bandgap being zero at those energies (shown in Figure 2.2 as hashed green).

2.1.3 Direct and indirect semiconductors

The band diagrams given up to now have been highly simplistic, however in reality they are a lot more complex. A crystal lattice is a regularly repeating structure with translational symmetry, meaning its properties will be invariant across the entire lattice. This can be modelled by

considering the reciprocal lattice, which describes the relative angle and distance of each point of the real lattice in terms of a wavevector. The volume inside the reciprocal lattice is known as the Brillouin zone and is the elementary building block of the reciprocal lattice, all waves that pass through the crystal can be described by how they interact within this zone¹. The Brillouin zone contains multiple bands, however for the case of optical emission discussed in this thesis, only the shape and position of the conduction and valence band around the energy gap is important.

If a semiconductor has a valence band (VB) maximum and conduction band (CB) minimum in the same position in k -space it is said to have a direct bandgap. This means that an electron excited with a photon of energy $\hbar\omega \geq E_g$ will be promoted into the conduction band as shown in Figure 2.3a. If the valence and conduction band are offset from one another in k -space like in Figure 2.3b, then the semiconductor is said to have an indirect bandgap. A photon in the visible wavelength range has a wavevector an order of magnitude lower than the typical momentum of an electron near the valence band edge²; therefore the photon cannot promote an electron into the conduction band, as it does not have the momentum required (Δk). For an electron to undergo a successful indirect transition it requires momentum from an additional source, which in a lattice is most easily provided by a phonon. This is a quasiparticle that propagates through lattice vibrations, and provides the primary mechanism of heat propagation in a lattice. Phonons of high wavevector are common in a lattice even at low temperatures due to phonons having relatively small energies compared to the bandgap (0.01-0.03 eV)¹. Even so the probability that a photon collides with a suitable phonon, or produces a phonon with the correct wavevector to undergo an indirect transition is a lot lower than a direct excitation. This has a large impact on the absorption of light, with indirect semiconductors having a large dependence on temperature, due to their transitions being heavily dependent on the availability of phonons of the suitable wavevector.

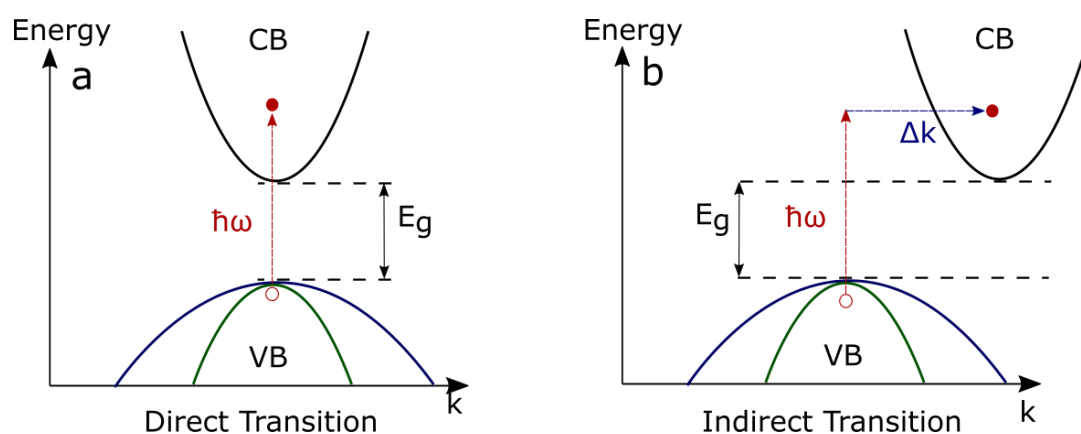


Figure 2.3: (a) A direct bandgap semiconductor (e.g. GaAs) undergoing a direct transition via absorption of a photon ($\hbar\omega$). (b) An indirect bandgap semiconductor (e.g. Si) undergoing an indirect transition enabled by the interaction with a phonon (Δk).

The light emission of a semiconductor is also heavily influenced by the band structure. The probability that an electron will recombine in an indirect bandgap semiconductor is lower than that of a direct bandgap, due to the difference in momentum between the electron and the hole (holes are explained further in section 2.2.1). This increases the lifetime of the excited state, making the light emission of an indirect bandgap material a lot weaker than a direct one. This accounts for one of the main reasons why direct bandgap semiconductors such as GaAs are generally more preferential to use as light emitters over indirect semiconductors such as silicon.

2.2 Artificial Atoms

Since atoms contain electrons confined in orbital shells they are very particular in the light they emit when excited. Electrons can only exist in a few allowed states meaning that when they relax to ground state they only release photons of distinct frequencies, a good example of this is the hydrogen spectral series. An individual atom is an excellent source for single photons, however it is not a very convenient emitter, as isolating individual ones require large, expensive atom traps³. It would be ideal if a light source like an atom could be made, which could be easily integrated into modern technology like a silicon based chip. This section thus describes how atom like emitters, (aka artificial atoms) can be formed in a semiconductor by manipulating its band structure to create confinement akin that seen in an atom.

2.2.1 Excitons

When electrons are excited out of the valence band they leave behind a hole in the valence band's sea of electrons. Electrons in a lattice balance the positive charge of the nuclei due to their negative charge, however the absence of an electron (aka a hole), leaves a net positive charge in the holes location due to the electron no longer screening the nuclei. Holes can therefore act like a positively charged particle and can move through the lattice and respond to electric fields in a similar way to a positron. When electrons and holes are produced they feel a mutual coulomb interaction due to their opposite charges, this binds them together creating a 2-body quasiparticle called an exciton.

In the formation of excitons, the mutual coulomb attraction places the electron and hole into a lower energy state than if they were free. This binding energy effectively lowers the energy needed to excite excitons relative to free electrons and holes, causing new levels to form in the energy gap just below the conduction band, which are offset from the conduction band edge by the binding energy (BE_{Exciton}) as shown in Figure 2.4.

Excitons can move through the crystal like a particle and thus can act as a method of energy transportation. This is very important for the optical properties of the semiconductor as excitons

formed at one location can migrate through the lattice and recombine elsewhere. A structure embedded underneath the surface of a semiconductor can still be excited by shining light on the surface, which creates excitons that migrate to the structure before they recombine. Quite often this type of excitation is performed using light with a higher energy than the bandgap of the embedded structure, so the exciton can “fall” into it via a non-radiative process.

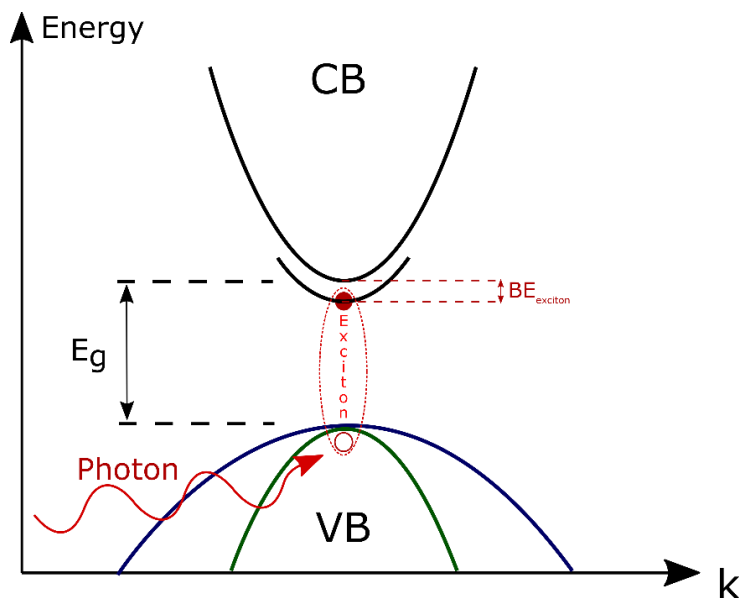


Figure 2.4: Band diagram showing the formation of an exciton with a binding energy ($BE_{exciton}$).

Excitons are charged neutral complexes meaning that although they are charge neutral and only transport energy, they can still weakly interact with other objects that possess charge which can include other excitons. This can lead to the formation of more complex excitons such as charged excitons known as trions which are excitons bound with either an additional electron/hole (eeh or ehh), and biexcitons, which are two neutral electron-hole pairs bound together (eehh).

Electron-hole pairs excited in a semiconductor are known as Wannier-Mott excitons. They are weakly bound together with radii larger than the lattice spacing, due to a large amount of electric screening and the electrons tending to have a small effective mass (for more information on effective mass please refer to Kittel [1]). The exciton can be described in a similar way to a hydrogen atom with an electron orbiting a positively charged region (hole), thus the binding energy can be given by the following modified Rydberg equation (2.3):

$$BE_{exciton} = \frac{\mu e^4}{2\hbar^2 \epsilon^2 n^2} \quad (2.3)$$

Where e = charge of an electron, ϵ = dielectric constant, n = principle quantum number, and μ = reduced mass, which can be calculated from the electron and hole effective masses i.e:

$$\frac{1}{\mu} = \frac{1}{m_e^*} + \frac{1}{m_h^*} \quad (2.4)$$

The implications of this equation are the formation of hydrogen-like states inside the bandgap which start to look more atom like, the state with the lowest energy (ground state) will occur when $n = 1$.

2.2.2 Excitonic Confinement

To create atom-like light emission it is essential to modify the density of states (DOS) so that the exciton can only exist at well-defined energies. This can be achieved in a semiconductor by creating an energy well for the exciton, which has a width approaching the electron-hole de-Broglie wavelength. As the width decreases and approaches the excitons Bohr radius, the exciton become increasingly confined and the electronic density of states splits from a continuum into discrete states. As well as the reduction in available energy states the bandgap is also effected, increasing as the size of the well decreases; this is an effect that is well described in quantum mechanics by a particle in a box⁴. Confinement can be applied in multiple dimensions to shrink the number of states available down, this is shown in Figure 2.5 where each reduction in dimension also reduces the density of states ($D(E)$). The most important of these is the quantum dot which confines the exciton in 3 dimensions and forces the DOS into a set of discrete delta functions. This is very similar in structure to the DOS of an atom, and there is a large degree of tunability with the exciton energy being dependent on the size of the quantum dot.

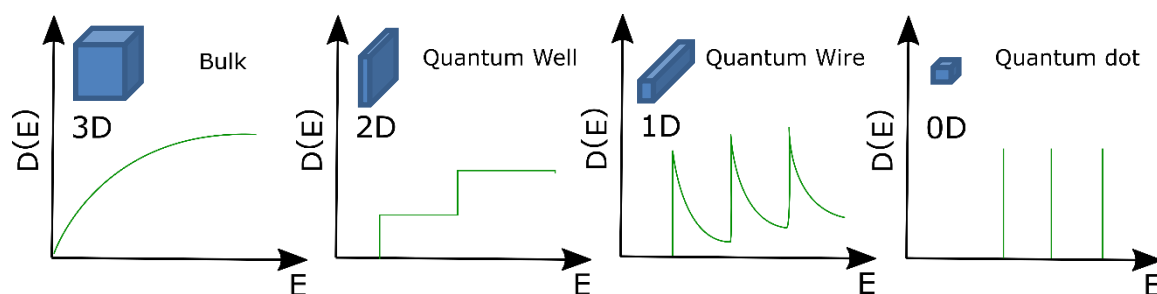


Figure 2.5: Diagrams showing the density of states of a semiconductor when confined in various dimensions, the number to the right of the y-axis denotes the degrees of freedom that an electron can travel in, with a bulk semiconductor quantum well, quantum wire and a quantum dot.

Confinement of excitons also helps to improve the emission of light at room temperature. In a bulk semiconductor at room temperature the phonon energy is sufficient to overcome the exciton binding energy, and pulls the electron and hole apart destroying the exciton. When confined however, the exciton has a smaller wave function, giving it an increased binding energy making it more difficult for phonons to destroy the particle. An additional effect of confining excitons is an increased generation of biexcitons/trions, due to the confining potential forcing excitons to interact with each other. Whereas this thesis mainly studies the confinement effects of quantum dots, it

should be noted that both quantum wells and wires can also be used in optoelectronic applications. Quantum wires can be especially useful due to them allowing a large density of states near the band edge.

2.2.3 Quantum dots

A semiconductor quantum dot (QD) is a type of heterostructure i.e. layers of two or more different semiconductors, grown in a common crystal. The quantum dot itself is a small island of a semiconductor (of the order of 10's of nm for GaAs), with a smaller bandgap than the semiconductor surrounding it. They can be formed in multiple different ways such as quantum well etching⁵, site controlled epitaxial growth^{6,7}, and self-assembled growth via the SK method⁸⁻¹². Two examples of QD band structures are shown in Figure 2.6, and are based on real semiconductor systems explored in chapters 4 and 5. In type-I QDs the electron and hole wave functions are spatially aligned and the exciton (dashed purple line) can recombine using a direct transition. In type-II quantum dots the electron and hole are not spatially aligned meaning that the electron hole overlap is reduced compared to type-I QDs; this decreases the probability of exciton recombination making type-II QDs less bright. TEM images of both InAs/GaAs and GaSb/GaAs QDs can be seen in Figures 4.2 and 5.2.

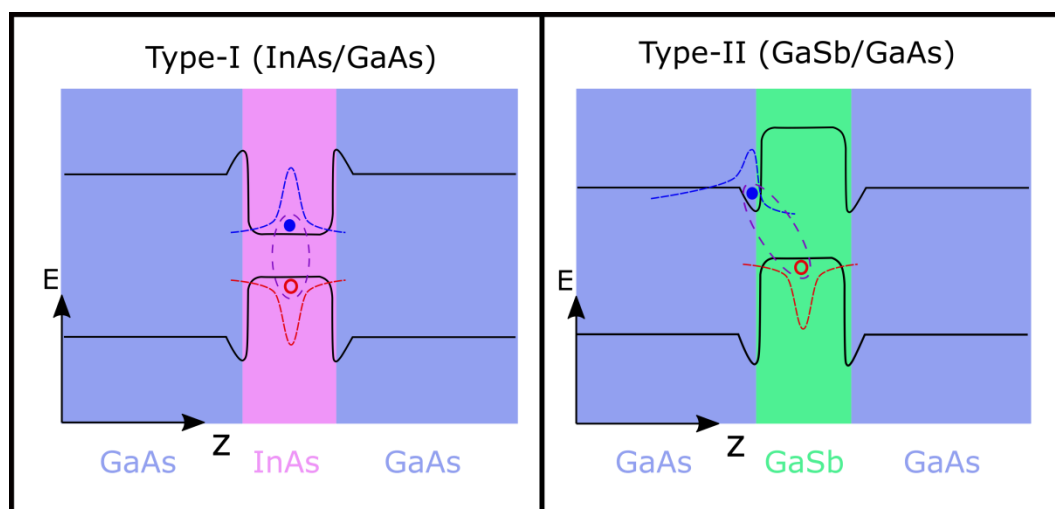


Figure 2.6: Simple band diagrams showing the two different types of quantum dots explored in this thesis, the electrons and their wave functions are shown in blue and the holes in red.

The field of quantum dots is very broad and only a brief description is presented here, for a more detailed review of the subject the author recommends reading Bimberg, et al. [13] also Bimberg and Pohl [14].

2.2.4 Properties of Type-II QDs

In this thesis type-II QD structures are predominantly studied, and are well known to exhibit a strong blueshift in their emission energy with increased excitation power^{15,16}. The cause of this blueshift is not fully understood with coulomb charging¹⁷ state filling¹⁸ and band bending¹⁹ all being cited in the literature; each of these effects are summarised below:

Band Bending: Band bending refers to the distortion of the band into a triangular shape at the interface between a nanostructure, and its surrounding material. This distortion arises due to the charge separation of carriers creating an electric field, which causes a small potential well to form at the nanostructures interface. The shift in the ground state of this well (ΔE) is dependent on the carrier density (n) in the proximity of the nanostructures, can be calculated using the following equation (2.5):¹⁵

$$\Delta E = \left(\frac{\hbar}{2m}\right)^{1/3} \left(\frac{9}{8}\pi\right)^{2/3} \left(\frac{2\pi e^2}{\epsilon_0 \epsilon_r}\right)^{2/3} n^{2/3} \quad (2.5)$$

m = effective electron mass, ϵ_0 = permittivity of free space, ϵ_r = relative permittivity and e = charge of an electron. This equation means that changing the excitation and producing more carriers will alter the energy of the well, thus causing a shift in the emitted wavelength.

State Filling: Due to the electrons and holes being spatially separated in a type-II system their lifetime in the QD before they recombine is relatively long compared to a type-I system. If the injection of carriers is faster than the recombination rate then electrons/holes will not be able to occupy the ground state in a confined structure due to the ground state already being filled with other carriers. When this occurs if the injected carriers have initially a significantly higher energy than the bandgap they will occupy higher energy states. If they radiatively recombine whilst in this state, they will produce a photon with higher energy than the bandgap.

Coulomb charging: Electronic states of a semiconductor are very sensitive to charge due to coulomb interactions between electrons. When the number carriers increase, the coulomb interactions between the electrons increase as described by the Hartree approximation. This has a large effect on the charge of a type-II structure due to their carriers being spatially separated.

In type-II structures only one carrier is tightly confined the other is either delocalized, or localized only by the mutual coulomb interaction between them. Taking GaSb/GaAs QRs studied in chapter 4 as an example, the hole is tightly bound and forms a spatially indirect exciton state with the unbound electron. In a many body regime (lots of carriers) the hole-hole (E_{hh}) interactions will dominate the electron-hole (E_{eh}) and the electron-electron (E_{ee}) interactions, due to the spatial separation of electrons and holes reducing (E_{Eh}) and the electrons delocalisation reducing (E_{ee}). Based on equation 2.6 this leads to an energetic shift (ΔE_{ex}) when there is a change in the hole-hole

interaction¹⁷. This is different from type-I like structures where all the contributions to ΔE_c will be roughly equal, due to the electrons and holes having a strong wave function overlap, and very similar confinement.

$$\Delta E_{ex} = E_{ee} + E_{eh} + E_{hh} \quad (2.6)$$

Hodgson, et al. [15] showed that the shift in energy can be considered a capacitive effect with each hole contributing to an increase in charge and thus an increase in energy i.e. $\Delta E_{hh} \propto n_h$. They additionally state that (assuming the semiconductor stayed charge neutral) you can use the bimolecular recombination approximation to find a relationship between the intensity of the emission (I) and the corresponding carrier concentration. This leads to the following relationships: band bending $\propto I^{1/3}$ and coulomb charging $\propto I^{1/2}$. It is therefore expected that under high excitation powers coulomb charging should dominate.

2.2.5 Quantum Yield

An important term to understand when talking about the light emission of a material is the quantum yield (QY) of the system. This is simply the ratio of the number of photons emitted by the material compared to the number of photons it absorbed. This value is very important when considering the efficiency of a system and its worth as a light source, especially when considering single photon sources. A material with a high QY is less likely to de-excite non-radiatively, which makes it more likely a system will emit a photon when excited. This is very important for emitters like single photon sources, which for their applications such as QKD are required to be deterministic²⁰.

2.3 Light emitting 2D materials

2D materials are generally made from crystals that are very strongly bonded in the same plane, but are only weakly bonded by van der Waal interactions to the layers above and below them. A good example of this is graphene which has sp^2 hybridisation, which keeps all covalent bonds in the same plane. These different planes can stack together using van der Waals forces to form the common material known as graphite. The reduction of a bulk crystal down to a single atomic layer of the crystal, causes confinement of carriers similar to a quantum well (see section 2.2.2), giving remarkably different optical and electronic properties from their bulk counterparts²¹. Monolayer Transition Metal Dichalcogenides (TMD) are a set of especially interesting 2D materials that have recently seen an explosion of interest from researchers, due to them having a direct bandgap in the visible to near infra-red spectrum²²⁻²⁴.

2.3.1 Properties of TMD's

TMD's have the formula MX_2 where M = transition metal, and X = Chalcogen (Group VI in the periodic table). The bandgap of these materials change as they are reduced to just a few layers, materials like MoS_2 can change from an indirect to a direct bandgap with the removal of just one layer. This is demonstrated in Figure 2.7, where from (a-c) very little change in the band structure is observed; however upon changing to a monolayer (Figure 2.7d) there is a significant change in the band edge which changes the lowest energy transition from indirect (dashed line) to direct (solid line). Additionally, TMD's exhibit a range of interesting optical physics due to their strong exciton binding energy and large spin-orbit interaction that can heavily influence their optical spectra²⁵⁻²⁸.

TMDs are additionally exciting because they can be integrated into silicon which can enable a wide range of innovative technologies. This can be achieved by directly exfoliating using adhesive tape^{29,30}, chemically exfoliating with TMD flakes in solution²⁴ or by directly growing onto the substrate using Chemical Vapour Deposition (CVD)^{31,32}. TMDs can also easily be stacked on-top of each other to create multi-layered heterostructures^{33,34}, enabling novel structures such as ultrathin LEDs³⁴. Defects inside monolayer sheets have been shown as capable of emitting single photons at low temperature³⁵, these defect layers can be integrated into a heterostructure and electrically excited³⁶ opening up the potential of using these materials as a single photon source operating on silicon, a highly desirable property for applications such as quantum information processing.

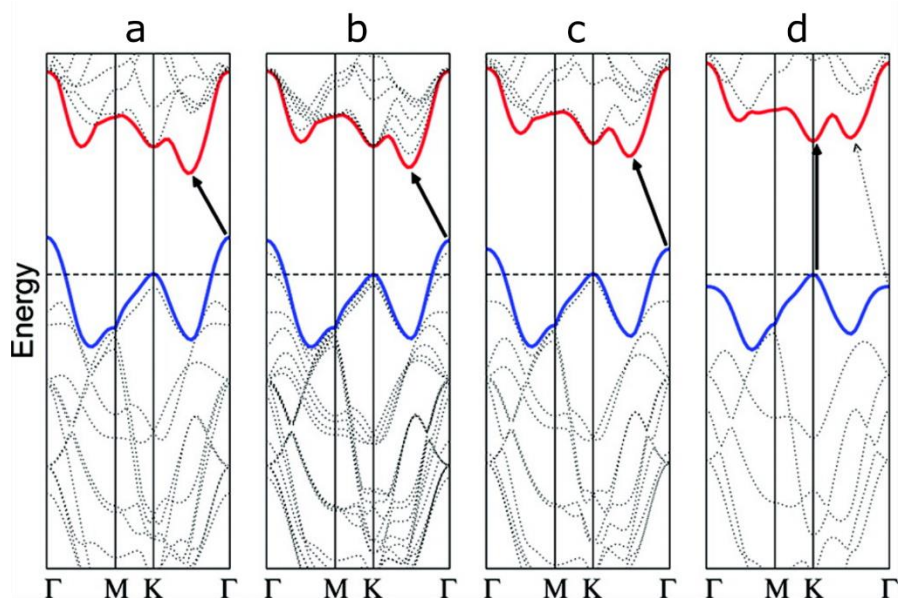


Figure 2.7: – Band structure of MoS_2 , which a solid arrow showing the lowest energy transition whilst in: (a) Bulk, (b) 4 layers, (c) Bilayer and (d) Monolayer. Reprinted with permission from Splendiani, et al. [37]. Copyright 2017 American Chemical Society.

Enhancing light

Light emitted from nanostructures is often insufficient for certain practical applications. A good single photon source for example requires an efficient flow of photons that have a high repetition rate, good efficiency as well as having a low multi-photon probability and being indistinguishable from each other. Quantum dots solve the issue of indistinguishability and prevent multi-photon events as only one exciton can exist in a QD state at a time. However, the frequency of the radiative emission and the probability that each pulse contains a photon are also essential especially in applications such as quantum cryptography, where a high transmission rate is required. There are however several strategies that can be used to improve light emission these are:

- Increasing the internal quantum efficiency of the device, and therefore increasing the probability of an exciton undergoing radiative recombination, i.e. increasing the quantum yield.
- Modifying the spontaneous emission rate so they can emit more photons per second (e.g. Purcell enhancement).
- Increase the solid angle of light collected from the nanostructure into your optics (i.e. extraction efficiency), which helps to reduce the photons lost to the external environment.

This section thus describes three different methods that use some of the strategies above to increase the light observed from a semiconductor nanostructure.

2.3.2 The Solid Immersion Lens

A Solid Immersion Lens (SIL) is a lens that can be placed on the surface of a semiconductor to effectively embed the light source within a higher refractive index medium than air; to increase the optical extraction efficiency. SIL's are typically formed from high index glass³⁸, and are placed directly on the surface to either enhance the resolution of the optical image, or increase the light being coupled out.

Two different geometries of SIL have been predominantly studied; those with a hemispherical shape (h-SILs) and those with a Weierstraß shape (s-SILs)³⁸ (shown in Figure 2.8). S-SILs have a higher magnification than h-SILs, scaling as the refractive index of the SIL squared ($\propto n^2$) as opposed to a direct linear relationship for a h-SIL ($\propto n$). S-SILs also have the advantage of further increasing the light input/output coupling efficiency by being able to refract a higher number of rays at the SIL-air boundary, thus collecting/delivering more light to and from a device. The main disadvantage of an s-SIL is its strong chromatic aberration, as the increased height leads to more variation in the path length taken by different rays. This can be very problematic for good quality imaging of a device, but acceptable for low bandwidth emitters such as quantum light LED's, for which getting the best extraction of light is essential.

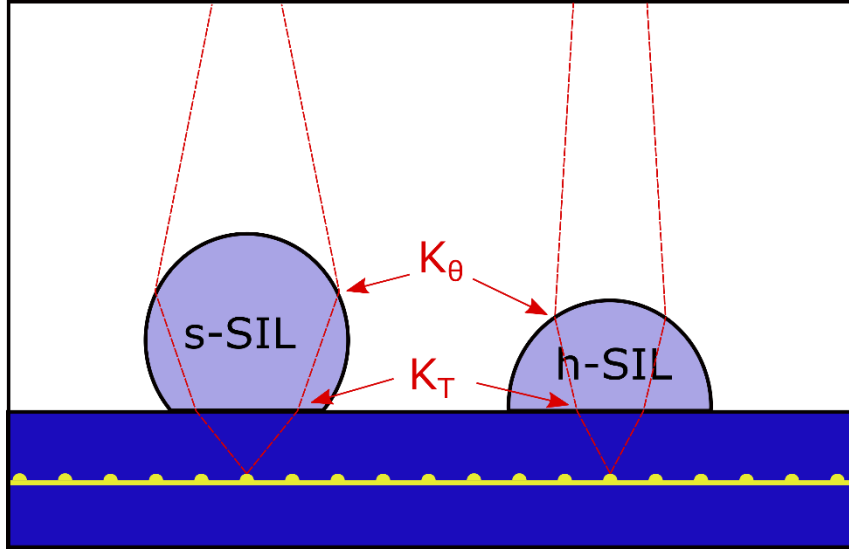


Figure 2.8: Diagram showing the difference in shape between a s-SIL and a h-SIL. The red dashed lines highlight how a larger angle of emitted light is collected in the s-SIL relative to the h-SIL.

Due to an s-SIL being wavelength dependent, the geometry often needs to be tuned so that the best coupling efficiency is reached. For an embedded emitter like a quantum dot this can be achieved by using the following equation (2.7)³⁹ where h = vertical height, r = radius, $n(\lambda)$ = refractive index and X = distance from the base of the SIL to the emitter.

$$h = r \left(1 + \frac{1}{n(\lambda)} - X \right) \quad (2.7)$$

The increase in collection efficiency of a SIL comes from reduction in reflection losses at the substrate-SIL boundary (K_T), combined with a refraction at the SIL-air boundary (K_θ), as shown in Figure 2.8. The efficiency of an s-SIL positioned above an embedded emitter can be calculated using equation (2.8), where η = collection efficiency, NA_{obj} = numerical aperture of objective, n_{SIL} = refractive index of SIL, n_s = refractive index of substrate³⁹.

$$\eta = \frac{1}{2} \left[1 - \sqrt{1 - \left(\frac{NA_{obj} n_{SIL}}{n_s} \right)^2} \right] \quad (2.8)$$

Using (2.8) and placing the values for the SIL used in chapter 4, we can calculate that the efficiency should increase from 0.8% to 2.7%.

For the case of putting a SIL on a surface emitter such as a 2D material (as demonstrated in chapter 6) the above equation (2.8) is no longer valid; as the TMDC thickness is much less than the wavelength of emission resulting in a negligible refractive index. The solid angle increase instead comes solely from the refraction that occurs at the SIL-air interface (K_θ), for this reason h-SILs will not increase the light output for a surface emitter placed in the centre as there will be no refraction.

A SIL with a height between that of an s-SIL and an h-SIL will have an enhancement at this interface. To calculate the enhancement due to K_θ , the angle of refraction at the SIL-air interface (γ) needs to be calculated as a function of the release angle of the light from the monolayer (θ). This is shown below in equation 2.9, where a is the minimum distance between the base of the SIL and its spherical centre ($h-r$), n_1 is the refractive index of the SIL and n_2 is the refractive index of the environment (unity for air),

$$\gamma = \sin^{-1} \left[\frac{a}{r} \sin(\theta) \right] - \sin^{-1} \left[\frac{n_1 a}{n_2 r} \sin(\theta) \right] + \theta \quad (2.9)$$

This equation can be used to find the maximum angle of emission that can be coupled into the collection optics. A ray trace simulation is shown in Figure 2.9, highlighting the increase in the number of rays that can be launched into the collection optics with a SIL present on the surface.

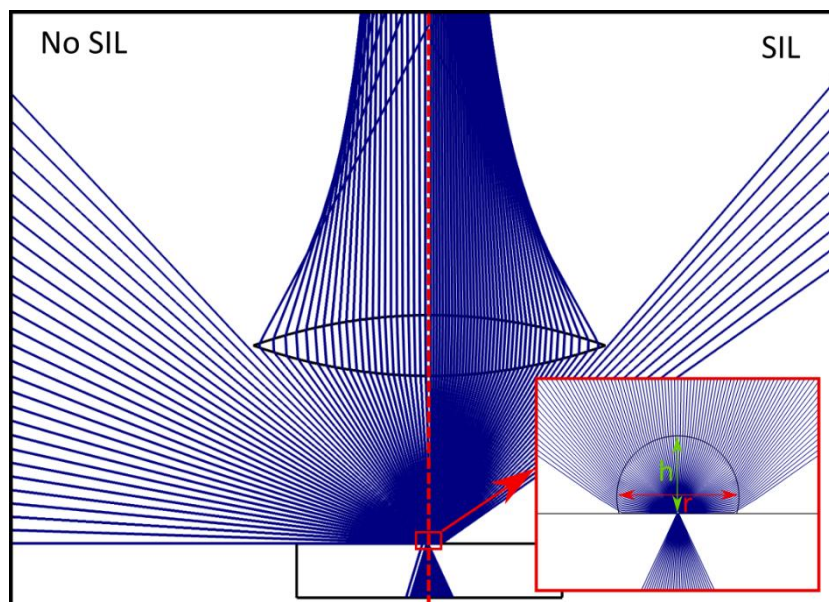


Figure 2.9: A simulation illustrating how rays from a surface emitter couple to a lens, with and without a solid immersion lens (SIL). The SIL increases the coupling efficiency of rays emerging from the emitter. The inset shows a magnified region surrounding the SIL.

Glass SILs can be difficult to integrate into complex structures, due to their morphology often creating potential air gaps between the bottom of the SIL and the emitter, which reduces the optical enhancement. Glass SILs can also be challenging to permanently mount, physical mounts can be bulky and potentially reduce the SILs collection area⁴⁰, whilst gluing methods such as the one used in the chapter 4 often create poor interfaces, due to the epoxy having a different refractive index. Furthermore, the process of mounting a glass SIL can risk damage to sensitive structures such as site controlled quantum dots^{6,7}, and plasmonic structures⁴¹, due to the hardness of the glass.

SILs however can be formed out of other materials, Born, et al. [42], demonstrated that a SIL could be formed out of UV curable epoxy. In this paper, they use a thin needle to finely position then dispense a droplet onto their substrate, this can then be cured into a solid object without causing any damage to the surface. To create SILs of the correct geometry the dispensing environment is incredibly important. The needle must be immersed in a dense liquid phase medium to modify the interfacial surface tensions sufficiently to allow a droplet with a contact angle of 90 degrees or above to be produced⁴³; this can later be fine-tuned using electrowetting to achieve the desired geometry. The flexibility of this method in varying the contact angle makes them ideal for use in semiconductor systems where short tuneable focal lengths are required, such as optical wireless imaging receivers⁴⁴. This idea is expanded on in chapter 6 where epoxy based SILs are mounted onto 2D materials.

2.3.3 Purcell Effect

One method of enhancing the light of an emitter is by modifying its rate of spontaneous emission otherwise known as the Purcell effect⁴⁵. The rate of spontaneous emission for a light source in a weak coupling regime (γ) is given by Fermi's golden rule, which states that it's proportional to the final density of states ($\rho(\omega)$) as shown in Equation (2.10)⁴⁶.

$$\gamma = \frac{2\pi}{\hbar^2} |\langle d.E \rangle|^2 \rho(\omega) \quad (2.10)$$

Where $|\langle d.E \rangle|^2$ represents the probability, there will be a transition and is a product of the dipole moment operator d and the electric field operator E . What this equation means is that by modifying the density of states around the dipole emitter ($\rho(\omega)$), and positioning/aligning the dipole emitter at a local electric field maximum the spontaneous emission rate can be increased. The maximum achievable enhancement is defined as the Purcell factor (F_p) and is given in Equation (2.11), where the first bracket is a constant, the second gives the wavelength of light in the material, and the third bracket is the ratio between the quality factor (Q) and the mode volume (V) of the cavity.

$$F_p = \left(\frac{3}{4\pi^2}\right) \left(\frac{\lambda_0}{n}\right)^3 \left(\frac{Q}{V}\right) \quad (2.11)$$

Semiconductor based Fabry-Pérot microcavities are a common example of the Purcell effect in action. In these structures an emitter is placed in the centre of a cavity with distributed Bragg reflectors (DBR's) both above and below it. Both the cavity and the mirrors lengths are tuned to the wavelength of emission by λ/n and $\lambda/4n$ respectively, this allows a resonance to form with an electric field maximum at the emitters location increasing the quality factor Q . This can further be improved by reducing the mode volume (V) by the formation of micropillars that confine the mode, in lateral dimensions⁴⁷⁻⁵⁰.

2.3.4 Plasmonic enhancement

Surface plasmons are oscillations of electrons that can exist at the interface between two materials which can couple to light to form surface plasmon polaritons (SPP). For this to happen certain conditions of the material interface must be met⁵¹:

- 1) The real part of the relative permittivity (or dielectric constant) of the material forming the surface (e.g. gold) must be of opposite sign to the space it is in (i.e. negative if it's in air) for the wavelength of light incident on it.
- 2) The magnitude of the permittivity in the surface (e.g. gold) must be greater than that of the space it's in, to ensure the polaritons are bound to its surface.
- 3) For surface plasmons, the propagation constant (commonly denoted as β) must be greater than the wavevector of incident light (k). Therefore, in order to excite SPP's, the wavevector k needs modifying, this can be achieved using a prism or a grating.

This effect has many physical applications, the one relevant to this work is the enhancement of photoluminescence of surface emitters. There are two effects that cause this enhancement, the first is an increase in light absorption. This occurs when a pump laser's light is resonant with a surface plasmon, causing an increase in the coupling of EM radiation to the local electric field⁵². If the emitter is close enough, the energy of the electric field can couple to the emitter through the near field effectively providing it with an increase in excitation, and thus a larger generation of electron-hole pairs⁵³. The second effect arises from the large electric fields causing a modification of the spontaneous emission rate via the Purcell effect. This increase in exciton recombination can lead to dramatic increases in the PL intensity, with enhancements from 2 – 28000 times the original intensity being reported⁵²⁻⁵⁴.

2.4 References

- 1 Kittel, C. *Introduction to solid state physics*. 5th ed. edn, (New York : Wiley, 1976).
- 2 Jaros, M. *Physics and applications of semiconductor microstructures*. (Oxford England : Clarendon Press, 1989).
- 3 Pérez-Ríos, J. & Sanz, A. S. How does a magnetic trap work? *American Journal of Physics* **81**, 836-843, (2013).
- 4 Rae, A. I. M. *Quantum mechanics*. 5th ed. edn, (New York : Taylor & Francis, 2008).
- 5 Reed, M. A. *et al.* Spatial quantization in GaAs–AlGaAs multiple quantum dots. *Journal of Vacuum Science & Technology B: Microelectronics Processing and Phenomena* **4**, 358-360, (1986).
- 6 Watanabe, S. *et al.* Dense uniform arrays of site-controlled quantum dots grown in inverted pyramids. *Applied Physics Letters* **84**, 2907-2909, (2004).
- 7 Dimastrodonato, V., Mereni, L. O., Young, R. J. & Pelucchi, E. Growth and structural characterization of pyramidal site-controlled quantum dots with high uniformity and spectral purity. *physica status solidi (b)* **247**, 1862-1866, (2010).
- 8 Dekel, E. *et al.* Multi-Exciton Spectroscopy of a Single Self Assembled Quantum Dot - Physical Review Letters.pdf>. *Physical Review Letters* **80**, 4991, (1998).
- 9 Trevisi, G. *et al.* The effect of high-In content capping layers on low-density bimodal-sized InAs quantum dots. *J. Appl. Phys.* **113**, 194306, (2013).
- 10 Tadić, M., Peeters, F. M., Janssens, K. L., Korkusiński, M. & Hawrylak, P. Strain and band edges in single and coupled cylindrical InAs/GaAs and InP/InGaP self-assembled quantum dots. *J. Appl. Phys.* **92**, 5819-5829, (2002).
- 11 Songmuang, R., Kiravittaya, S., Sawadsaringkarn, M., Panyakeow, S. & Schmidt, O. G. Photoluminescence investigation of low-temperature capped self-assembled InAs/GaAs quantum dots. *J. Cryst. Growth* **251**, 166-171, (2003).
- 12 Bayer, M. *et al.* Fine structure of neutral and charged excitons in self-assembled In(Ga)As/(Al)GaAs quantum dots. *Physical Review B* **65**, (2002).
- 13 Bimberg, D., Grundmann, M. & Ledentsov, N. N. *Quantum dot heterostructures*. (John Wiley, 1999).
- 14 Bimberg, D. & Pohl, U. W. Quantum dots: promises and accomplishments. *Materials Today* **14**, 388-397, (2011).
- 15 Hodgson, P. D. *et al.* Blueshifts of the emission energy in type-II quantum dot and quantum ring nanostructures. *J. Appl. Phys.* **114**, 073519, (2013).
- 16 Klenovský, P., Steindl, P. & Geffroy, D. Excitonic structure and pumping power dependent emission blue-shift of type-II quantum dots. *Scientific Reports* **7**, 45568, (2017).
- 17 Müller-Kirsch, L. *et al.* Many-particle effects in type II quantum dots. *Applied Physics Letters* **78**, 1418-1420, (2001).

- 18 Gradkowski, K. *et al.* Coulomb-induced emission dynamics and self-consistent calculations of type-II Sb-containing quantum dot systems. *Physical Review B* **85**, 035432, (2012).
- 19 Sun, C. K. *et al.* Optical investigations of the dynamic behavior of GaSb/GaAs quantum dots. *Applied Physics Letters* **68**, 1543-1545, (1996).
- 20 Ding, X. *et al.* On-Demand Single Photons with High Extraction Efficiency and Near-Unity Indistinguishability from a Resonantly Driven Quantum Dot in a Micropillar. *Phys. Rev. Lett.* **116**, 020401, (2016).
- 21 Xia, F., Wang, H., Xiao, D., Dubey, M. & Ramasubramaniam, A. Two-dimensional material nanophotonics. *Nat Photon* **8**, 899-907, (2014).
- 22 Mak, K. F. & Shan, J. Photonics and optoelectronics of 2D semiconductor transition metal dichalcogenides. *Nature Photonics* **10**, 216-226, (2016).
- 23 Wang, Q. H., Kalantar-Zadeh, K., Kis, A., Coleman, J. N. & Strano, M. S. Electronics and optoelectronics of two-dimensional transition metal dichalcogenides. *Nat Nanotechnol* **7**, 699-712, (2012).
- 24 Chhowalla, M. *et al.* The chemistry of two-dimensional layered transition metal dichalcogenide nanosheets. *Nat Chem* **5**, 263-275, (2013).
- 25 Huang, J., Hoang, T. B. & Mikkelsen, M. H. Probing the origin of excitonic states in monolayer WSe₂. *Scientific Reports* **6**, 22414, (2016).
- 26 Yan, T., Qiao, X., Liu, X., Tan, P. & Zhang, X. Photoluminescence properties and exciton dynamics in monolayer WSe₂. *Applied Physics Letters* **105**, 101901, (2014).
- 27 Xu, X., Yao, W., Xiao, D. & Heinz, T. F. Spin and pseudospins in layered transition metal dichalcogenides. *Nature Physics* **10**, 343-350, (2014).
- 28 Neumann, A. *et al.* Opto-valleytronic imaging of atomically thin semiconductors. *Nat Nanotechnol* **12**, 329-334, (2017).
- 29 Novoselov, K. S. *et al.* Two-dimensional atomic crystals. *Proceedings of the National Academy of Sciences of the United States of America* **102**, 10451-10453, (2005).
- 30 Novoselov, K. S. *et al.* Electric Field Effect in Atomically Thin Carbon Films. *Science* **306**, 666-669, (2004).
- 31 Gutiérrez, H. R. *et al.* Extraordinary Room-Temperature Photoluminescence in Triangular WS₂ Monolayers. *Nano Letters* **13**, 3447-3454, (2013).
- 32 Cain, J. D., Shi, F., Wu, J. & Dravid, V. P. Growth Mechanism of Transition Metal Dichalcogenide Monolayers: The Role of Self-Seeding Fullerene Nuclei. *ACS Nano* **10**, 5440-5445, (2016).
- 33 Kaplan, D. *et al.* Excitation intensity dependence of photoluminescence from monolayers of MoS₂ and WS₂/MoS₂ heterostructures. *2D Materials* **3**, (2016).
- 34 Withers, F. *et al.* Light-emitting diodes by band-structure engineering in van derWaals heterostructures. *Nature Mater* **14**, 301 - 306, (2015).
- 35 Koperski, M. *et al.* Single photon emitters in exfoliated WSe₂ structures. *Nat Nano* **10**, 503-506, (2015).

- 36 Palacios-Berraquero, C. *et al.* Atomically thin quantum light-emitting diodes. *Nat. Commun.* **7**, 12978, (2016).
- 37 Splendiani, A. *et al.* Emerging Photoluminescence in Monolayer MoS₂. *Nano Letters* **10**, 1271-1275, (2010).
- 38 Qian, W., Ghislain, L. P. & Elings, V. B. Imaging with solid immersion lenses, spatial resolution, and applications. *Proceedings of the IEEE* **88**, 1491-1498, (2000).
- 39 Serrels, K. A. *et al.* Solid immersion lens applications for nanophotonic devices. *NANOP* **2**, 021854-021829, (2008).
- 40 Sung, H.-Y. *et al.* Fabrication of mounting device to apply solid immersion lens to infra-red microscopy. *International Journal of Precision Engineering and Manufacturing* **15**, 375-379, (2014).
- 41 Henzie, J., Lee, J., Lee, M. H., Hasan, W. & Odom, T. Nanofabrication of Plasmonic Structures. *Annual Review of Physical Chemistry* **60**, 147-165, (2009).
- 42 Born, B., Landry, E. L. & Holzman, J. F. Electrodispensing of Microspheroids for Lateral Refractive and Reflective Photonic Elements. *IEEE Photonics Journal* **2**, 873-883, (2010).
- 43 Lee, C. C., Hsiao, S. Y. & Fang, W. in *TRANSDUCERS 2009 - International Solid-State Sensors, Actuators and Microsystems Conference*. 2086-2089.
- 44 Jin, X., Guerrero, D., Klukas, R. & Holzman, J. F. Microlenses with tuned focal characteristics for optical wireless imaging. *Applied Physics Letters* **105**, 031102, (2014).
- 45 Purcell, E. M. Spontaneous emission probabilities at radio frequencies. *Phys. Rev.* **69**, 681, (1946).
- 46 Unitt, D. *Enhanced single photon emission from a quantum dot in a semiconductor microcavity*, Cambridge, (2005).
- 47 Unitt, D. C. *et al.* Quantum dots as single-photon sources for quantum information processing. *Journal of Optics B: Quantum and Semiclassical Optics* **7**, S129, (2005).
- 48 Bennett, A. J. *et al.* Microcavity single-photon-emitting diode. *Applied Physics Letters* **86**, 181102, (2005).
- 49 Bennett, A. J., Unitt, D. C., Atkinson, P., Ritchie, D. A. & Shields, A. J. High-efficiency single-photon sources based on InAs/GaAs quantum dots in pillar microcavities. *Physica E: Low-dimensional Systems and Nanostructures* **26**, 391-394, (2005).
- 50 Bennett, A. J., Unitt, D. C., Shields, A. J., Atkinson, P. & Ritchie, D. A. Influence of exciton dynamics on the interference of two photons from a microcavity single-photon source *Opt Express* **13**, 7772, (2005).
- 51 MAIER, S. A. *Plasmonics: Fundamentals and Applications*. (Springer, 2007).
- 52 Wang, Z. *et al.* Giant photoluminescence enhancement in tungsten-diselenide-gold plasmonic hybrid structures. *Nat Commun* **7**, (2016).
- 53 Lumdee, C., Yun, B. & Kik, P. G. Gap-Plasmon Enhanced Gold Nanoparticle Photoluminescence. *ACS Photonics* **1**, 1224-1230, (2014).

- 54 Sobhani, A. *et al.* Enhancing the photocurrent and photoluminescence of single crystal monolayer MoS₂ with resonant plasmonic nanoshells. *Applied Physics Letters* **104**, 031112, (2014).

Chapter 3

Experimental Methods and Techniques

3.1 Optical Spectroscopy

The core work performed in this thesis is the optical characterisation of semiconducting light emitters, which can emit at room temperature. This section will go into further detail on how these optical characterisations were performed.

3.1.1 Photoluminescence

Photoluminescence (PL) is used throughout this thesis to gain information on the optical emission of both III-V nanostructures and 2D materials. PL can be performed in two different regimes macro and micro-photoluminescence. In macro-PL, either no lens or a 5x/10x lens is used to image the entire sample. This typically gives low power densities, but a wide laser spot, allowing large ensembles of Quantum dots (QDs) to be observed. Micro-PL is similar, except it uses a microscope objective in a confocal setup to reduce the excitation laser spot down to approximately $1 \mu\text{m}^2$. This is approaching the absolute diffraction limit for far field optics, and allows individual/small groups of QDs to be observed, and their variation imaged across the entire sample.

The setup used to perform micro-PL is shown in Figure 3.1; a frequency doubled 532 nm Nd:YAG CW laser is used to illuminate a sample mounted in a dry optical cryostat. The laser light passes initially through two neutral density filter wheels to control its intensity, which is then recorded by sampling 10% of the light using a calibrated laser power meter. BS1 is used to reflect the laser light into the cryostat, a reflected to transmitted ratio of 8:92 is used a trade-off to increase the light transmission from the cryostat to the spectrometer, at the expense of reducing the maximum excitation power. The remaining laser light is focussed to a narrow spot by a 50x Olympus LCPLN-IR objective lens with an NA of 0.65, giving an absolute Abbe diffraction limit for the laser diameter of $0.41 \mu\text{m}$. This objective was mounted on a piezo stage which can be programmed to move up to $20 \mu\text{m}$ in x-y-z, and has a step size of 25 nm. Photoluminescence maps performed with this piezo stage have suggested that the laser spot diameter in our system is in reality closer to $1 \mu\text{m}$. This increased diameter possibly arises due to the laser being focussed through the cryostat window, which is most likely acting as a source of scattering.

The PL from the sample was analysed by passing it through an Andor Shamrock 500 spectrometer, onto either a InGaAs or an EMCCD detector, depending on the wavelength of emission. The PL is filtered before entering the spectrometer to remove reflected laser light with a long-pass filter. It enters the spectrometer by being focussed through a variable width entrance slit to maximise resolution and minimise background signals.

Additionally, the system contains an LED with a beam splitter (BS2) to couple white light into the system along with the laser light, this can be directed into a camera using another beam splitter (BS3) to allow visual inspection of the samples surface. After alignment of the optical components is completed the white light can be switched off and BS3 removed from the system to ensure maximum PL transmission to the spectrometer is achieved.

Samples are mounted behind an optical window under vacuum in an ICE oxford dry optical cryostat. The cryostat employs a Sumitomo GM cryocooler, which is suspended above the cold head and coupled using a He⁴ transfer gas held in a bellows to significantly reduce vibration. Using this arrangement temperatures approaching 15K, along with RMS vibrations ~50 nm can be achieved.

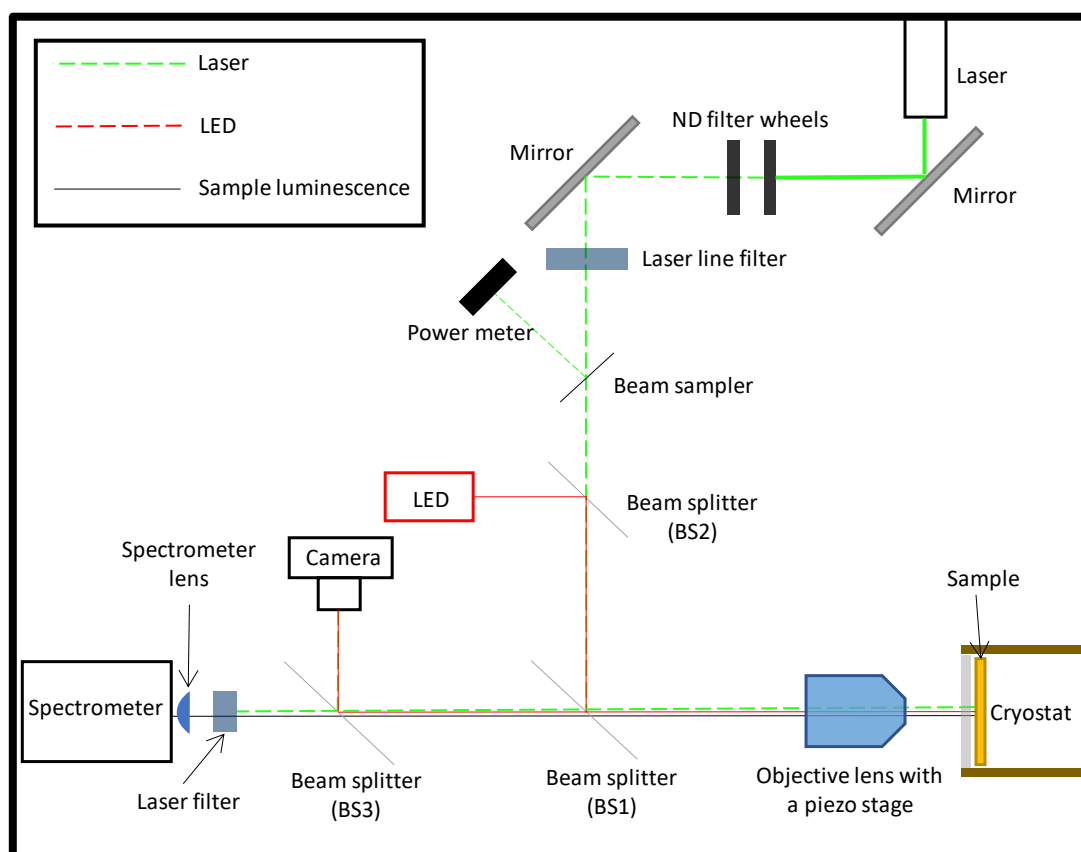


Figure 3.1: Diagram showing the low temperature photoluminescence system, the objective lens (50x NIR lens with an NA of 0.65) is used to both excite the sample and collect the light emitted.

3.1.2 Raman Spectroscopy

Raman spectroscopy data is presented in Chapter 7, to analyse the structure of a 2D material. In Raman spectroscopy, a laser is used to excite vibrational energy levels in a molecule via inelastic scattering of a photon. This scattered photon has a slight energy shift equal to the excited energy level of the molecule, which can be used to identify that molecular structure. Raman data in Chapter 7 was taken using a commercial Raman system built by Horiba. A, 100x objective lens was used to both excite and collect the light from the sample.

3.2 Fabrication

In this section, the fabrication techniques used to create the samples that were optically analysed in Chapters 4-7 are discussed. The growth of the QD samples in Chapter 4, and 5 was performed by collaborators using molecular beam epitaxy (MBE), with the novel step of this work being the optical characterisation, and the techniques employed to isolate individual exciton emissions. The growth of the individual samples is summarised in the respective Chapters and for more information on MBE growth please see P. Frigeri, et al. [1].

3.2.1 Exfoliation of 2D materials

The 2D materials used in Chapter 6, were exfoliated onto a SiO₂/Si substrate using mechanical exfoliation. To perform this, a bulk crystal of either MoS₂ or WSe₂, was placed onto a low adhesive (nitto) tape to remove and produce a single layer using the scotch tape method². The Si substrate had a SiO₂ capping layer with a thickness of 300 nm creating an interference colour which gives high contrast with respect to a TMD monolayer when under white light illumination^{3,4}. The sample was then placed into an oxygen plasma before exfoliation to remove any organic contaminants and heat the sample's surface. This method was found to be very effective at producing mono/bilayers with lateral dimensions up to 50 μm.

3.2.2 Fabricating epoxy SILs

The basic process involved in fabricating epoxy SILs onto a 2D material is illustrated in Figure 3.3. A SiO₂/Si substrate with a monolayer exfoliated onto it was immersed into a glycerol bath, which provides the liquid phase medium needed to allow high contact angled droplets to form on the sample (b). This arises due to a modification of the surface tension experienced by the droplet, and can be explained by considering the Young equation, which is given in Equation (3.1) and is illustrated in Figure 3.2.⁵

$$\cos(\theta_y) = \frac{\gamma_{sf} - \gamma_{sl}}{\gamma_{lf}} \quad (3.1)$$

When the filler solution is air, the solid-filler surface tension (γ_{sf}) is a lot greater than both the solid-liquid (γ_{sl}), and the liquid-filler surface tensions. This makes $\cos(\theta_y)$ equal to a large positive number, resulting in a small equilibrium contact angle (θ_y). However, when a filler solution such as glycerol is used (γ_{sf}) reduces dramatically, making $\cos(\theta_y)$ a large negative number; this enables droplets with a large contact angle to form. Glycerol is an ideal filler solution due to it being relatively inert with respect to the epoxy. Other filler solutions such as water are less ideal as they are known to be absorbed by the epoxy, leading to a significant reduction in the SIL's transparency⁶.

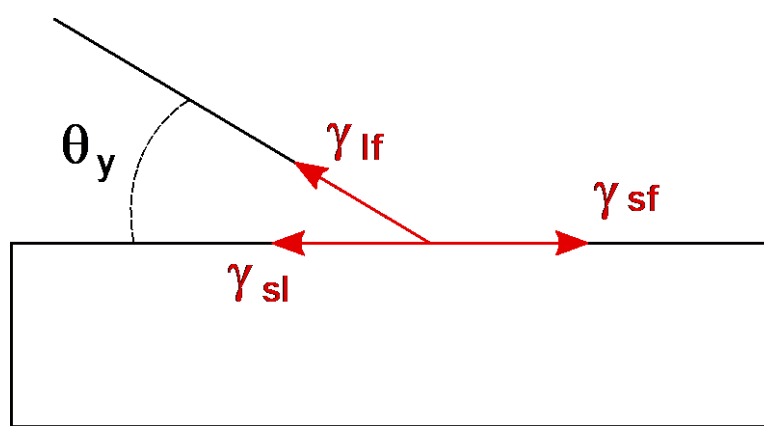


Figure 3.2: Diagram illustrating Young's equilibrium contact angle (θ_y), due to the balancing of the solid-liquid (γ_{sl}), liquid-filler (γ_{lf}) and solid-filler (γ_{sf}) surface tensions.

The UV-curable epoxy was then formed onto the wafer using an air dispensing system and a 32-gauge needle (c); this allowed the droplet size to be carefully controlled. The droplet itself can be dispensed using two-different methods, both of which have their own advantages:

- Needle raise method: A tiny amount of epoxy is dispensed at the tip of the needle and is pushed into the sample so it wets. Epoxy is then slowly dispensed to increase the size of the droplet whilst the needle is carefully raised. This method is useful for getting the centre of the SIL in the exact location, however the act of raising the needle whilst dispensing can lead to a reduction in the droplets sphericity, effecting the focus of the SIL.
- Drop method: A droplet of the desired size is dispensed using the needle above the surface. The droplet is then gently lowered until it meets the surface, very gentle compression of the droplet is used to encourage wetting. This method generally leads to good sphericity as the droplet can spread in a motionless environment. However, this uncontrolled spreading makes it difficult to ensure the centre of the SIL is positioned directly over small nanostructures.

The shape of the SIL is highly dependent on the wettability of the surface, the more hydrophilic the surface, the tighter the contact angle of the initially dispensed droplet. Contact angle can be reduced either by electrowetting or by simply allowing the epoxy to wet then sucking back the epoxy to shrink the overall size, as once wetted the epoxy does not tend to lift away from the substrate. However, increasing the contact angle after wetting is very challenging; therefore, the initial angle that the epoxy makes to the substrate normally dictates the maximum possible angle of SIL that can be formed. A good example is bare SiO₂ which has a relatively low surface tension and this can only create angles close to 90 degrees. This is not however an issue for 2D materials or small-scale structures as they themselves modify the surface tension changing the surface wettability and increasing the contact angle. Surface roughness enhancing contact angle is known as the lotus effect, or superhydrophobicity^{7,8} and can be exploited to ensure that a SIL has a contact angle large enough that it can be later reduced to the desired value.

Finally, after the needle is retracted, the droplet can be hardened into a SIL by exposure to UV light (d). The sample can be removed from the glycerol bath and rinsed with deionised water, to remove the residual glycerol.

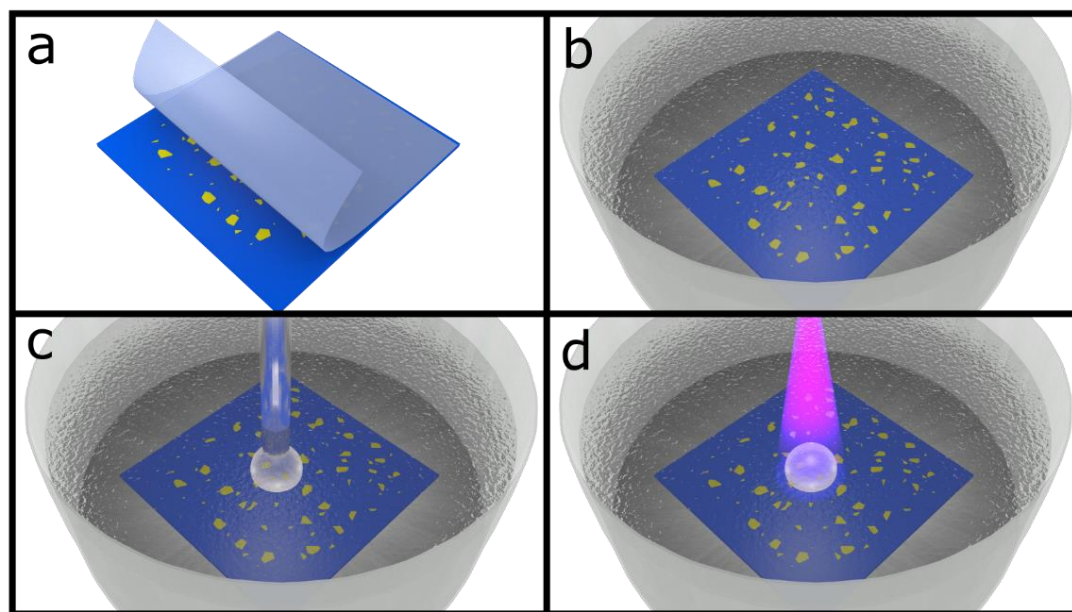


Figure 3.3: The experimental process used to mount SILs deterministically on to monolayers of 2D materials; (a) monolayers were produced via mechanical exfoliation and then transferred onto SiO₂; (b) sample was immersed in a bath of glycerol; (c) UV curable epoxy was dispensed over the monolayer and shaped; (d) the epoxy was bonded onto the surface with a UV light source.

3.2.3 Electron Beam Lithography

Electron beam lithography (EBL) is a technique used to pattern a surface of a semiconductor, using a beam of electrons. This pattern is written onto an electron-sensitive photoresist which is spin-coated onto the surface of the sample. When the electron beam is incident onto the photoresist the long molecular chains that form the resist are broken. These shorter chains are dissolvable in an appropriate developer, causing the exposed areas to be removed, leaving behind the desired pattern. This process typically has a very high resolution, with precision on the order of nm being possible due to the short wavelength of high energy electrons.

In this thesis EBL was used in both Chapter 5 and 7, to create micropillars and plasmonic structures. A JEOL-JBX-5500ZD was used to perform this patterning, with a minimum beam diameter of less than 1 nm. However, in practice backscattering of electrons makes this closer to 10 nm as the CSAR 62 resist used is highly sensitive.

3.2.4 Plasma Etching

Dry etching or plasma etching, when combined with a photoresist, is a common technique used to selectively remove semiconductor material from a sample. Material is removed from unmasked areas, whereas masked areas are unaffected due to the masking material having a very reduced etch rate compared to the semiconductor, the etch rate difference between these is known as the selectivity. There are two etch mechanisms in a plasma: chemical etching where etchant gasses in the plasma chemically react with the surface, and physical etching where large unreactive ions (e.g. Ar⁺) bombard the surface removing atoms via sputtering.

Chemical etching is most predominant in inductively coupled plasma (ICP) systems, which use a rotary magnetic field to deliver energy to the plasma, making the ions move in plane with the sample. This magnetic field allows the ions to chemically react across the sample in a highly uniform way. With the execution of a good etch chemistry, the by-products of these reactions form a vapour in the plasma and get extracted with the rest of the gasses. Chemical reactions also play a role in reactive ion etching (RIE), however in this system physical etching is more predominant with an oscillating electric field used to drive the plasma up and down to enable sputtering. These two etching methods can be combined together in an ICP-RIE machine, which combines a rotating magnetic field with an oscillating electric field. This allows the advantages of an ICP (high selectivity and smooth etched surfaces), and RIE (high anisotropic etching) to be combined, so that the plasma density and the momentum of the ions bombarding the surface can be precisely controlled. This can enable some very high aspect ratio structures to be formed, such as the plasmonic samples presented in Chapter 7.

3.2.5 Deposition

In this thesis, two different methods used to deposit materials: electron beam physical vapour deposition (EBPVD), and plasma enhanced chemical vapour deposition (PECVD).

EBPVD is a deposition technique performed at a very high vacuum, where the material to be deposited is subjected to an intense electron beam, causing it to heat up and sublimate into a vapour due to the low pressure. This vapour then precipitates back into a solid coating anything in the chamber with a thin film. This technique usually gives a very high film purity over other techniques such as thermal evaporation, due to the very low vacuum. The EBPVD machine used in this work was custom built, and achieved its high vacuum of 2×10^{-7} mbar using a cryopump. This machine was used to deposit both the Ti and Au films required for creating plasmonic structures in Chapter 7.

PECVD uses a plasma environment to chemically react two different gasses into a solid form. In this work Silane gas was reacted with oxygen to create SiO_2 which acted as a hard mask for etching gold. The PECVD is an ideal machine for this task due to it providing a fast deposition rate and a uniform film coverage.

3.3 Imaging techniques

A lot of the samples discussed in this thesis have small-scale structures on the order of microns or below that cannot be observed sufficiently with the unaided eye, and require more specialist equipment. Predominantly, most observations were made using a standard optical microscope in conjunction with post processing software to help improve the visual clarity e.g. Figure 6.5. However, some of the structures fabricated such as the micropillar in chapter 5, and the plasmonic structures in chapter 7 required a resolution beyond the diffraction limit of visible light to fully observe. This section thus contains some of the techniques used to image to sub-micron structures.

3.3.1 Scanning Electron Microscope (SEM)

A scanning electron microscope (SEM) is an essential tool for surface characterisation. They have magnifications more than three orders of magnitude higher than the best optical microscopes, combined with large depths of field⁹. This can enable some incredibly small structures to be imaged, for example the SEM used in this work (JEOL JSM-7800F) has resolution of 0.8 nm^{10} . This resolution is made possible due to the short wavelength of high energy electrons (0.08 nm at 15 keV). A scanning electron microscope works in a similar way to an optical microscope. Electrons are produced using an electron gun and focussed into a beam using a series of lenses. In the SEM these lenses are called electromagnetic lenses, due to them using magnetic fields to force a beam of electrons to travel in a tightening helical motion. This electron beam is directed onto the sample surface, where electrons are scattered and are directed into a detector. Unlike an optical microscope, however, the beam needs to be raster-scanned across the sample to image an area. This is facilitated

by the scanning coils, which deflect the electron beam into a series of lines that sweep over the desired imaging area. There are two types of signals released from this process, secondary and backscattered electrons. Secondary electrons are produced when the beam dislodges electrons from the surface, and provides topological information, whereas backscattered electrons are produced sub-surface and can be used to get chemical composition information via energy-dispersive x-ray spectroscopy¹¹. In this thesis, the backscattered electrons were used to gain topological information of fabricated gold nano-trenches and GaAs based micropillars; allowing their fabricated dimensions to be assessed.

It should be noted that a scanning transmission electron microscope (STEM) is used to image individual dots in chapters 4 and 5. This works in a similar way to an SEM, except instead of observing backscattered electrons, the electrons that are transmitted through the sample are detected. The resultant interference from the electrons interactions, with the atoms of the lattice can be detected and reconstructed to get information on the internal structure of the sample. The STEM measurements presented in this thesis were performed by collaborators, but are included to allow the reader to visualise the embedded quantum dot structures that are not normally observable. For more information on STEM, please see Clarke [12].

3.3.2 Scanning Probe Microscopy (SPM)

Scanning probe microscopy is a surface characterisation technique that uses a sharp pyramid shaped probe to gain topological, mechanical and electrical information of a samples surface. One of the most common and versatile imaging techniques that comes under this term is the atomic force microscope (AFM). The success of an AFM arises from its simplicity of design combined with its ability to measure non-conductive samples with high sensitivity (the tip is able to detect forces to nN precision)¹³. A simple diagram showing the operation of an AFM is shown in Figure 3.4. A sharp probe is attached to a cantilever and placed carefully into contact with the surface using piezoelectric actuators (piezo) mounted to the sample stage. The cantilever is then carefully raster-scanned across the sample using x-y piezos mounted underneath the sample stage. The cantilever tip is very sensitive to the topography of the surface, any slight increase in height will cause the tip to experience a repulsive force due to short range, repulsive coulomb interactions between the tip and the surface. This force causes the cantilever to deflect, and can be detected by reflecting a laser off the cantilever and into a photodetector. The change in position of the laser spot on the photodetector is measured and a feedback circuit then moves the z-piezo to keep the force on the cantilever constant. The movement of the z-piezo is recorded and used to provide the topography of the sample.

In this thesis AFM measurements in Chapter 7 were performed in tapping mode using a Bruker Icon AFM. Tapping mode oscillates the cantilever just below its resonant frequency; this reduces the

lateral friction and makes it less likely for the probe to get stuck on the surface. In this mode the amplitude of the oscillation is monitored and put into the feedback circuit, so that the Z-piezo can keep the tip force constant. Using this method 20 nm gold trenches could be measured, providing information on the quality of their fabrication.

Another type of SPM used by collaborators in this thesis was cross sectional scanning tunnelling microscopy (X-STM). This imaging method works by placing a bias between the sample and an atomically sharp probe, then bringing the sample close and measuring the tunnelling current that passes through. Tunnelling currents are very sensitive to the distance from the sample, which combined with the very sharp tip of an STM allows individual atoms to be resolved. Additionally, the tunnelling current is dependent on the band structure of the material, therefore enabling the chemical composition of each atom to be assessed. This is incredibly useful for understanding the growth of quantum dots, and is used in Figure 4.2 to observe the growth of a single GaSb/GaAs quantum ring. The STM data in Figure 4.2 was obtained from collaborators, and further details can be found by reading Smakman, et al. [14].

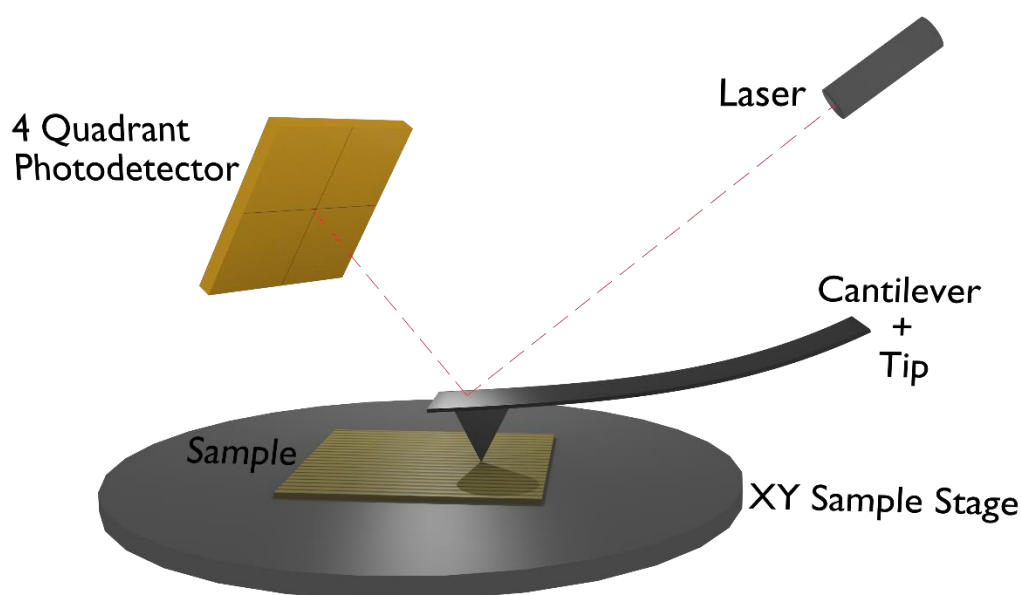


Figure 3.4 – Diagram showing the basic principle of an AFM. Deflections in the height of the cantilever due to the sample are detected by reflecting a laser from the end of the cantilever and recording deflections in the reflected light using a photodetector.

3.4 References

- 1 P. Frigeri, L. Seravalli, G. Trevisi & Franchi, S. in *Comprehensive semiconductor science and technology*, Vol. 3 Ch. 3.12, 480-522 (Elsevier, 2011).
- 2 Novoselov, K. S. *et al.* Electric Field Effect in Atomically Thin Carbon Films. *Science* **306**, 666-669, (2004).
- 3 Benameur, M. M. *et al.* Visibility of dichalcogenide nanolayers. *Nanotechnology* **22**, 125706, (2011).
- 4 Blake, P. *et al.* Making graphene visible. *Applied Physics Letters* **91**, 063124, (2007).
- 5 Frieder, M. & Jean-Christophe, B. Electrowetting: from basics to applications. *Journal of Physics: Condensed Matter* **17**, R705, (2005).
- 6 Born, B., Landry, E. L. & Holzman, J. F. Electrodispensing of Microspheroids for Lateral Refractive and Reflective Photonic Elements. *IEEE Photonics Journal* **2**, 873-883, (2010).
- 7 Yamamoto, M. *et al.* Theoretical Explanation of the Lotus Effect: Superhydrophobic Property Changes by Removal of Nanostructures from the Surface of a Lotus Leaf. *Langmuir* **31**, 7355-7363, (2015).
- 8 Lafuma, A. & Quere, D. Superhydrophobic states. *Nat Mater* **2**, 457-460, (2003).
- 9 Vernon-Parry, K. D. Scanning electron microscopy: an introduction. *III-Vs Review* **13**, 40-44, (2000).
- 10 JOEL. JSM-7800F Schottky Field Emission Scanning Electron Microscope. <<https://www.jeol.co.jp/en/products/detail/JSM-7800F.html>> (2017).
- 11 D'Alfonso, A. J., Freitag, B., Klenov, D. & Allen, L. J. Atomic-resolution chemical mapping using energy-dispersive x-ray spectroscopy. *Physical Review B* **81**, 100101, (2010).
- 12 Clarke, D. R. Review: transmission scanning electron microscopy. *Journal of Materials Science* **8**, 279-285, (1973).
- 13 Giessibl, F. J. Advances in atomic force microscopy. *Reviews of Modern Physics* **75**, 949-983, (2003).
- 14 Smakman, E. P. *et al.* GaSb/GaAs quantum dot formation and demolition studied with cross-sectional scanning tunneling microscopy. *Applied Physics Letters* **100**, 142116, (2012).

Chapter 4

Enhancing the photoluminescence of GaSb/GaAs QD nano-structures

This chapter describes how individual type-II like GaSb/GaAs quantum rings can be isolated to allow observations of individual rings with exciton linewidths of 200 μeV . The power dependent blueshift of individual peaks is studied and compared to the ensemble's blueshift, to gain a better understanding of the underlying physics of this system.

4.1 Introduction

Embedded semiconductor nanostructures such as quantum dots (QDs) and quantum Wells (QW's) have a variety of optical and electronic applications that can be used to perform both classical and quantum measurements¹. QD's are especially interesting for use in optical semiconductor devices, due to their reduced dimensionality enabling carrier confinement and single photon generation²⁻⁵, making them suitable for quantum optoelectronic applications^{6,7}. Additionally, QDs are capable of improving classical light sources such as lasers, giving them lower threshold currents and higher thermal stabilities⁸.

Quantum dots can be grown using a variety of methods, such as Metal Organic Chemical Vapour Deposition (MOCVD)⁹, Liquid Phase Epitaxy (LPE)¹⁰, Molecular Beam Epitaxy (MBE)¹¹, and can be formed either by a random process (SK-growth¹²) or in a site controlled approach¹³. One type of QDs that have been recently studied are self-assembled Quantum Rings (QRs), which can be formed from III-V semiconductor materials and then capped to create an embedded light source. These structures were first grown using an MBE by García, et al. [14], who partially capped InAs quantum dots with 5 nm GaAs, and noted a redistribution of the island material during the capping process. In 2004 Kobayashi, et al. [15], showed that GaSb/GaAs quantum ring structures could be formed by growing a 10 nm “cold layer” (490°C) of GaAs over self-assembled GaSb QDs then “hot capping” (580°C) with 100 nm of GaAs. The ring formation arises due to the initial GaAs cold cap dramatically increasing the strain felt by the Quantum dot as it becomes forced into the more tightly spaced GaAs lattice. This increase in strain is particularly high for GaSb compared to other dot forming materials such as InAs (34% larger¹⁶). This high strain creates a force that causes the Sb to migrate radially,

leaving behind GaAs in the centre and forming a ring structure. There are several different mechanisms which have been suggested to facilitate the migration of the Sb from the dot, these are: strain driven lateral diffusion, As/Sb exchange and Sb segregation^{16,17}; however it is likely that for GaSb QRs that the latter two mechanisms are the most important due to very little intermixing of the rings¹⁷, (this can be observed in Figure 4.2).

GaSb QRs are interesting due to them having spatially separated electrons and holes, due to their type-II band alignment. Holes become tightly confined in the Sb rich lobes of the ring, whereas the electrons are more loosely confined in the surrounding material via their coulomb interaction to the hole (shown in Figure 4.1). This spatial separation is a disadvantage for light emitting devices as they have a reduced exciton recombination rate compared to a type-I structure, which arises due to a smaller electron-hole wavefunction overlap^{18,19}. However, this in turn can have its own advantages, allowing for long carrier storage times making them useful for optical/electronic memories²⁰. Furthermore, the deep hole confinement potential in the GaSb ring²¹ has been shown to enable room temperature emission^{22,23}, which opens up their use as a room temperature light source both for multiple-photon applications (e.g. LEDs), and single photon applications (e.g. quantum information processing).

To understand if QRs are a viable single photon source there are several challenges that need to be overcome. The first is that QR samples are generally too dense in their emission to see individual rings using micro-photoluminescence (μ PL); their random formation causes high densities of rings and dots as well as clusters of Sb to form¹⁷ (see Figure 4.1), which can cause a lot of background signal. Therefore, to create a single photon source out of these structures there needs to be a method that can be used to observe the emission of a single ring, so it can be identified amongst all the other signals. This would allow measurements to be performed to test its suitability as a single photon source such as a Hanbury Brown-Twiss experiment²⁴.

Another challenge for these types of emitters is the relatively low optical efficiency that arises from the type-II band structure; which needs to be optimised if it is to be a viable light source. This chapter will try and address each of the above issues by using aperture masks and solid immersion lenses (SILs) to reduce and enhance the excitation/emission area, to enable the observation of individual rings. It also explores the physical origin of the power dependent blue-shift that QRs display when optically excited.

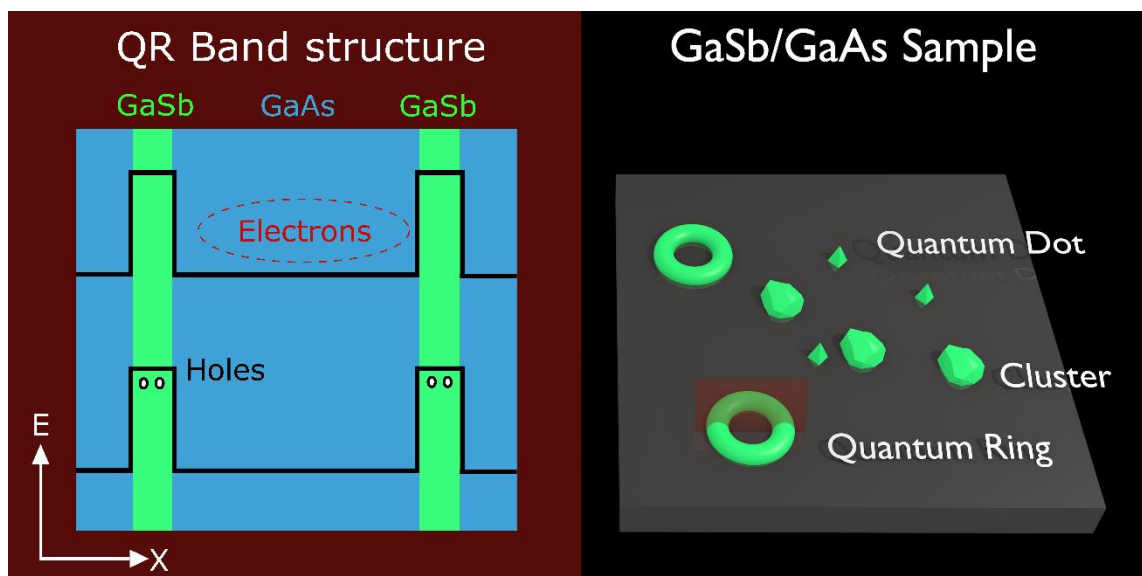


Figure 4.1: Image showing a 3D representation of the band structure of a quantum ring (left), and a representation of the structures present on the GaSb/GaAs sample.

4.2 Isolating individual Quantum rings

GaSb quantum rings studied in this chapter were grown in Lancaster using MBE; details of the growth including TEM and STM images of the structure and morphology of the GaSb structures can be found by reading Smakman, et al. [17]. These example cross sectional STM and TEM images are shown in Figure 4.2 a, b respectively, with Sb atoms represented by the bright yellow in (a), and dark grey/black in (b). Very distinct lobes of GaSb are present with a highly pure GaAs centre, the average diameter of these rings is approximately $15 \pm 5 \text{ nm}$ ¹⁷.

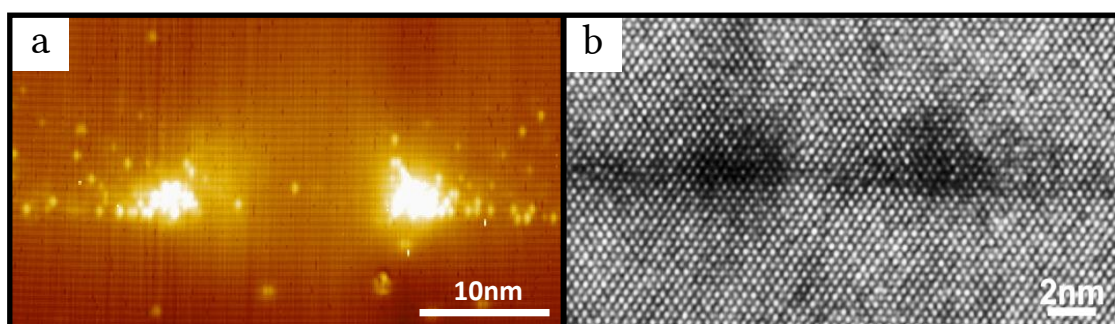


Figure 4.2: Cross sectional images of a Quantum Ring in a similar structure, using in (a) Scanning tunnelling microscope (STM) and (b) Transmission electron microscope (TEM), the bright pixels in (a) and the dark in (b) show Sb atoms.

The density of the Quantum ring structures for similarly grown samples was found to be approximately $1 \times 10^{10} \text{ cm}^{-2}$ ($100 \mu\text{m}^{-2}$)²⁵, which means that a laser spot created in the μPL setup (see

chapter 3) incident on the sample will excite over a thousand structures, which makes it very challenging to isolate individual peaks. Figure 4.3a shows the emission of the grown GaSb/GaAs samples over a range of different wavelengths, the GaAs, wetting layer and QD/QR peak are highlighted and the spectra matches that of previously reported GaSb/GaAs structures²¹. Figure 4.3b shows a typical QR peak for this sample, excited using a 1 μm diameter laser spot at an excitation power of 10 μW . The spectra is very rich containing a lot peaks which all overlap due to the density of the QR structures, making the observation of individual excitons from a single QR very challenging. Another issue arises from the relatively low optical efficiency of the QRs. Their type-II band structure causes the intensity of light emitted from the sample to be relatively weak, this can be seen by comparing the intensity of the QR peak to the GaAs and wetting layer peak in Figure 4.3a. The high powers required to observe the QD/QR peak can also cause inhomogeneous broadening of the peaks via the generation of a large number of carriers, which cause charge fluctuations that produce local electric fields causing a stark shift²⁶. It was therefore clear from these results that the ‘normal’ operating resolution in the μPL setup was not sufficient to observe individual rings, therefore to isolate a smaller number of rings, additional modifications to the experimental setup were required.

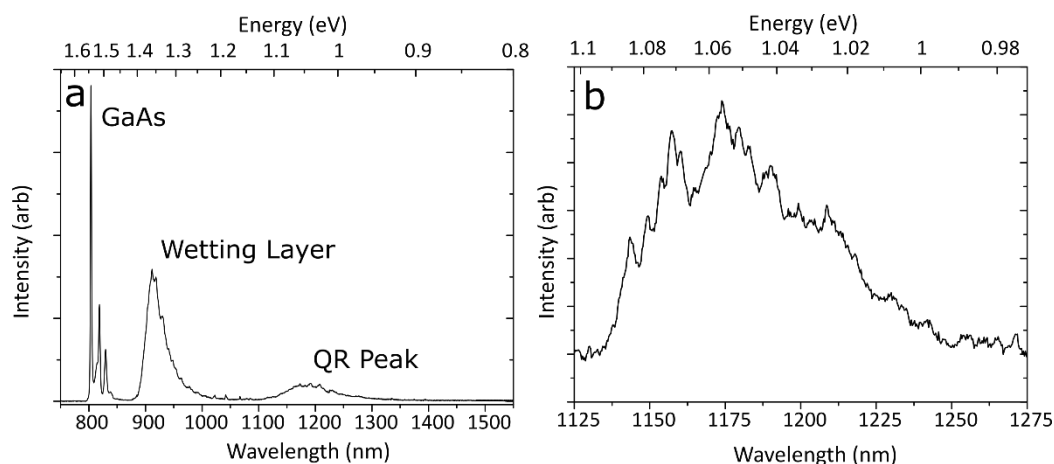


Figure 4.3: Photoluminescence showing in (a) 800 – 1550nm sweep of the PL emitted by these QR samples, (b) PL spectra of the QR peak.

4.2.1 Modifying the sample surface

To isolate individual rings two different structures were added to the surface, a Ti:Au aperture mask and a glass super solid immersion lens (s-SIL).

Glass s-SILs were mounted onto the samples surface to increase the light output, and enhance the resolution of the μPL (for more information on this see chapter 2). The glass SILs used in this experiment were 1 mm in diameter and formed from LASFN-9 glass with a refractive index of 1.80 and a height of 800 μm , a side view can be seen in Figure 4.4.

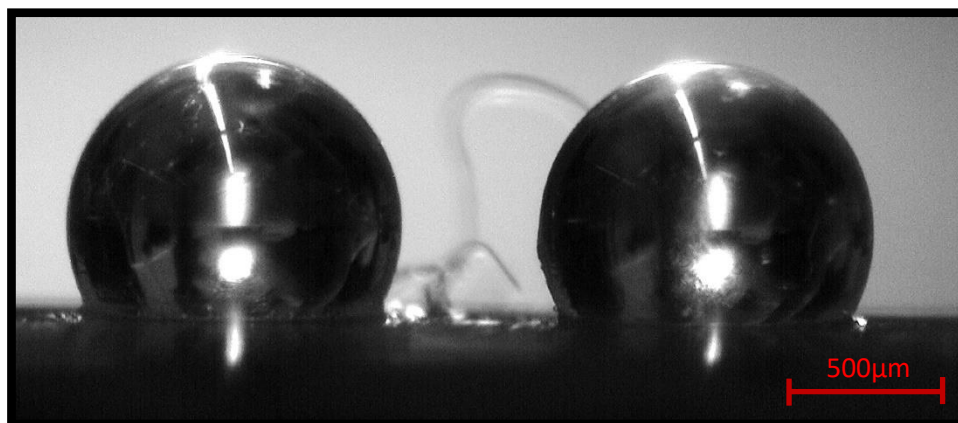


Figure 4.4: Side view of the glass SILs mounted on top of the GaSb/GaAs structures taking using an optical microscope.

Due to the cryostat having a vertical orientation the SIL had to be physically attached onto the sample. This was done using a UV cured epoxy with a closely matched refractive index (NOA 164). Applying epoxy in this way presents an additional challenge, as if the epoxy was too thick it would create a poor interface under the SIL which would show reduced PL (an example of this can be seen in Figure 4.6a). To improve this interface, a SIL mounting device was designed which would reduce the epoxy thickness; this can be viewed in Figure 4.5 with (a) and (b) showing a real image and schematic image respectively. A 1.5 μm thick layer of UV curable epoxy was spun onto the sample, and placed onto the X-Y stage along with a SIL. A glass slide with a 0.8 mm diameter nylon ring was then lowered onto the SIL. The purpose of the nylon ring was to grip the SIL and prevent it from moving while the X-Y stage is adjusted to the appropriate position using the microscope objective. Finally, the z-stage is moved down and the SIL is pressed hard into the sample to squeeze out the epoxy and make a very thin film, the SIL is then cured in place by exposing it to UV light. The results of this method can be seen by comparing Figure 4.6a showing a SIL mounted by hand and Figure 4.6b a SIL mounted using the above apparatus. The film is much thinner in b and more importantly much more uniform, although a faint colour sheen was still present suggesting that there remains some interference, which could affect the intensity of the observed PL. Overall the SIL was found to reduce the laser spot radius from 0.5 μm to approximately 0.3 μm, reducing the number of rings by approximately one order of magnitude from >100 to ~ 30.

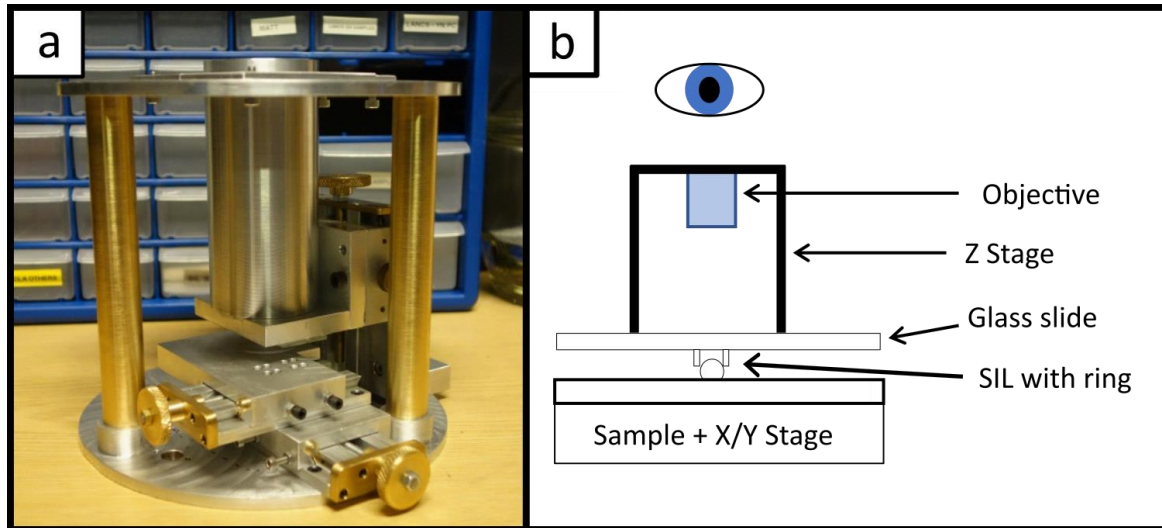


Figure 4.5: (a) showing a picture of the glass SIL mounting device, and (b) showing a schematic diagram of the device in (a)

The aperture mask was a 100 nm thick layer of gold (with a 10 nm Ti adhesion layer) deposited onto a photolithography patterned GaAs surface. The Au is then lifted off to leave 1 μm diameter apertures with some associated labels to allow each aperture to be easily located and can be observed in Figure 4.6d. This mask served multiple purposes, firstly it prevents light being emitted by structures outside of the excitation area, this effect occurs due to excitons migrating away from the laser spot through the GaAs before being captured. The mask also allowed individual exciton emissions to be easily relocated, allowing the same area to be observed multiple times, and any temperature induced drift of the sample corrected.

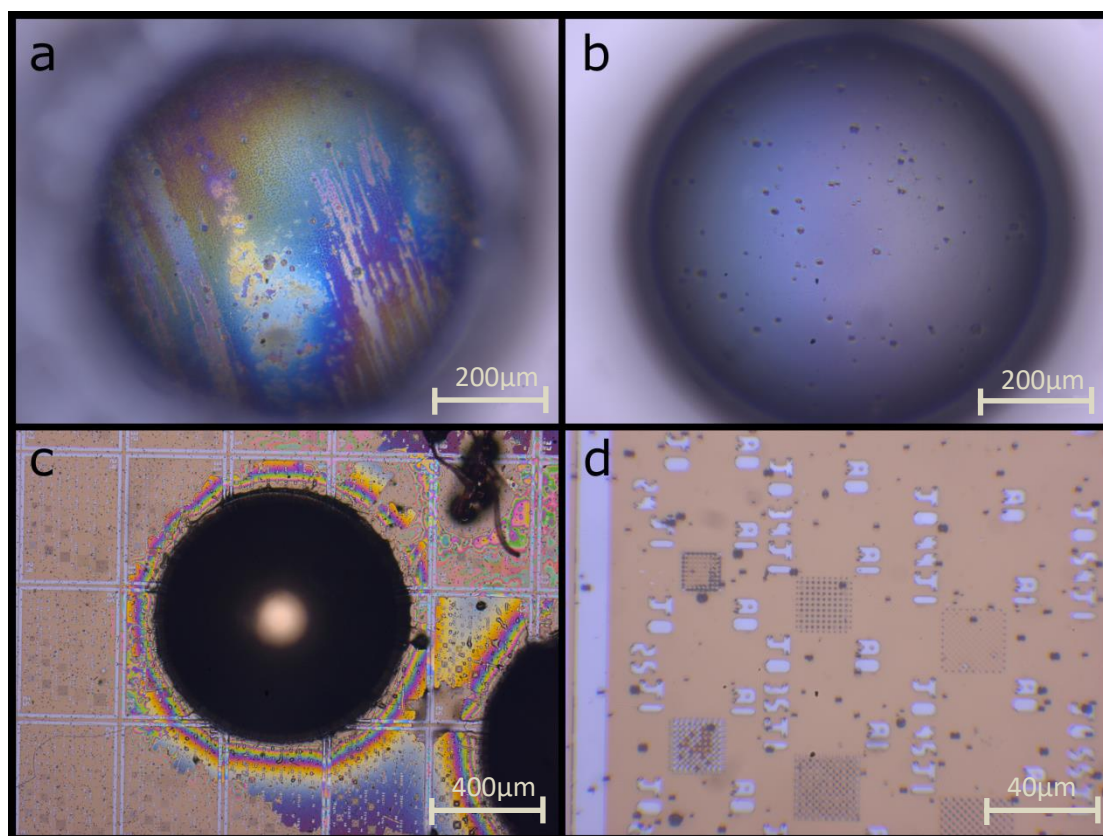


Figure 4.6: Microscope images showing glass *s*-SILs being mounted onto GaAs surfaces with **a-b**, showing the effect of having too thick a layer of epoxy, **(c)** showing the final glass SIL used in the experiment, and **(d)** showing a zoomed in view of the Au Aperture mask the SIL was mounted on.

4.2.2 μ PL Results

Figure 4.7 shows two high resolution μ PL spectra from the QRs sample shown in Figure 4.6c at low excitation power ($\sim 10 \mu\text{W}$) and at low temperature (20K). Previously, the PL at this power was indistinguishable from the noise whereas in these spectra we can clearly identify the peaks, demonstrating the effectiveness of the SIL at coupling light. The identified exciton peaks have a variety of linewidths, the sharpest of which were fitted with a Lorentzian fit and were found to be approximately $200 \mu\text{eV}$ in width. This is significantly wider than the linewidth observed for type-I QD systems such as InAs and InGaAs QDs, which can be an order of magnitude lower⁷. This increased width likely arises from two sources, the first effect may arise from charge noise causing fluctuating electric field around the QR resulting in a stark shift in the emission²⁷. In a type-II system such as the QRs the electrons and holes are spatially separated with only a small overlap in their wave functions and are therefore likely to be more sensitive to electric field perturbations than a type-I system. Charge fluctuations in the bulk around the QRs are also more likely due to there being clusters of GaSb around them arising from the random nature of the growth, which will trap charge carriers. Another source of increased linewidth may arise from the resolution of the μ PL system. When these measurements were taken the cryostat had a low frequency vibration of

amplitude ~ 300 nm, which can displace the sample from side with respect to the spectrometer. Light that successfully gets into the spectrometer travelling at even a slight angle can display a shift in wavelength due to the spectrometer being calibrated for light entering perpendicular. A slight vibration which moves the light from left to right may cause a slight shift in wavelength that broadens every exciton peak by a similar amount.

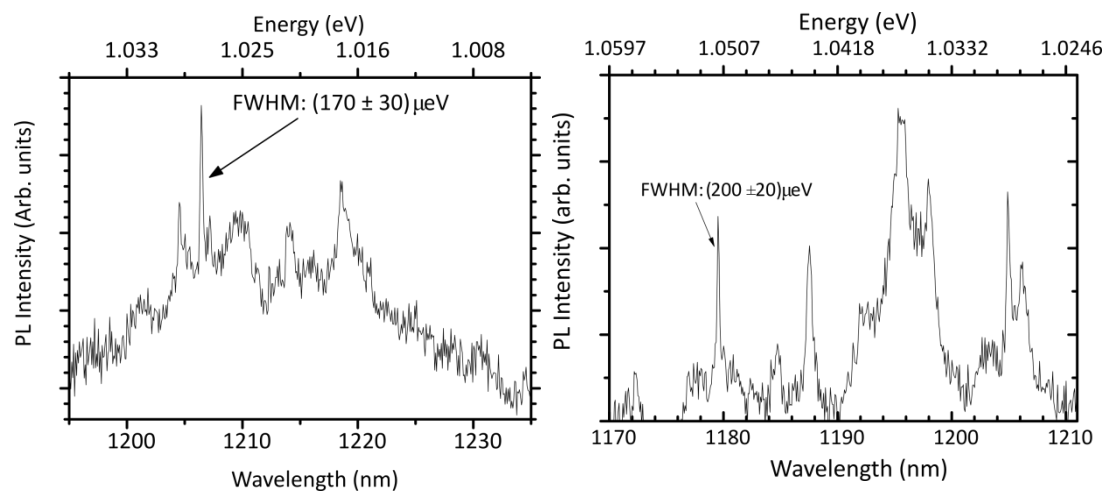


Figure 4.7: Two example micro-photoluminescence spectra of GaSb QRs taken at low excitation power, the resolution limited linewidth of the peak is displayed.

4.3 Power dependent blueshift

The ability to see individual exciton lines can be very useful to further our understanding of the origin of blueshift in these structures. As previously mentioned there are 3 different ideas on how blueshift with increased excitation power can arise, band bending, state filling and coulomb interactions. By monitoring the individual exciton peak positions with increasing excitation powers, we can gain a better understanding of how these different mechanisms contribute.

To investigate this effect, micro-photoluminescence (μ PL) spectra were taken at a range of different excitation powers spanning three orders of magnitude, and then normalised and plotted against each other (Figure 4.8). To quantify the blueshift a centre-of-mass (COM) fitting procedure was performed by integrating the μ PL spectra between 1100-1300 nm, then calculating which point on the spectra the half area falls (red line in Figure 4.8). This fitting procedure has been shown to be reliable for modelling the blue shift in bulk PL from previous work²⁸, and a direct comparison of the COM fit in μ PL to macro-PL is provided in Figure 4.9b. This can then be compared to the centre wavelength of individual exciton lines (blue line Figure 4.8), by fitting the QR peaks with a Lorentzian. Analysing Figure 4.8 it can be seen that the individual peaks (blue) stay roughly

constant in wavelength as excitation power is increased, whereas the COM (red) shows a reduction in the wavelength indicating an increase in emission energy of ~10 meV.

To better visualise the blueshift, the excitation power dependence of individual and COM peak fits were separately plotted in Figure 4.9a, against their peak energy. Analysing Figure 4.8/9, it is clear that the overall COM blueshift does not arise from the shift of the individual exciton lines, with there being virtually no change of energy within the resolution of the system. This negligible power induced shift of the exciton lines indicates that band bending cannot be providing a significant contribution to the observed blueshift, as any change to the bending of the bands would shift the energy levels of the potential well. This shift of ground state energy would as a result shift the energy of all the confined exciton states, however this is not observed. Instead an increase in excitation power appears to shift the overall centre of the ensemble peak. These findings are very similar to observations of InP/GaAs type-II quantum dots performed by Iikawa, et al. [29], who also showed that despite an overall ensemble shift the individual peaks from QDs remained constant.

This overall shift of the entire QR ensembles PL can therefore either arise from the filling of new higher energy states, or from the coulomb interaction creating a large amount of positive charge which results in a blueshift of the emission energy²⁵. State filling has previously been shown to not be a large effect in these structures with Young, et al. [28] showing that an increase in excitation power does not create a non-linear behaviour of the peak intensity, which would be expected if the higher energy states were being rapidly filled. Indeed, upon looking at the data in Figure 4.8, an increase in excitation power does not appear to yield new peaks at higher energy (this observation is representative of several different power dependences which were performed). Instead, a gradual shift in peak PL signature is detected which is believed to arise from the rings becoming increasingly charged with holes as excitation power is increased; as reported by Hayne, et al. [21]. This increased positive charge enhances the coulomb interaction between electrons and the positively charged lobes of the QR, causing the electron to be better confined in the GaAs resulting in an increase of emission energy when the exciton recombines. However, this build-up of charge near the material edges is precisely what will cause band bending to occur, and it is curious that this increased charging does not start to cause observable band bending effects. It is possible that at higher or lower excitation powers, band bending may still be occurring, however we were not able to resolve individual exciton peaks outside the excitation powers shown in Figure 4.8.

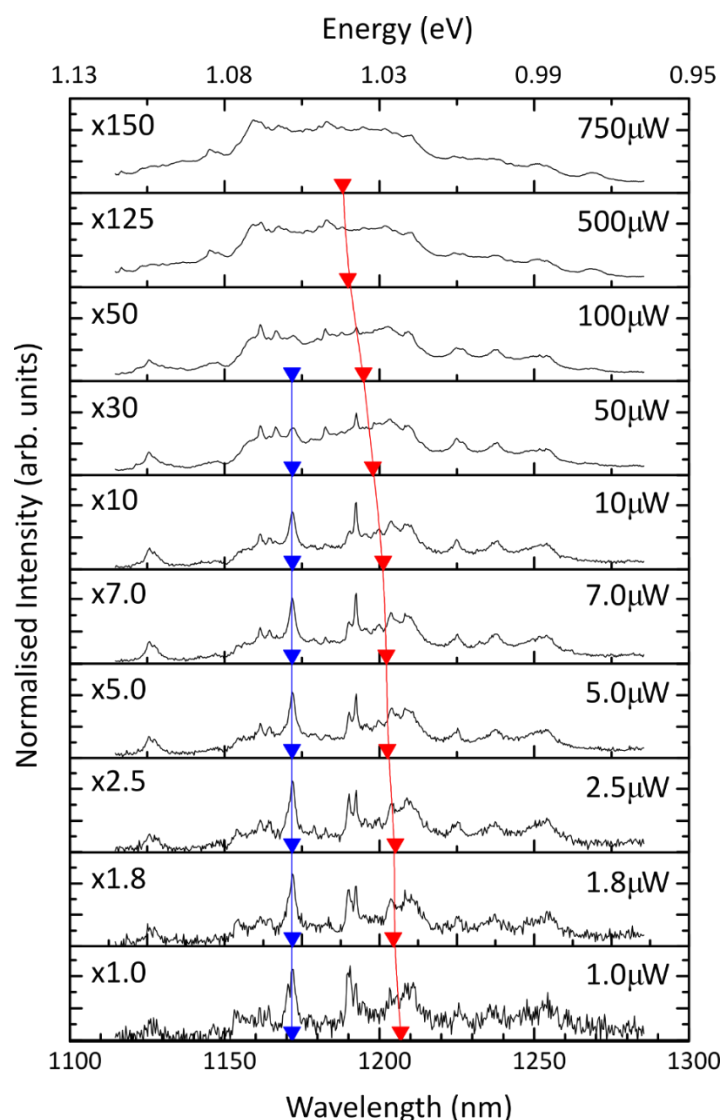


Figure 4.8: Normalised Micro-photoluminescence spectra from QRs as a function of laser power. The numbers on the left indicate the intensity before normalisation, the blue markers show the position of a single exciton peak calculated using a Lorentzian fit, the red markers show the centre position of the entire QD spectra.

The broad emission observed in the QR peak may arise from holes recombining with electrons which are poorly confined. Electrons that exist outside of the lobes of the ring are unconfined having a large number of states, therefore when they combine with a hole there can be significant variations in photon wavelength, which might lead to the broad peak observed. Electrons that exist in the centre of the rings however, are likely to experience 2D confinement from the Sb lobes that surround the ring centre. This confinement is likely to reduce the density of states of the electron leading to a reduction in the emission linewidth²⁸. It could therefore be possible that the tightly confined electrons in the centre of the ring are responsible for the sharp peaks, whereas the electrons outside the ring create the broad background.

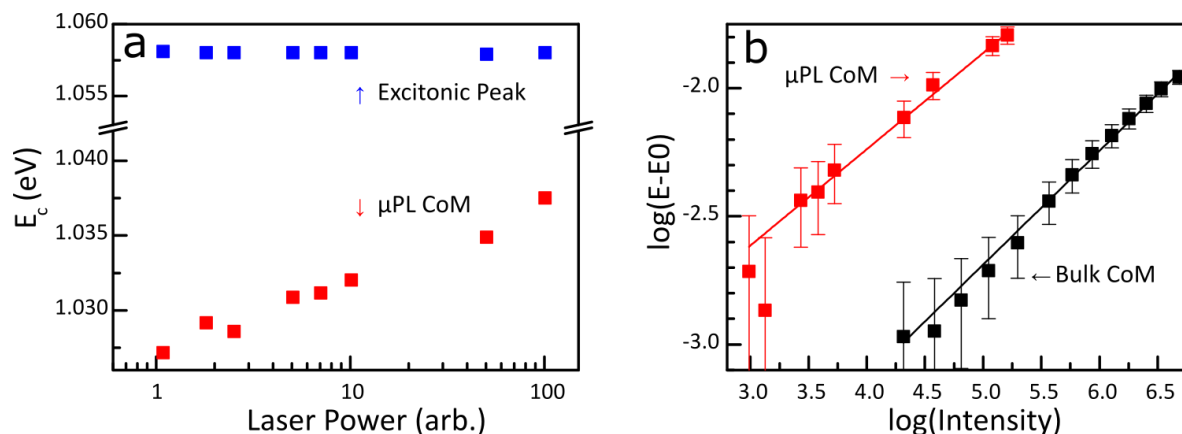


Figure 4.9: Graphs showing in (a) the change in energy of the COM and exciton peaks due to varying excitation power (as shown in Figure 4.8), and (b) showing the corrected centre of mass position ($E-E_0$) as a function of integrated intensity, for both Micro and Macro-Photoluminescence.

One significant question is whether the COM blueshift measured using μ PL is the same as that of a large ensemble of QDs measured in macro-PL. To investigate this, a piece of the same wafer was immersed in a continuous flow cryostat, and illuminated with an optical fibre giving a 1.6 mm diameter spot; a second fibre was then used to collect the spectra. The reason for using this setup over the closed cycle cryostat used for μ PL, was to reproduce results similar to previous work in this field^{8,21,25,30}, therefore eliminating any possibility that the measurement equipment was influencing the result. The PL spectra was measured over a wide range of excitation powers at 4.0K, then fitted using a Gaussian fit to find the peaks centre. The intensity was then plotted against the energy shift of the PL centre position ($E-E_0$) along with the μ PL COM fit, and can be seen in Figure 4.9b. The emission energy at zero excitation power (E_0) (the minimum transition energy), was calculated by linearly extrapolating the excitation power vs integrated intensity graph (Figure 4.9a) to zero. The reason for recovering this value from the data is due to E_0 being sensitive to unintentional doping, therefore each sample will have its own unique E_0 regardless of how similar the growth. A log-log scale was used to produce a linear fit of the data giving a gradient of 0.38 ± 0.04 for the μ PL and 0.44 ± 0.03 for the macro-PL. It can be seen that the two gradients agree within uncertainties showing a clear correlation between the blueshift in both regimes indicating that the mechanisms involved in the blueshift are highly similar. In fact the power densities used in this experiment were $0.03 - 15 \text{ Wcm}^{-2}$ for macro-PL and $3.6 - 2700 \text{ Wcm}^{-2}$ for μ PL suggesting that the blueshift is consistent over five orders of magnitude. The exponents themselves are somewhere between $1/3$ and $1/2$, but we expected from the theory that it should be closer to $1/2$ if the shift was mainly coulomb interactions. This is consistent with previous work done on these structures such as that performed by Hodgson, et al. [8], who showed that in type-II QR's exponents are lower than $1/2$. This is attributed by the authors to a breakdown of the bimolecular recombination approximation that is used when deriving

the exponents presented in the theory section. The work in this chapter thus seems to support their hypothesis, that in type-II QR structures the intensity is not proportional to the square of the number of holes.

4.4 Conclusions

In this chapter, we showed that individual type-II GaSb/GaAs quantum rings can be individually studied using micro-photoluminescence. To achieve this, an aperture mask and a glass solid immersion lens (SIL) were employed to reduce the excitation/emission area, and increase the light output coupling. Individual linewidths down to 200 μeV were detected in the quantum ring sample, however this may be resolution limited from the optical setup therefore it is possible that they are emitting with a narrower linewidth than this, but a better optical setup would be needed to test this theory.

The observation of individual exciton peaks made it possible to understand how they contribute to the ensemble power dependent blueshift that these samples exhibit. It was found that the individual lines do not change wavelength with excitation power, instead weaker peaks at shorter wavelengths became gradually more intense than the longer wavelengths. This suggests that the cause of the power dependent blueshift in these samples is not due to band bending but instead is either caused by an asymmetric coulomb charging effect, or state filling. The magnitude of each effects contributions was not elucidated in this study, however from previous literature²⁸ it is expected that the contribution of state filling is low. Fully understanding the physics behind this blueshift is important when designing optical devices such as lasers, and LEDs out of QRs, as any shift in wavelength can ruin the effectiveness of an optical cavity.

A remaining question is whether the spikes observed are confined enough to be a single photon source. To further explore this it would be necessary to see if the emitted photons show signs of anti-bunching, which can be found by performing a Hanbury Brown-Twiss experiment²⁴. A few attempts were made to perform this; however, it was very difficult to detect the QR emission due to the signal being weak and the peaks broadening significantly with high excitation powers. Furthermore, cryostat drift and background light placed limits on how long the detectors could be left exposing; which meant that light from these individual peaks could not be detected. In the future it would be useful to perform this experiment again with a better laboratory environment with a more stable cryostat and more sensitive detector.

An interesting future direction for this work would be to try and isolate a single QR in a tuned micro-cavity. This could be accomplished during MBE growth by growing GaAs/AlAs mirror pairs

above and below the active region, then after growth patterning the substrate then etching it into freestanding pillars. The quantum rings in these tuned pillars should benefit from a Purcell enhancement that would make their exciton peaks a lot brighter. These brighter sources would allow an anti-bunching experiment like the one mentioned above to be performed, allowing their suitability as a single photon source to be assessed.

4.5 References

- 1 Bimberg, D. & Pohl, U. W. Quantum dots: promises and accomplishments. *Materials Today* **14**, 388-397, (2011).
- 2 Unitt, D. *Enhanced single photon emission from a quantum dot in a semiconductor microcavity*, Cambridge, (2005).
- 3 Sonia, B., Kelley, R. & Jelena, V. Engineered quantum dot single-photon sources. *Rep. Prog. Phys.* **75**, 126503, (2012).
- 4 Schlehahn, A. *et al.* Generating single photons at gigahertz modulation-speed using electrically controlled quantum dot microlenses. *Applied Physics Letters* **108**, 021104, (2016).
- 5 Unitt, D. C. *et al.* Quantum dots as single-photon sources for quantum information processing. *Journal of Optics B: Quantum and Semiclassical Optics* **7**, S129, (2005).
- 6 Rivoire, K. *et al.* Fast quantum dot single photon source triggered at telecommunications wavelength. *Applied Physics Letters* **98**, 083105, (2011).
- 7 Valéry, Z., Thomas, A. & Oliver, B. Quantum optics with single quantum dot devices. *New Journal of Physics* **6**, 96, (2004).
- 8 Hodgson, P. D. *et al.* Blueshifts of the emission energy in type-II quantum dot and quantum ring nanostructures. *J. Appl. Phys.* **114**, 073519, (2013).
- 9 Liu, H., Wang, Q., Chen, J., Liu, K. & Ren, X. MOCVD growth and characterization of multi-stacked InAs/GaAs quantum dots on misoriented Si(100) emitting near 1.3 μm . *J. Cryst. Growth* **455**, 168-171, (2016).
- 10 Krier, A., Huang, X. L. & Hammiche, A. Liquid phase epitaxial growth and morphology of InSb quantum dots. *Journal of Physics D: Applied Physics* **34**, 874, (2001).
- 11 Nicoll, C. A. *et al.* MBE growth of In(Ga)As quantum dots for entangled light emission. *J. Cryst. Growth* **311**, 1811-1814, (2009).
- 12 Bimberg, D., Grundmann, M. & Ledentsov, N. N. *Quantum dot heterostructures*. (John Wiley, 1999).
- 13 Watanabe, S. *et al.* Dense uniform arrays of site-controlled quantum dots grown in inverted pyramids. *Applied Physics Letters* **84**, 2907-2909, (2004).
- 14 García, J. M. *et al.* Intermixing and shape changes during the formation of InAs self-assembled quantum dots. *Applied Physics Letters* **71**, 2014-2016, (1997).

- 15 Kobayashi, S., Jiang, C., Kawazu, T. & Sakaki, H. Self-Assembled Growth of GaSb Type II Quantum Ring Structures. *Jpn. J. Appl. Phys.* **43**, L662, (2004).
- 16 Timm, R. *et al.* Self-Organized Formation of GaSb/GaAs Quantum Rings. *Physical Review Letters* **101**, 256101, (2008).
- 17 Smakman, E. P. *et al.* GaSb/GaAs quantum dot formation and demolition studied with cross-sectional scanning tunneling microscopy. *Applied Physics Letters* **100**, 142116, (2012).
- 18 Klenovský, P., Steindl, P. & Geffroy, D. Excitonic structure and pumping power dependent emission blue-shift of type-II quantum dots. *Scientific Reports* **7**, 45568, (2017).
- 19 Hatami, F. *et al.* Radiative recombination in type - II GaSb/GaAs quantum dots. *Applied Physics Letters* **67**, 656-658, (1995).
- 20 Marent, A. *et al.* $10^{(6)}$ years extrapolated hole storage time in GaSb/AlAs quantum dots. *Applied Physics Letters* **91**, 242109, (2007).
- 21 Hayne, M. *et al.* Electron localization by self-assembled GaSb/GaAs quantum dots. *Applied Physics Letters* **82**, 4355-4357, (2003).
- 22 Lin, S.-Y. *et al.* Room-temperature operation type-II GaSb/GaAs quantum-dot infrared light-emitting diode. *Applied Physics Letters* **96**, 123503, (2010).
- 23 Lin, W.-H., Wang, K.-W., Chang, S.-W., Shih, M.-H. & Lin, S.-Y. Type-II GaSb/GaAs coupled quantum rings: Room-temperature luminescence enhancement and recombination lifetime elongation for device applications. *Applied Physics Letters* **101**, 031906, (2012).
- 24 Hanbury Brown, R. & Twiss, R. Q. The Question of Correlation between Photons in Coherent Light Rays. *Nature* **178**, 1447-1448, (1956).
- 25 Young, M. P. *et al.* Photoluminescence studies of individual and few GaSb/GaAs quantum rings. *AIP Advances* **4**, 117127, (2014).
- 26 Vamivakas, A. N. *et al.* Nanoscale Optical Electrometer. *Physical Review Letters* **107**, 166802, (2011).
- 27 Houel, J. *et al.* Probing Single-Charge Fluctuations at a GaAs/AlAs Interface Using Laser Spectroscopy on a Nearby InGaAs Quantum Dot. *Physical Review Letters* **108**, 107401, (2012).
- 28 Young, R. J. *et al.* Optical observation of single-carrier charging in type-II quantum ring ensembles. *Applied Physics Letters* **100**, 082104, (2012).
- 29 Iikawa, F. *et al.* Optical properties of type-I and II quantum dots. *Brazilian Journal of Physics* **34**, 555-559, (2004).
- 30 Carrington, P. J. *et al.* Long-Wavelength Photoluminescence from Stacked Layers of High-Quality Type-II GaSb/GaAs Quantum Rings. *Crystal Growth & Design* **13**, 1226-1230, (2013).

Chapter 5

Integration of III-V based type-II QDs with silicon

This chapter looks at the integration of telecoms wavelength emitting InAs/GaAs quantum dots, with silicon (Si). Photoluminescence (PL) measurements on two samples were performed, with one grown on silicon with defect filter layers (DFLs) grown underneath the active region, and the other grown on a Gallium Arsenide (GaAs) substrate. Individual quantum dots on both samples were isolated using both micropillars and gold apertures.

5.1 Introduction

In the previous chapter we studied the near infra-red (NIR) emission of GaSb/GaAs quantum rings, which had emission up to 1300 nm. These emission wavelengths make them suitable for integration with fibre optic networks due to their emission lying within a low loss region for silica fibres 1260-1360 nm (O-band). In this window scattering and chromatic dispersion are highly reduced, making these wavelengths good for telecoms¹. However, QRs are unlikely to be adopted for telecoms due to their wavelength being too short to be enhanced by erbium doped fibre amplifiers (EDFA) which produce gain in the 1550 nm region². These amplifiers have been a key enabling technology for fibre communication³, therefore it is desirable that future telecom light sources emit in the C-band (1530-1565 nm).

InAs/GaAs quantum dots are one of the most extensively studied quantum dot systems⁴, they emit at 780–1300 nm⁵ and are type-I which makes them optically bright making them excellent single photon sources⁶, but their short wavelengths make them unsuitable for long distance telecoms. InAs QDs can however be capped with GaAsSb to give them a much longer emission wavelength shifting it to over 1500 nm, placing them in the telecoms C-band⁷. These structures like the GaSb/GaAs structures are type-II in their band alignment and have been shown to emit at room temperatures⁸⁻¹¹. Like quantum rings their type II band alignment arises due to the Sb in their capping layer, the only difference is that in this system the carrier's state of confinement is opposite, with the holes loosely confined in the cladding layer and the electrons tightly confined within the dot as shown in Figure 5.1.

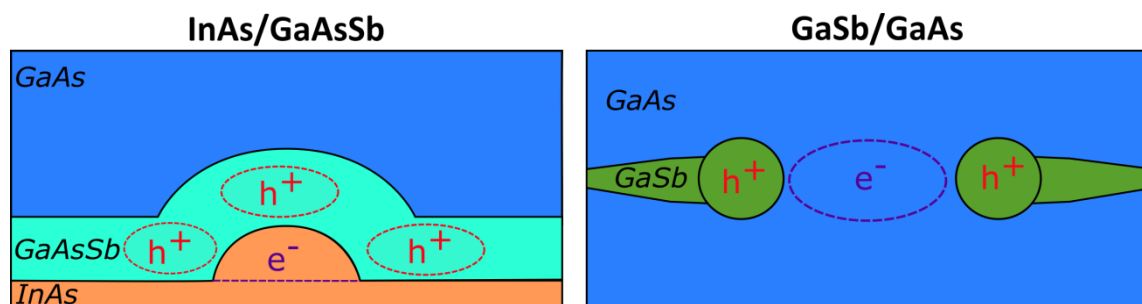


Figure 5.1 – Simple cross-sectional diagram showing the structure of a InAs/GaAs quantum dot, showing localised electrons and delocalised holes in the GaAsSb cap, compared to a GaSb quantum ring with holes localised in the lobes of the ring and delocalised electrons in the GaAs centre.

These GaAsSb capped InAs QDs seem an ideal candidate for a future telecoms single photon source. If they could be integrated into silicon electronics, they would be ideal for use in applications such as optical networks-on-chip¹². To achieve this GaAs would need to be grown on silicon, however this is a problem as these materials have a large lattice mismatch (4.2%) and different thermal expansion coefficients, which lead to threading dislocations and other interfacial defects to form in the GaAs^{13,14}. The dislocations can propagate through the structure, up into the InAs quantum dot layer and act as sites for excitons to be captured, greatly reducing the emission intensity due to the excitons recombining non-radiatively. Therefore, if InAs/GaAs quantum dots are to be integrated with Si, a solution needs to be found to greatly reduce/remove these dislocations. Additionally, due to Si and GaAs being polar/non-polar GaAs, grown on Si forms antiphase domains which results in a poor crystallinity, however a simple two process growth has been shown to solve this problem¹⁵.

One method known to reduce dislocations is to grow dedicated layers between the Si interface and the active region called dislocation filter layers (DFLs)¹³. DFLs are sets of strained superlattices which bend propagating dislocations into the growth plane so that they meet and annihilate each other¹⁶. These have been shown to greatly improve room temperature photoluminescence of InAs quantum dots grown on silicon, with Yang, et al. [17] demonstrating that emission can be improved from less than 10% to 50% of the intensity of a InAs dot grown on a GaAs wafer.

In this chapter, micro-photoluminescence was used to observe exciton emission originating from GaAsSb capped InAs/GaAs quantum dots grown on Si with three DFLs between the wafer and the active region. This sample was then compared to identical dots grown on a GaAs wafer to ascertain the effectiveness of DFLs when used with a type-II QD system. Single QDs on these samples were isolated using micropillars/aperture masks to reduce the number of excited QDs, enabling the study of individual quantum dot emission.

5.2 Sample structure details

In this work two samples with identical active regions were grown using MBE, one on a silicon substrate, the other on a GaAs substrate. The active region consisted of 50 nm of GaAs followed by the InAs QD layer, a 6 nm cap of GaAs_{0.74}Sb_{0.26} was then grown over the dots, which was followed by 50 nm of GaAs. The active region was additionally clad with 100 nm of AlGaAs. The wafer grown on silicon had additional growth underneath the active region, consisting of an initial 1000 nm of GaAs then 3 DFL layers which consist of superlattices of 10 nm In_{0.18}Ga_{0.82}As and 10 nm GaAs. Each DFL had 5 repeats and a 350 nm GaAs spacer separating them. A cross-sectional render of the structure is shown in Figure 5.2; further details on the growth of the sample are outside of the scope of this work, therefore for more information on growth please see Orchard, et al. [18].

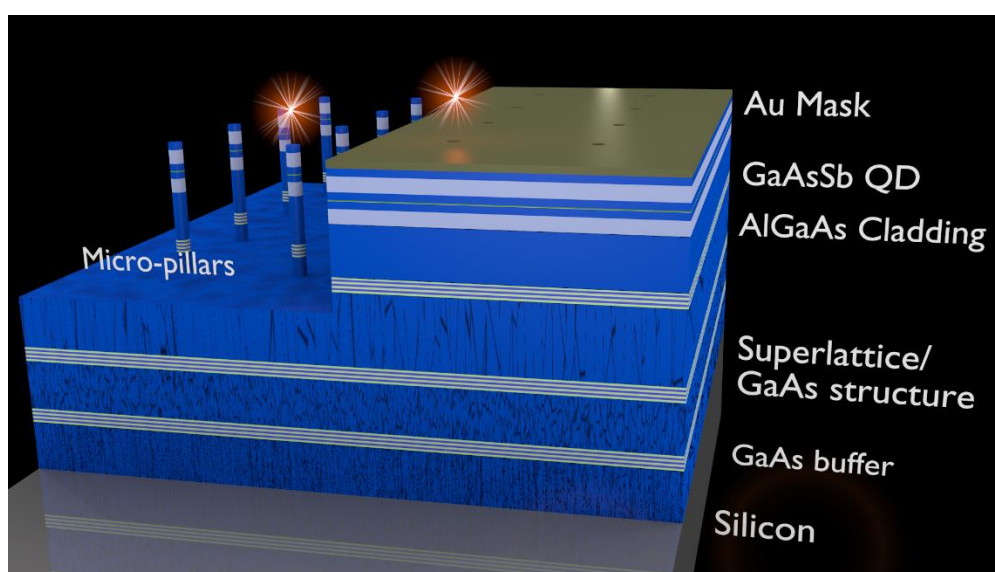


Figure 5.2 – Diagram showing a cross-sectional image of the growth structure

Figure 5.3a shows a transmission electron microscope (TEM) cross-sectional image of a single quantum dot approximately 8 nm high and 23 nm wide, grown on the GaAs wafer. The InAs quantum dot is highlighted by a dashed line, the bright band around the dot is the GaAsSb cladding layer. It can be seen that there is a non-uniform ring like structure of the capping layer that has formed around the dot, this has likely formed from material migrating away from the apex of the dot to reduce strain. It was found from energy-dispersive X-ray spectroscopy (EDS) studies that there was an additional migration of In out of the QD into the cladding layer.

Figure 5.3b shows an AFM image of uncapped InAs QDs grown in the same way as the capped sample. It can be seen in the image that there are two distinct sizes of QDs that have formed small and large. This growth is dense with the small QDs having a density of $80 \mu\text{m}^{-2}$ and the large QDs $5 \mu\text{m}^{-2}$; this means that standard micro-PL will excite hundreds of structures making individual lines difficult to observe. The sample in the AFM was grown on Silicon, however there should be no

significant difference in the structural composition of the GaAs and the Si grown samples due to the amount of GaAs grown between it and the wafer.

The size and distribution of the quantum dots is interesting as other studies of GaAsSb capped InAs/GaAs structures have shown no sign of smaller dots just the larger QD sizes.¹⁹ This binominal distribution is independent of the capping layer, and arises from the growth of the InAs QDs. This binominal growth has been shown in other literature to be tuneable by a varying growth temperature^{20,21}, and In flux²². This means that it should be possible to both increase the uniformity, and reduce the density of QDs with a change of growth recipe; high quality InAs QDs with similar sizes have been grown with densities of $1 \mu\text{m}^{-2}$ and less^{23,24}.

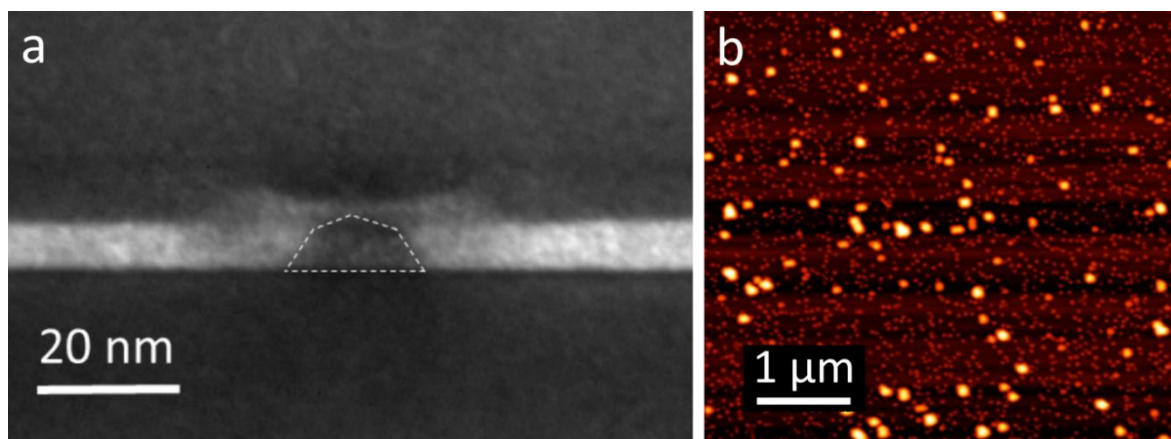


Figure 5.3 – (a) TEM cross sectional image of a single InAs QD with its GaAsSb cap (white region), and (b) showing an AFM image showing uncapped QDs grown on the surface. (These images were obtained from fellow collaborators R. Beanland of Warwick (a) and M. Tang of UCL (b)).

5.3 Macro- PL results

Initially a wide spectral range macro-photoluminescence measurement was performed at 70K using a 638 nm laser (spot diameter $\sim 200 \mu\text{m}$) and is shown in Figure 5.4. This was performed so the entire NIR emission could be analysed to see how the emission varied between the samples, for different excitation powers. Several different features can be seen in these spectra the most important of which is the 1500 nm peak which is attributed to the large InAs QDs seen in Figure 5.3. This peak being present in both the GaAs and the silicon wafer shows that telecom wavelength emission is possible from InAs QDs grown on silicon. There is a very slight reduction in the peak emission wavelength from the growth on silicon of a few nm, which is attributed to the residual strain in the structure arising from the different thermal expansions of GaAs and Si when at low temperatures.

We also observe that the PL intensity from QDs on the GaAs wafer (a) is 20 times higher than that of QDs on the Si wafer, which suggests that even though the DFLs are reducing the amount of dislocations some are still propagating through the active region. This is further supported by analysing the other peaks at 920nm, 1070nm and 1200nm. The 920nm and 1200nm peaks are attributed to the InAs wetting layer, and the GaAsSb cladding layer respectively. The 1070 nm peaks arise from the smaller InAs quantum dots and are brighter than the larger dots in (a) due to their higher density¹⁸. Comparing (b) to (a) the peaks attributed to QWs are greatly reduced becoming indistinguishable from the broad background, whereas the peaks attributed to QD emission are a lot less effected, and are still easily observable. This behaviour is consistent with dislocations being present in the active region, as in a QW carriers are able to migrate in-plane until they reach a dislocation where they can recombine non-radiatively. This is not the case in a QD due to carriers being more spatially confined, preventing exciton migration after capture. When looking at the ratio between (a) and (b) (inset of a) it can be seen that the large quantum dots are less affected by the presence of dislocations than the smaller set, this is most likely due to the larger quantum dots having a deeper confinement potential than the small dots, therefore having a strong barrier to prevent migration out of the QD.

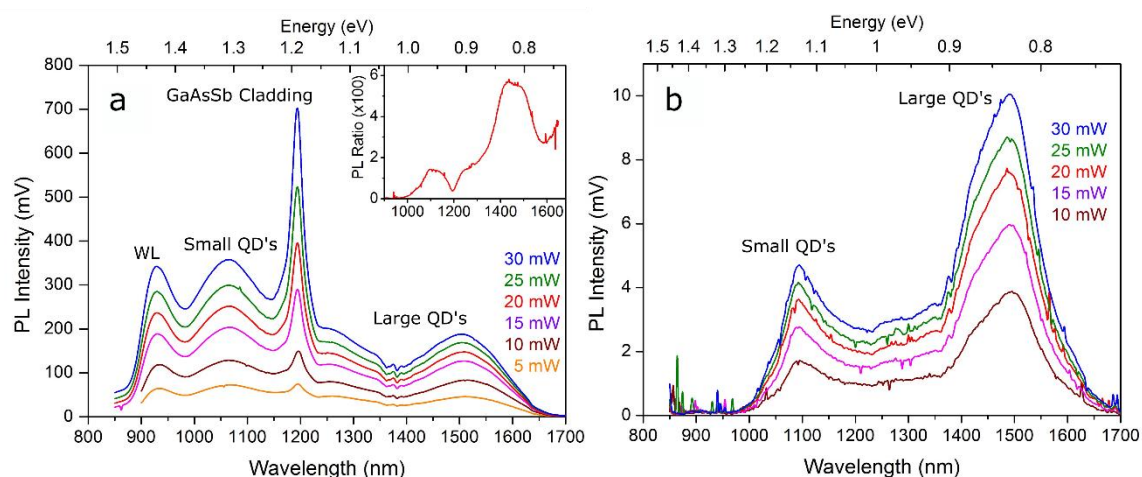


Figure 5.4 - Power dependent photoluminescence spectra from GaAsSb capped InAs/GaAs QDs at 70K, grown on a GaAs wafer (a) and a Silicon wafer (b). Inset of (a) shows the ratio of the Silicon to the GaAs. (This data was collected and plotted by collaborator J. Orchard, et al. [18]).

5.4 Isolating individual dots

5.4.1 Micropillars

Upon performing initial micro-photoluminescence (μ PL) measurements it became immediately clear that the high QD density made individual excitons very hard to spot due to a broad ensemble of lines and a high background signal. To reduce the excitation area, 1 μ m diameter micropillars with 5 μ m spacing's were patterned into the sample using e-beam lithography (EBL) followed by plasma etching using an inductively coupled plasma (ICP). The micropillars are smaller than the excitation area, reducing the number of quantum dots observed. Additionally, any quantum dots near the edge of the pillar are less likely to emit due to carriers being scattered by the micropillars etched surface. An example SEM image of the etched micropillars can be seen in Figure 5.5, the pillars were etched to a depth of approximately 500 nm.

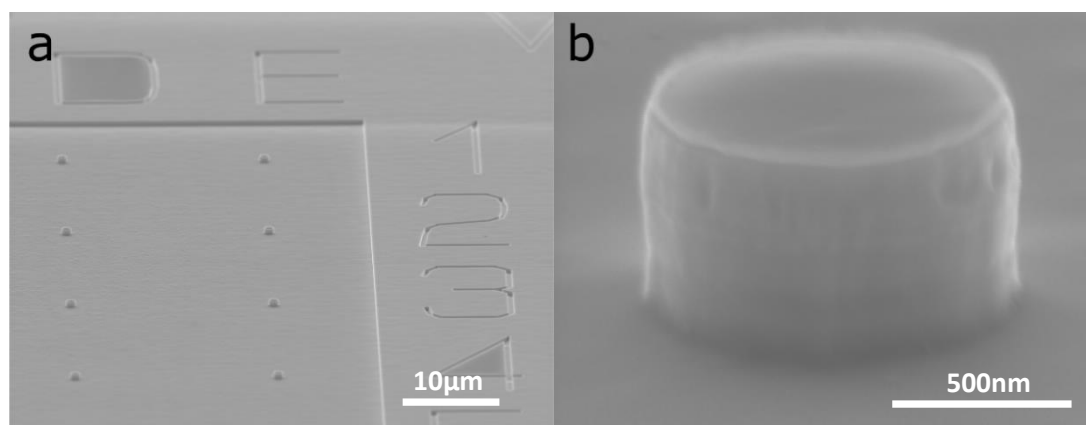


Figure 5.5 - SEM image showing (a) an array micropillars and (b) a single micropillar etched into the active region.

Micro-photoluminescence measurements were taken from multiple pillars at 20K using the setup described in the methods, and two example low power spectra for both GaAs (a) and Si (b) substrates are shown in Figure 5.6. Comparing (a) to (b), as expected the QDs on the Si have a reduced intensity and require an order of magnitude increase in excitation power to achieve similar emission intensities. All spectra show peaks around 1500 nm on a broad background, each of these peaks is attributed to an individual QD in the micropillar, albeit significantly broadened. The FWHM of these peaks show a range of values between 1 – 5 meV with the Si showing more broadening than the GaAs. This is a lot broader than normal type-I InAs quantum dots which have linewidths closer to 10 μ eV²⁵. Some of this broadening arises from the type-II nature of the system, causing localised electric fields and a large QCSE, similar to the QRs in chapter 4. However, the linewidths are 10 times broader than the QRs which are also type-II, suggesting that this broadening cannot be explained simply by its type-II nature. It is therefore likely that there are additional charge fluctuations in the vicinity of the QDs, which may arise from multiple different sources such as inhomogeneous growth or surface states.

The linewidths measured from the Si-substrate samples tend to be broader than the GaAs which can be attributed to the 10x increase in laser power, and possibly from inhomogeneous broadening due to the sample being broken up slightly by defects. In fact, the dislocations can be clearly identified in the pillars, with some pillars showing much lower PL than others. This can be clearly seen in (b) where Pillar 3's peak intensity is 8x brighter than Pillar 4 despite being neighbouring pillars and having identical excitation.

It can also be seen from looking at Figure 5.6 that there is a broad background emission which partly obscures the individual lines. This background is present even at low excitation powers and can completely hide the QD peaks at high excitation. This suggests excitons are recombining radiatively outside the quantum dots. The cause of this is unknown; however, it appears to be an issue with both the GaAs and the Si substrates, suggesting that like the high density of small QDs it is an issue arising from the growth of the active region rather than the Si substrate.

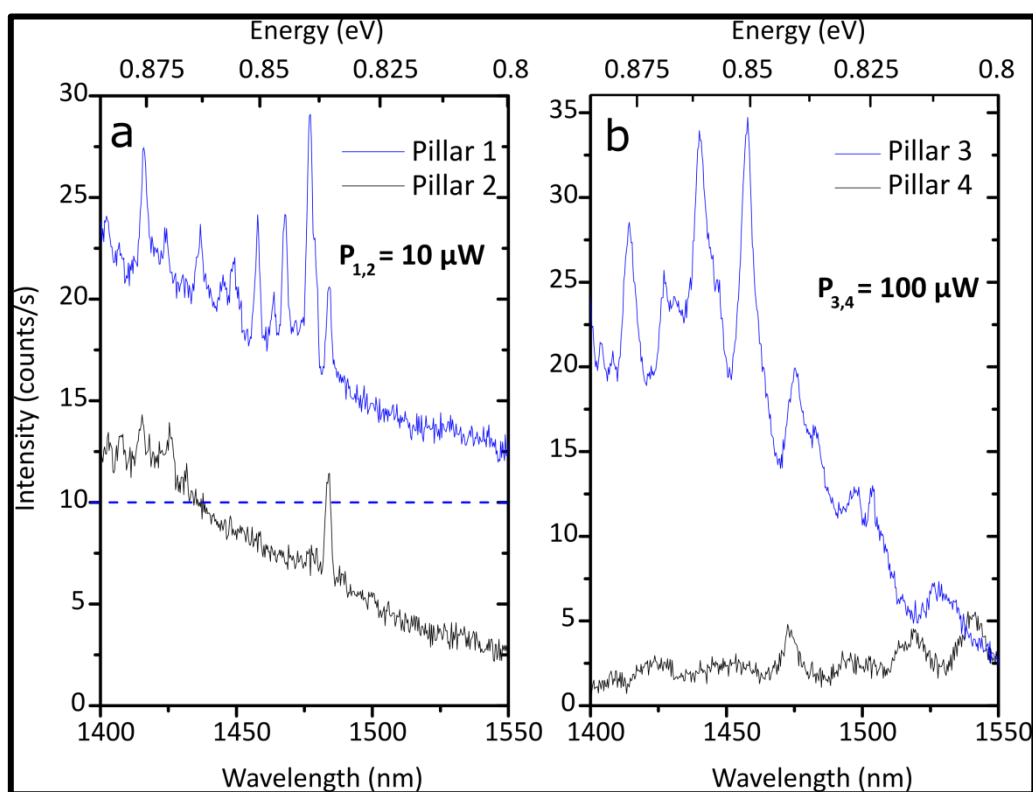


Figure 5.6 - Photoluminescence spectra for different micropillars at 20K, showing exciton emission from InAs/GaAs QDs grown on a GaAs substrate (a) and a Silicon substrate (b). NB: Pillar 1 is offset from Pillar 2 for clarity; the blue dashed line marks its offset zero.

5.4.2 Apertures

When looking at the relatively broad linewidths observed in Figure 5.6, it was proposed that this broadening might arise from charge fluctuations in the vicinity of the quantum ring. These could

arise from two possible sources, either inside the bulk of the semiconductor from charge being trapped in sites around the quantum dots, or from surface states that occur around the micropillar due to etching. Surface states have been found to decrease the Q-factor of micropillars, due to charge fluctuations²⁶, therefore these small micropillars might be a source of the broadening. To explore the effects of this a Ti/Au aperture mask similar to the one in chapter 4, was thermally evaporating on-top of both GaAs and Si samples. Electron Beam Lithography (EBL) was used to pattern the resist, to enable apertures of the same dimensions as the pillars to be formed (see Figure 5.7). The opaque metal mask prevents light emission from anywhere but the aperture, and does not cause any edge states to form.

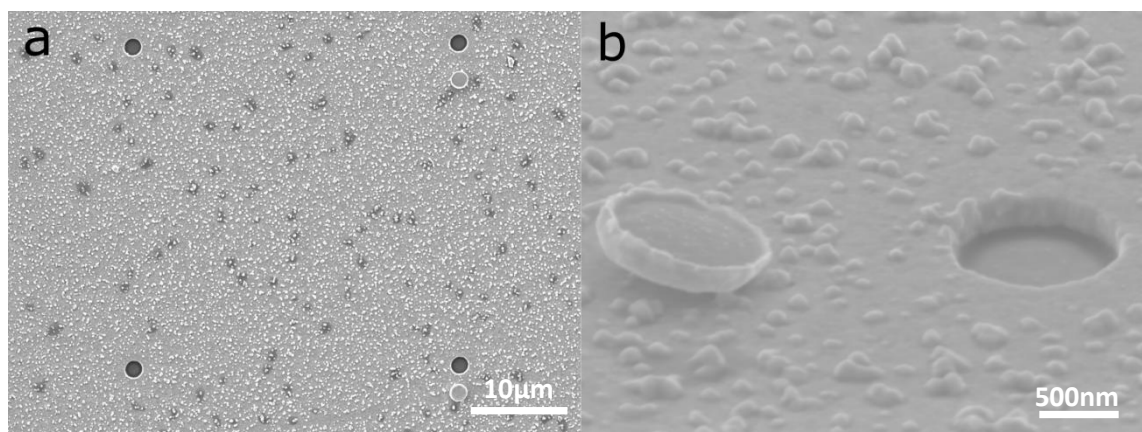


Figure 5.7 – SEM images showing the lifted off gold covered apertures with (a) showing the array, and (b) showing an individual aperture up close with the removed gold still present on the left of the image.

Figure 5.8 shows two example μ PL spectra (a), (b) from apertures on GaAs and Si-substrates respectively, both taken using the same excitation power (200 μ W). Both samples spectra show sharp lines similar to the micropillars, however rather than a reduced linewidth they are slightly broader with FWHM ranging from 2 – 5 meV, with once again the Si substrate sample showing reduced intensity and increased broadening. It can be seen that these samples required much higher excitation powers to achieve a similar intensity to that from the pillar samples, which may indicate that there is a poor coupling efficiency of light into and out of the apertures. The slight increase in broadening may therefore arise simply from the higher laser power used to excite the structures, as these samples all show significant broadening with excitation powers.

These results therefore give no evidence to suggest that surface states are having a large effect on the linewidth, with the emission from the apertures showing no significant reduction. It is therefore likely that this broadening is an effect which originates in the bulk semiconductor around the quantum dots. Whereas it is impossible to determine the exact causes it is possible to speculate, based on what we know of the growth. From analysing the TEM images in Figure 5.3 there are

thickness fluctuations of the GaAsSb capping layer where the holes are confined. These fluctuations can affect the local electric field around the hole, which in turn can affect how the hole recombines, possibly broadening the emission. Additionally, from EDS measurements of similar samples it is clear that Antimony (Sb) can migrate through the lattice to create non-uniform distributions²⁷, which can lead to alloy fluctuations, which are theoretically predicted to effect linewidths of radiative transitions²⁸.

Another possibility is that some of the broadening arises from a spectral diffusion effect due to impurities or structural defects around the QD that come from the growth of the active region²⁹. Large quantum dots are known to have generally broader linewidths, being more vulnerable to strain related defects³⁰ and inter-dot coupling when grown next to high densities of small quantum dots³¹. Both of these effects could be minimised by more optimised lower density growth, additionally resonant excitation may help at reducing the effect of defects trapping excitons.

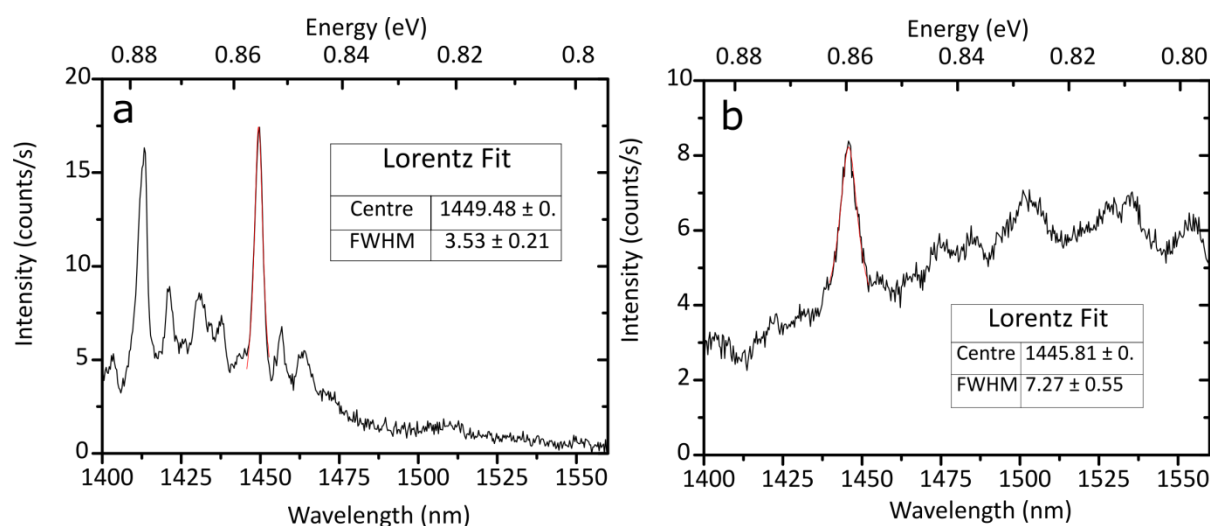


Figure 5.8 – Micro-Photoluminescence spectra of the QDs observed through gold apertures, with (a) showing the GaAs substrate and (b) showing the Si.

5.4.3 Power Dependence

To explore the type-II nature of these QDs PL was performed for a range of excitation powers, one of these power dependence spectra is shown in Figure 5.9. This power dependence was performed on the GaAs-substrate sample due to its brighter exciton emission. Since both have identical active regions and similar PL at 1500 nm these results should be indistinguishable from the Silicon substrate, but are significantly easier to obtain due to the increase in their efficiency. However, to ensure this was the case a quick power dependence on the Si was performed and showed similar results, but with significantly higher noise.

The centre of mass of the exciton emission (shown in Figure 5.9a) was found to blueshift with excitation power with significant broadening of the individual peaks at high excitation powers. However, the individual lines were found to be relatively independent of excitation power, with only a slight red shift observed (as shown by the red data plotted in Figure 5.9b). This is very similar to what we reported for the type-II QRs in the previous chapter (Figure 4.8), where we concluded that band bending was not playing a significant role, due to no blueshift occurring to the individual QD peaks. This similarity is interesting as these QD structures are very different in terms of the confinement of their carriers; the GaAsSb capped InAs/GaAs QDs have tightly confined electrons with loosely confined holes, the inverse of the situation in GaSb/GaAs QRs. However, it can be seen in Figure 5.3a that there is a ring like structure that has formed around the QD, which from EDS has shown to be high in Sb. It is possible that this structure might be loosely confining holes, which is overall creating a system similar to the QRs, which could account for the similarities in the power dependence.

The blue line in Figure 5.9b shows the total intensity of the 1450 nm peak with excitation power. Its linear dependence on a log-log scale at the lower powers then saturation upon reaching higher powers is consistent with single exciton recombination. No lines representing multi-excitonic recombination were observed in any spectra from the sample, although it is possible these were obscured by the broad background peak.

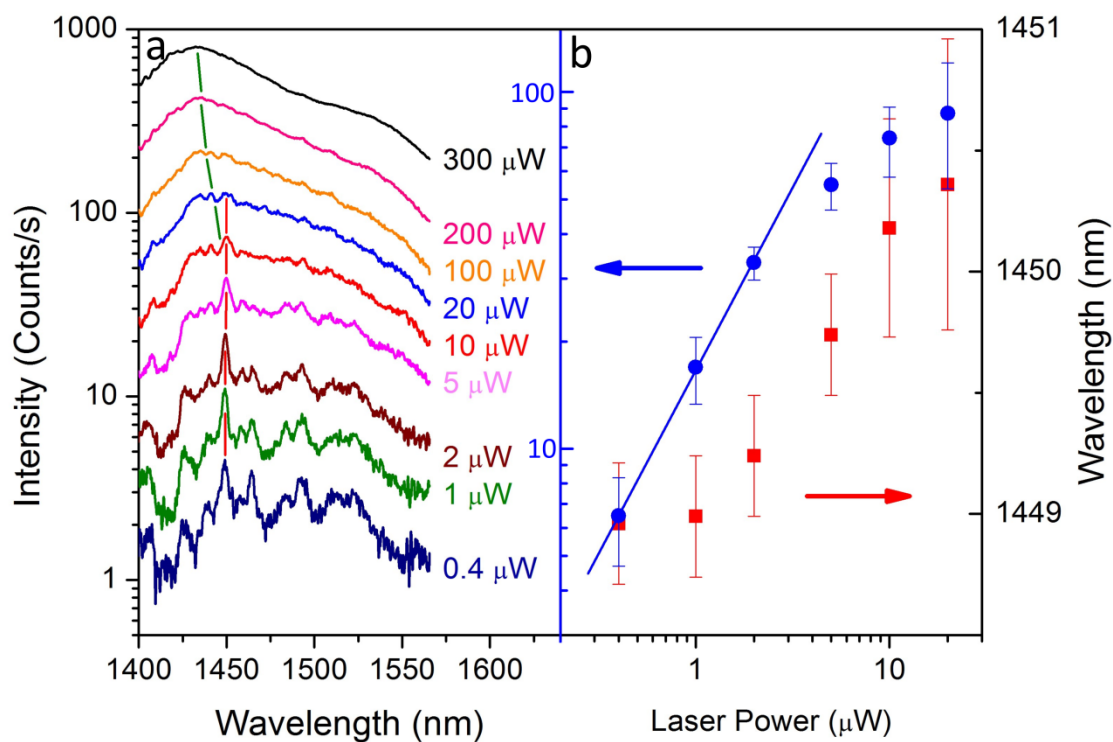


Figure 5.9 – (a) Micro-Photoluminescence spectra of the QD peak as a function of laser power, red/green lines show the change of the individual/ensemble peak respectively, with varying excitation power. (b) Plots the 1450 nm peak's total intensity (blue) and the peak wavelength (red) as functions of excitation power on a log scale.

5.5 Conclusion

Type-II GaAsSb capped InAs/GaAs QDs grown on Silicon and containing DFL's were studied to see if dislocations due to the GaAs/Si lattice mismatch could be reduced sufficiently to allow emission. The same quantum dots were grown on both a GaAs and a Si substrate to allow the DFL's effectiveness to be assessed. The QDs grown on silicon were found to emit at 1550 nm (telecoms C-band) but at a reduced intensity compared to the GaAs grown sample, showing that dislocations were still present but not in sufficient quantities to inhibit emission. To observe individual exciton lines micropillars were etched into the samples to reduce the excitation area, allowing individual lines to be observed amongst the high density of emitters. It was found that the whole ensemble blueshifts with increased excitation power, but individual QD peaks show very little variation, showing a red shift of <2 nm. This shows that similar to the QRs band bending is not a significant cause of the blueshift, and it more likely arises from an increase in the intensity of higher energy states or the creation of new states at higher excitation power.

The individual QD peaks were found to be very broad for InAs QDs which was surmised to arise from high charge fluctuations around the quantum dot. By comparing apertures to pillars it was found that the edge states of the micropillar were not contributing significantly to the broadening. These individual lines are significant as they show that III-V type II QD structures can be integrated with Si, albeit with some linewidth broadening. It is believed that this is the first reported observation of silicon based single QD emission at 1500 nm, although without doing autocorrelation measurements it's impossible to assess its usefulness as a single photon source.

These Si grown samples could possibly be improved further, by annealing during growth, which has been shown to significantly improve the effectiveness of DFLs¹⁶. The sample showed significant fluctuations of the capping layer height, thickness and composition, so it would be interesting to try and grow a more uniform capping layer to see what effect these variations had on the QD peaks emission. It is possible a more uniform layer may reduce both the background and the QD linewidth. Additionally, a change in the growth of the QD layer to create a lower density and more uniform QD size may help to reduce the amount of emission observed.

To improve this work further performing a μ PL map of the Si based sample's surface before etching pillars would allow regions of poor emission (due to defects) to be isolated. This would allow micropillars to be sited in more optimal locations where the presence of defects are reduced allowing much a better recombination rate making the individual QDs on Si to be more easily observed. Overall this work shows a promising direction towards integrating telecoms wavelength emitting QDs with silicon.

5.6 References

- 1 Paschotta, D. R. RP Photonics. optical fiber communications, data transmission, capacity, telecom windows, C band, L band. <https://www.rp-photonics.com/optical_fiber_communications.html> (2017).
- 2 Mears, R. J., Reekie, L., Jauncey, I. M. & Payne, D. N. Low-noise erbium-doped fibre amplifier operating at 1.54 μm . *Electron. Lett.* **23**, 1026-1028, (1987).
- 3 Gasca, L. From O to L: The Future of Optical-Wavelength Bands. *Broadband Properties*, 83 - 85 (2008). <http://www.bbcmag.com/2008issues/june08/BBP_June08_OtoL.pdf>.
- 4 Marzin, J. Y., Gérard, J. M., Izraël, A., Barrier, D. & Bastard, G. Photoluminescence of Single InAs Quantum Dots Obtained by Self-Organized Growth on GaAs. *Physical Review Letters* **73**, 716-719, (1994).
- 5 Valéry, Z., Thomas, A. & Oliver, B. Quantum optics with single quantum dot devices. *New Journal of Physics* **6**, 96, (2004).
- 6 Unitt, D. *Enhanced single photon emission from a quantum dot in a semiconductor microcavity*, Cambridge, (2005).
- 7 Ulloa, J. M. *et al.* High efficient luminescence in type-II GaAsSb-capped InAs quantum dots upon annealing. *Applied Physics Letters* **101**, 253112, (2012).
- 8 Ripalda, J. M. *et al.* Room temperature emission at 1.6 μm from InGaAs quantum dots capped with GaAsSb. *Applied Physics Letters* **87**, 202108, (2005).
- 9 Liu, H. Y. *et al.* Long-wavelength light emission and lasing from InAs/GaAs quantum dots covered by a GaAsSb strain-reducing layer. *Applied Physics Letters* **86**, 143108, (2005).
- 10 Llorens, J. M. *et al.* Type II InAs/GaAsSb quantum dots: Highly tunable exciton geometry and topology. *Applied Physics Letters* **107**, 183101, (2015).
- 11 Haxha, V. *et al.* Role of segregation in InAs/GaAs quantum dot structures capped with a GaAsSb strain-reduction layer. *Physical Review B* **80**, 165334, (2009).
- 12 Shacham, A., Bergman, K. & Carloni, L. P. Photonic Networks-on-Chip for Future Generations of Chip Multiprocessors. *IEEE Transactions on Computers* **57**, 1246-1260, (2008).
- 13 Tang, M. *et al.* Optimizations of Defect Filter Layers for 1.3- μm InAs/GaAs Quantum-Dot Lasers Monolithically Grown on Si Substrates. *IEEE Journal of Selected Topics in Quantum Electronics* **22**, 50-56, (2016).
- 14 Group, K. Lattice Mismatch. <http://amps.che.wisc.edu/research_latticemismatch.php> (2017).
- 15 Masahiro, A., Yoshihiro, K. & Katsuzo, K. Growth of Single Domain GaAs Layer on (100)-Oriented Si Substrate by MOCVD. *Jpn. J. Appl. Phys.* **23**, L843, (1984).
- 16 Orchard, J. R. *et al.* In situ annealing enhancement of the optical properties and laser device performance of InAs quantum dots grown on Si substrates. *Optics Express* **24**, 6196-6202, (2016).

- 17 Yang, J., Bhattacharya, P. & Mi, Z. High-Performance In_{0.5}Ga_{0.5}As/GaAs Quantum-Dot Lasers on Silicon With Multiple-Layer Quantum-Dot Dislocation Filters. *IEEE Trans. Electron Devices* **54**, 2849-2855, (2007).
- 18 Orchard, J. R. *et al.* Silicon-based Single Quantum Dot Emission in the Telecoms C-band. *ACS Photonics*, (2017).
- 19 Liu, W.-S. & Chang, C.-M. Capping InAs quantum dots with an InGaAsSb strain-reducing layer to improve optical properties and dot-size uniformity. *Thin Solid Films* **570**, 490-495, (2014).
- 20 Saito, H., Nishi, K. & Sugou, S. Shape transition of InAs quantum dots by growth at high temperature. *Applied Physics Letters* **74**, 1224-1226, (1999).
- 21 Harbord, E., Spencer, P., Clarke, E. & Murray, R. The influence of size distribution on the luminescence decay from excited states of InAs/GaAs self-assembled quantum dots. *J. Appl. Phys.* **105**, 033507, (2009).
- 22 Trevisi, G. *et al.* The effect of high-In content capping layers on low-density bimodal-sized InAs quantum dots. *J. Appl. Phys.* **113**, 194306, (2013).
- 23 Sharma, N. & Reuter, D. A modified gradient approach for the growth of low-density InAs quantum dot molecules by molecular beam epitaxy. *J. Cryst. Growth*, (2016).
- 24 Jie, S., Peng, J. & Zhan-Guo, W. Extremely low density InAs quantum dots realized in situ on (100) GaAs. *Nanotechnology* **15**, 1763, (2004).
- 25 He, Y.-M. *et al.* On-demand semiconductor single-photon source with near-unity indistinguishability. *Nat Nano* **8**, 213-217, (2013).
- 26 Reitzenstein, S. & Forchel, A. Quantum dot micropillars. *Journal of Physics D: Applied Physics* **43**, 033001, (2010).
- 27 Ulloa, J. M. *et al.* Suppression of InAs/GaAs quantum dot decomposition by the incorporation of a GaAsSb capping layer. *Applied Physics Letters* **90**, 213105, (2007).
- 28 Lee, S. M. & Bajaj, K. K. A quantum statistical theory of linewidths of radiative transitions due to compositional disordering in semiconductor alloys. *J. Appl. Phys.* **73**, 1788-1796, (1993).
- 29 Seravalli, L. *et al.* Single quantum dot emission at telecom wavelengths from metamorphic InAs/InGaAs nanostructures grown on GaAs substrates. *Applied Physics Letters* **98**, 173112, (2011).
- 30 Seravalli, L., Frigeri, P., Nasi, L., Trevisi, G. & Bocchi, C. Metamorphic quantum dots: Quite different nanostructures. *J. Appl. Phys.* **108**, 064324, (2010).
- 31 Hermannstädter, C., Huh, J. H., Jahan, N. A., Sasakura, H. & Suemune, I. in *IPRM 2011 - 23rd International Conference on Indium Phosphide and Related Materials*. 1-4.

Chapter 6

Increasing light extraction using UV curable SILs

This chapter describes how a liquid based solid immersion lens (SIL) made from UV curable epoxy can be used to enhance the light output of a 2D material. The epoxy SIL described fully encapsulates the monolayer helping to prevent physical damage and degradation in air. Micro-photoluminescence results show a large intensity increase from a monolayer of tungsten diselenide (WSe₂) combined with an increase in imaging resolution.

6.1 Introduction

Transition metal dichalcogenides (TMDs) as previously discussed are 2D materials that have a direct bandgap in the visible to NIR range. They are ideal for optoelectronic applications such as LEDs, lasers and photovoltaics¹ due to their unique ability to be stacked into heterostructures with graphene and boron nitride, to enable electrical excitation. These materials have advantages over existing III-V based devices due to their low cost and easy integration with silicon, which as discussed in the previous chapter are major drawbacks to III-V materials. Additionally, TMDs have a low thickness which makes complex multilayer structures (also known as van der Waal heterostructures) a lot more compact and therefore easy to integrate onto flexible substrates². As well as these many advantages for classical light sources TMDs show a good potential for quantum light, with defects in 2D materials capable of confining excitons to form quantum dot like emission, that can be electrically excited to make a on demand single photon source³.

However, TMDs are not without their drawbacks; one of the most significant challenges lies in maximising the light output of a monolayer flake. TMDs typically have a low light output compared to III-V based devices due to poor quantum yields (QY) which range from 0.01 – 6%⁴ compared to GaAs based QD's which can be very close to 100%^{5,6}. This can cause significant problems when developing a single photon source where any loss of photons can cause a significant reduction in performance⁷. Several recent studies have attempted to improve the materials photoluminescence (PL) using several different methods such as: chemical treatments using organic superacids⁴ and functionalisation using chemically active groups^{8,9}, plasmonic structures such as nano-spheres¹⁰ and gold coated trenches¹¹, microcavities¹² and photonic crystals^{13,14}. The gains from these methods

predominantly come from either improving the internal quantum efficiency, or increasing the pump adsorption coupled with a decrease in the radiative lifetime. Whilst these methods are effective at increasing light output none of these fully address the problem of extraction efficiency. A solution that can provide increased light coupling into the far field, whilst incorporating a light enhancing structure (e.g. a photonic crystal) would be highly desirable for the future of TMD based devices. For the rest of this chapter we address this issue by taking the aforementioned epoxy SILs, and employ them for the first time directly onto TMDs¹⁵. This should not only enhance the light output coupling of the TMD, but also will help to protect the TMD flake from degradation in air due to oxidation, which can significantly damage the optical and electronic properties of the TMD¹⁶.

6.2 Fabricating SILs onto different surfaces

6.2.1 Embedded GaSb/GaAs Quantum rings

To test the viability of epoxy SILs they were initially investigated by fabricating them on a sample of embedded GaSb quantum rings using the method outlined in section 3.2.2. The GaSb QR samples were initially chosen as reference sample that could easily be compared with PL data taken in Chapter 4. Additionally, the GaSb quantum ring samples have a uniform, flat hydrophobic surface (GaAs) which enables the formation of high contact angled epoxy droplets with similar contact angles to the previously studied glass SILs. Multiple epoxy SILs were created with varying contact angles onto the sample, and the μ PL analysed, the results of one of these SILs and its glass counterpart are presented in Figure 6.1a, and a side view of this SIL is shown in Figure 6.2a. From this data, epoxy SILs appear to be as effective as the glass SILs, with both showing a very similar enhancement of their QD peak. It should be noted that the glass SIL has been stuck in place using the same epoxy that was used to make the SIL, (as the cryostat it was being measured in has a vertical orientation). Therefore, since its interface with GaAs has the same refractive index as the epoxy, it is not increasing the light output as effectively as it has the potential to do. Theoretically it can be calculated for a perfect s-SIL (using equation 2.8) that the enhancements should be 12x, 6.2x for glass and epoxy respectively. This demonstrates that an epoxy SIL is just as useful as a glass SIL in applications where the SIL needs to be bonded to the surface.

The PL of the QD peak of the epoxy SIL in Figure 6.1a is lower than its theoretical value, this was most likely due to the SIL being distorted when fabricated. This distortion greatly reduces the SILs imaging and collection performance due to both the laser spot and the PL becoming de-focussed. To get a better idea of the SILs true potential an epoxy SIL with a close to perfect geometry was formed. Figure 6.1b shows the PL from this SIL, from different positions in the centre and compares them to a point off the SIL on the substrate (black). The integrated intensity of the PL increases by 5.90x which is very close to the theoretical value stated earlier. The addition of the SIL has also increased

the imaging resolution by reducing the laser spot size, this means that we can see more detail in the quantum dot peak than we can on the substrate, due to less structures being excited.

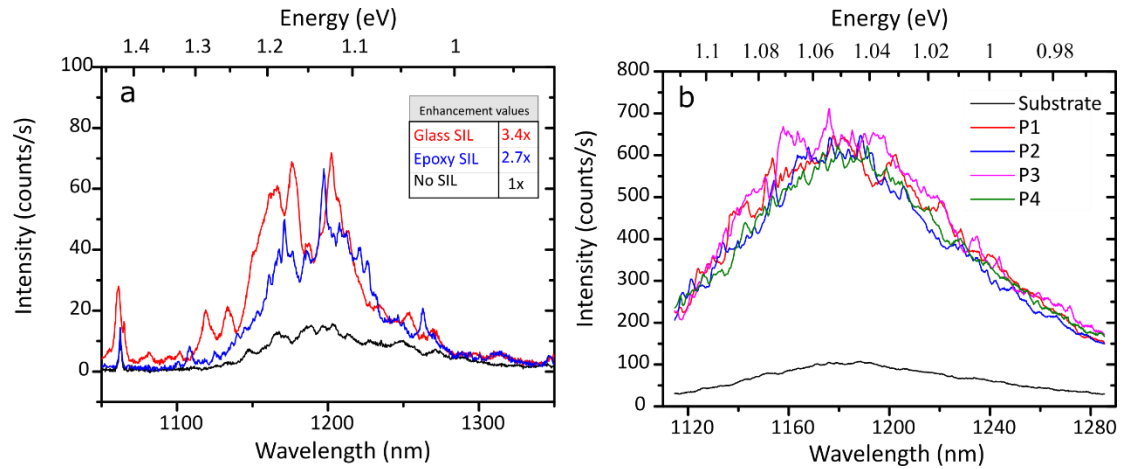


Figure 6.1 – (a) Compares the PL spectra of a SIL formed from glass (red) and epoxy (blue) to the substrate, (b) shows 4 different positions (P) in the centre of the SIL (coloured), compared to the intensity on the substrate (black).

6.2.2 Delicate surfaces

The work on GaSb QDs showed epoxy SILs have great potential on embedded systems, however one of the main advantages of epoxy SILs have over glass SILs is that they have the potential to be placed on sensitive surfaces. To test this epoxy SILs were deposited on a range of different samples which were too sensitive for glass SIL's, microscope images of these samples are shown in Figure 6.2b-d. The MoS₂ sample shown in Figure 6.2b was fabricated in Lancaster using mechanical exfoliation and shows that the application of the epoxy doesn't remove the flakes. The image in Figure 6.2c shows a SIL on a sample containing site controlled quantum dots made by the Tyndall National Institute in Cork¹⁸, and have been back etched, to reveal the pyramid tips containing the QDs. Figure 6.2d shows a gold grid containing plasmonic nano-rings, fabricated by the University of Southampton¹⁹. It can be seen from Figure 6.2 that the SILs show excellent optical quality, despite being on some very rough and non-uniform surfaces with the samples visually appearing undamaged from the encapsulation process. Additionally, various sizes of SIL are possible with Figure 6.2a having a radius of 720 μm and Figure 6.2b 325 μm . SIL's less than 250 μm in radius are very challenging to fabricate with the current setup for two reasons, firstly their small optical window makes positioning of the SIL difficult, secondly a SILs quality is highly dependent on their shape, and they become increasingly more effected by slight variations as they reduce in size.

Figure 6.2c shows a small amount of distortion due to the SIL not being perfectly circular, this arises from large features on the surface effecting how the epoxy spreads as it wets to the surface, creating non-symmetrical lenses. Although the lens still enhances and roughly works, the slight reduction in optical quality will reduce its effectiveness at enhancing PL due to it poorly focusing the PL, and

distorting the laser spot. One solution that was found to be effective was to first spin the same epoxy used for the SILs onto the surface at a sufficient thickness to fill the surface so it becomes flat, making a smooth surface when cured. The advantage of this is that once cured, the spin film has the same refractive index as the SIL itself; therefore, the interface should be invisible to the light and appear as part of the SIL. When making SILs in this way care must be taken to know the thickness of the spin epoxy before applying the SIL, as its thickness will slightly change the effective height of the SIL, and consequently the optical properties of the SIL. The minimum uniform layer thickness that can be achieved with the epoxy used to create the SILs (NOA 81) was found to be approximately $1.5 \mu\text{m}$

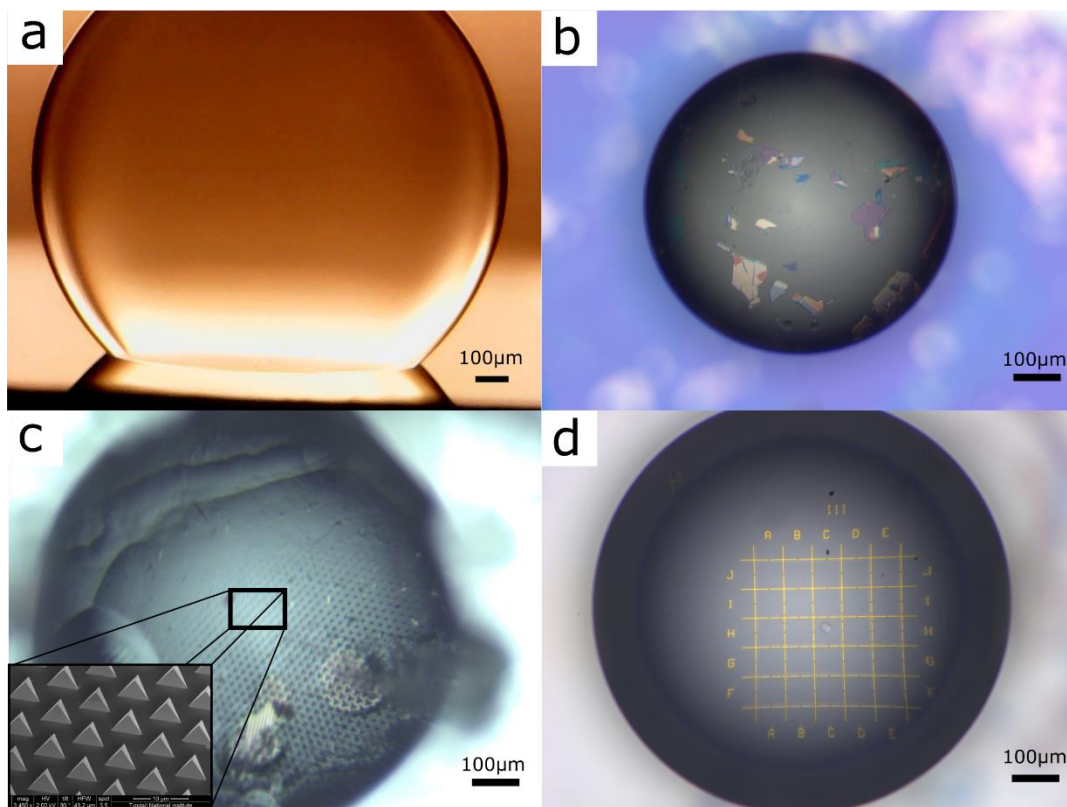


Figure 6.2 - Epoxy SILs mounted onto different surfaces, (a) Side view of a SIL mounted on GaAs whilst inside the glycerol bath, (b) A SIL on-top of mechanically exfoliated MoS_2 flakes, (c) site controlled pyramid QDs, (d) Gold grid containing plasmonic nano-rings

Figure 6.3 shows a wavelength PL map of a single pyramid isolated inside a SIL, the reduction in the laser spot and increase in magnification allows single pyramid to be mapped. The pyramid is emitting as expected and the quantum dot peak is observed roughly in the centre of the triangular structure with some shorter wavelengths corresponding to its GaAs base appearing around it. This shows that these structures PL has been unaffected by the application of the SIL. Unfortunately, the high distortion of the SIL shown above made it unsuitable for enhancing emission. This has arisen from the non-uniform back etch that has been performed on it making regions of the surface several microns higher than others. However, if enhancement of these structure was going to be

reattempted, a good first approach would be to try and fill the surface with the epoxy until a flat surface could be achieved. Then a SIL with a slightly reduced height could be dispensed onto a completely flat surface avoiding any distortion.

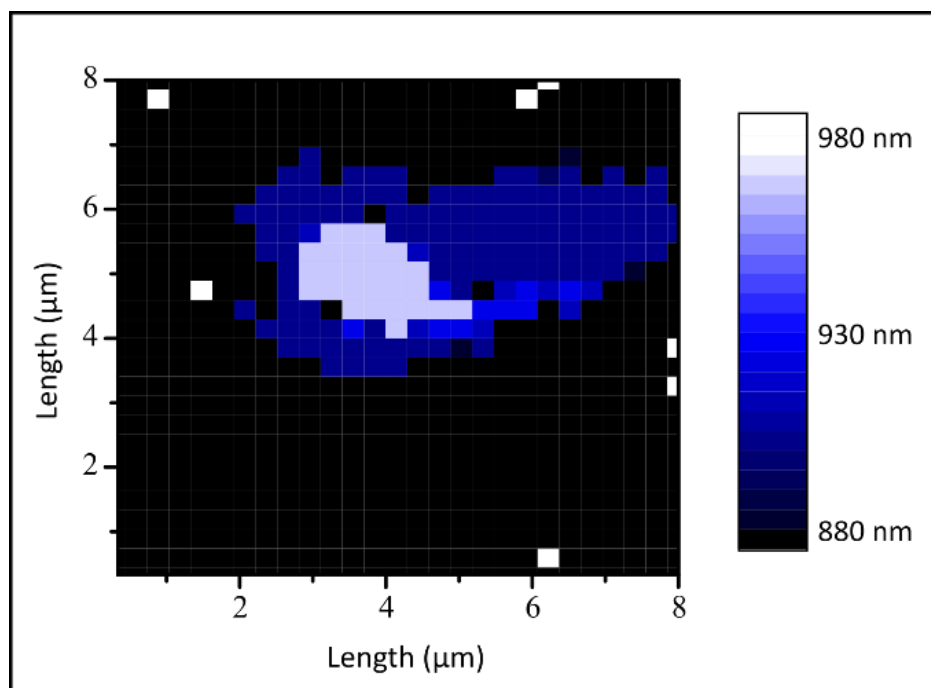


Figure 6.3 - Peak wavelength emission map of a site controlled quantum dot (shown in **Figure 6.2c**) (The white individual points arise from the fitting function used trying to incorrectly fit background noise and should be ignored).

6.3 Fabricating SILs onto 2D materials

Following on from the promising results in the previous section, the deposition of SILs onto mechanically exfoliated 2D materials was attempted. However, fabricating SILs on these samples presented new challenges, the first being that in this system the exact positioning of the SIL was essential. Most mechanically exfoliated 2D materials form monolayer flakes between 10 - 50 μm , with larger flakes being a lot rarer. This means that the centre of the SIL needs to be perfectly positioned to ensure the flake is in the optical window, as unlike previous samples only the monolayer flake emits light. The small size and high translucency of a monolayer makes it almost impossible to spot without a microscope, presenting extra challenges when fabricating a SIL. To overcome these challenges a whole new SIL mounting system was designed, and can be seen in Figure 6.4. The most important changes involved making the frame sturdier to prevent any undesired movement during SIL deposition, and adding a vertical magnifying endoscope to enable the flakes on the surface of the sample to be viewed, and the needle moved accordingly. The syringe barrel itself was angled at 45° and the needle manually bent at the same angle to allow it to deposit

vertically. It is very important that the needle is perfectly vertical to prevent the epoxy from syphoning up its sides, which prevents a nice droplet being formed, ruining the shape and symmetry of the desired SIL. The sample was illuminated from the side using a strong white light source, and the needle positioned over the monolayer, using the endoscope to locate the precise area.

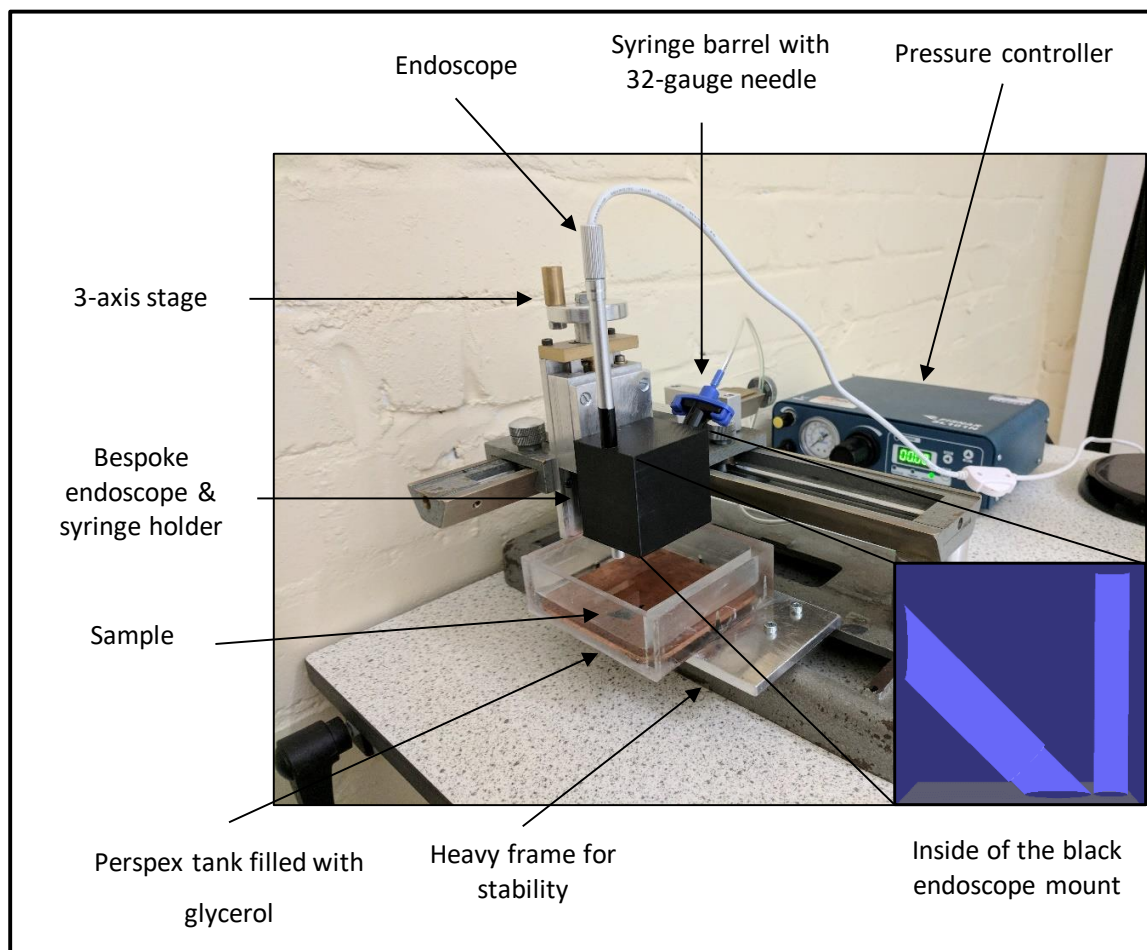


Figure 6.4 - Picture showing the experimental setup used to mount epoxy SILs onto 2D materials. Inset: Cross-section of the 3D printed mount holding both the endoscope (vertical) and syringe barrel (diagonal).

An additional challenge that mechanically exfoliated 2D materials presented was having a very non-uniform surface, due to thick flakes of material being deposited with the monolayer. To prevent this from effecting the base of the SIL, approximately 200 nm of NOA 81 (the same epoxy used to manufacture the SILs) was spun onto the surface to encapsulate all the flakes and make a uniform surface.

6.3.1 Enhancement of a Tungsten Diselenide (WSe₂) monolayer

The 2D material explored for use with SILs was Tungsten diselenide, which was chosen for several reasons. Firstly because it is one of the most studied 2D materials along with MoS₂, and secondly due to literature showing that it's capable of forming atomic level imperfections that act as single photon emitters^{20,21}, which could be integrated into an electrical device³. A SIL positioned on top of such a device would greatly increase the number of photons coupling out of the device, making it much more suitable for quantum security applications due to an increased bit rate²².

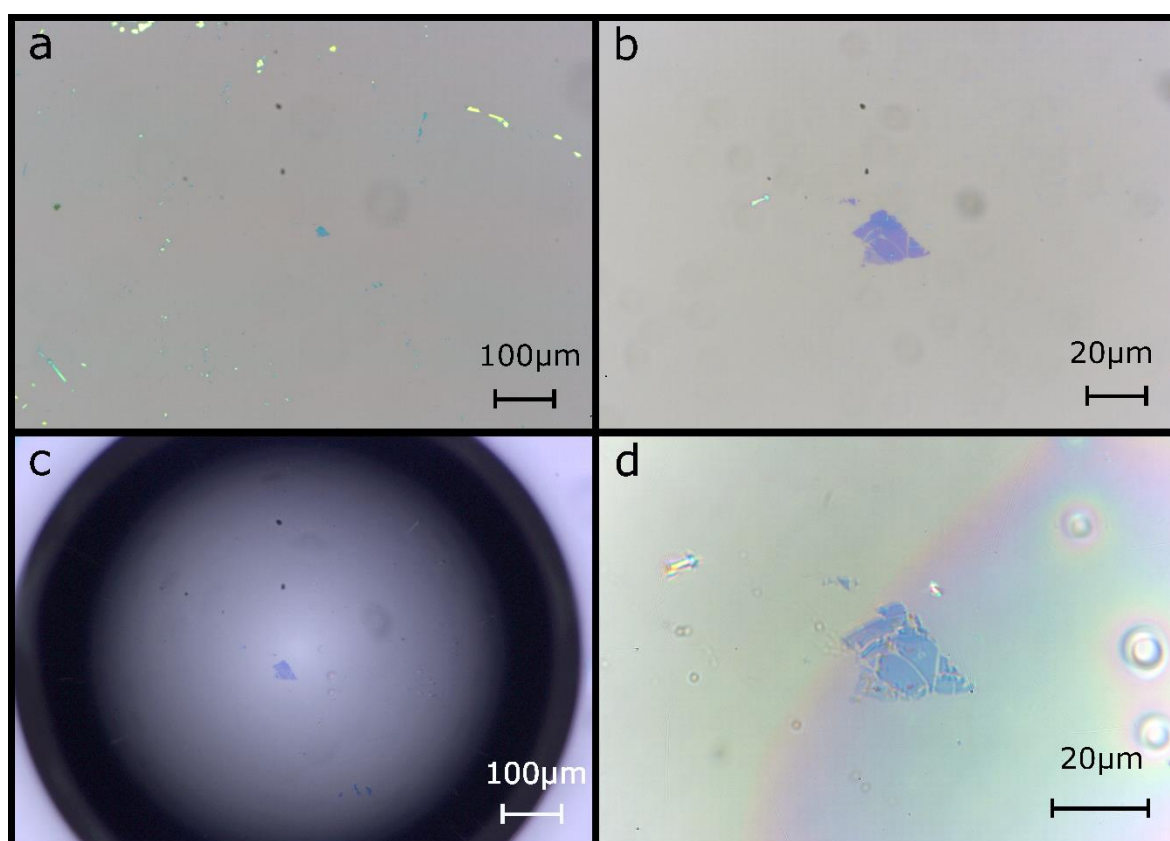


Figure 6.5 - Optical microscope image showing an isolated mono/bilayer of WSe₂, before (a,b) and after (c,d) mounting a SIL; the scale bar in (d) had been adjusted to account for the SILs magnification.

Figure 6.5 shows microscope images of a flake of WSe₂ approximately 20 µm², which contains regions of both monolayer and bilayer, both before and after the application of a SIL. The mounted epoxy SIL had a radius of 550 ± 5 µm, and a height from apex to base of 700 ± 50 µm creating a geometry somewhere between a h-SIL and a s-SIL (77% the height of a perfect s-SIL). This height is the maximum that could be achieved when applying a droplet on-top of the cured epoxy, and is the closest to an s-SIL that can be achieved without any additional modification of the sample surface. From optical microscope measurements of the flake, it was found that the SIL provided a magnification increase of 1.80. This magnification increase greatly helps in resolving fine defects and

cracks in the flakes which were previously difficult to identify, this can be seen between Figure 6.5b and d where cracks become easily observable in d which are difficult/cannot be seen in b. It should be noted here that there is an argument for the process of fabricating the SIL slightly widening these cracks. However, this was not investigated further as it did not appear to affect the optical properties of the flake. In Figure 6.5d optical artefacts are observed that are not seen in c, these are mainly down to using a narrower aperture in the microscope to take the image. Also observed is an iridescent sheen that appeared very abruptly, and was not present upon fabrication, this is possibly from a thin film of material contaminating the apex of the SIL sometime after being formed e.g. oil. It can also be observed that a few bubbles of either air or glycerol have become encapsulated, but providing the bubbles are not directly over the monolayer, these defects will have no effect on the light collection efficiency.

6.3.2 Resolution Enhancement and stability

To assess the performance of the SIL photoluminescence (PL) intensity maps of the WSe₂ flake shown in Figure 6.5 were performed both before and after the application of the SIL. These maps were performed by integrating the individual spectra between 700 – 900 nm, and assigning the integrated area as the intensity for that point. The graph is then interpolated to give a better comparison with the optical microscope images, the results of this can be shown in Figure 6.6. The increase in magnification previously discussed is easily observed between a-b of the PL maps in Figure 6.6, and the distance scales have been adjusted accordingly, with the magnified area identified by the orange box. The overall improvement in magnification is 1.80x from an epoxy with refractive index of 1.56, which is somewhere between that of an h-SIL (linear dependence with n giving 1.56x) and a s-SIL (quadratic dependence with n giving 2.43x)²³. This result shows that SILs in between the h and s-SIL geometries (shown in Figure 2.7), can give optical properties that are a combination of the two, with the studied SIL showing a greater magnification than an h-SIL without introducing strong chromatic aberrations. This suggests that gradually increasing the contact angle to the substrate from 90° will change the magnifications dependence on refractive index from a reciprocal to an inverse square relationship. This means that epoxy SILs have the potential to be formed into geometries that can provide optimised trade-offs between magnification and white light image quality.

The resolution increase observed in a SIL derives from a reduction of the lasers spot size as it travels from air to the SIL. Theoretically the increase in resolution from a h-SIL in μ PL arises from a decrease in laser spot diameter, which is proportional to $1/n$ (where n is the refractive index of the SIL)²³. The laser acting as a plane wave will approximately project an airy pattern with a half-width at half-maximum (HWHM) of:

$$\text{HWHM} = \frac{0.26\lambda}{n\text{NA}_{\text{obj}}} \quad (6.1)$$

where n = refractive index of the volume above the TMDC, NA_{obj} = numerical aperture of the μ PL system and λ = excitation wavelength²⁴. Calculating (6.1) with the experimental parameters here gives an expected resolution increase of 1.6 times.

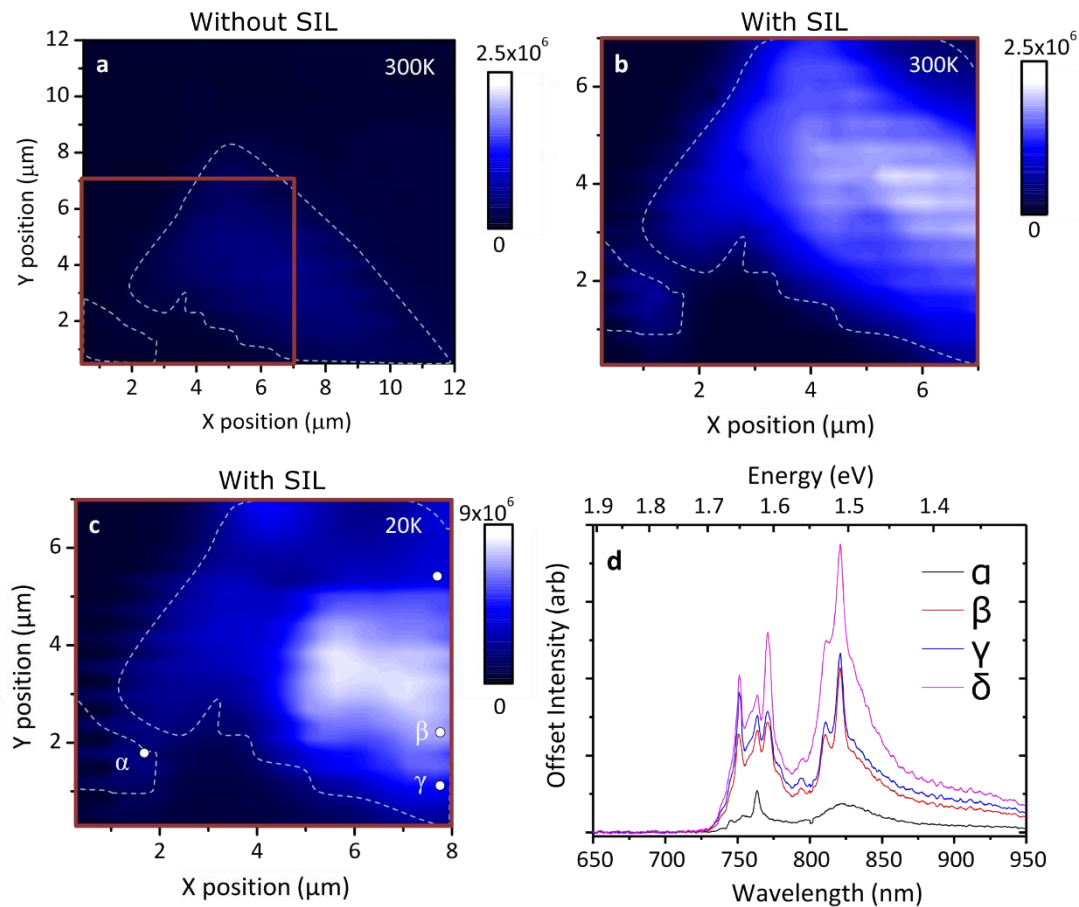


Figure 6.6 - Interpolated photoluminescence maps of a WSe_2 flake (outlined) taken both with and without a SIL and at low (20K) and high (300K) temperatures, as labelled; panels (a)-(c) show PL maps where the colour scale refers to the integrated intensity as a function of position; (d) shows example spectra from positions labelled in (c). The orange box in (a) highlights the area seen in (b) and (c).

An important property of a SIL for photoluminescence work is to be very stable at low temperatures. This is especially important when developing single photon sources, due to phonons heavily influencing the recombination rate and the line width of the emission. Figure 6.6c shows a map taken at cryogenic temperatures (20 K); the temperature change has had no detrimental effect on the emission of the monolayer. This result shows epoxy SILs are resistant to temperature changes, and can thus be used for photoluminescence studies at cryogenic temperatures. Some example spectra from Figure 6.6c are shown in Figure 6.6d, these spectra occur all over the sample but seem more common around the monolayer-bilayer boundary which could explain the two separate peaks. Sharp exciton-like lines can be observed in each of these spectra, this is unusual as these sharp peaks do not appear anywhere else on this flake, nor do they appear at room

temperature. Since these peaks all occur at the same wavelength, it is unlikely that they are due to random QD like impurities that form within the monolayer, but could be due defects/impurities that are more likely to occur at the monolayer-bilayer boundary.

Figure 6.7a/b show wavelength maps that highlight the value of the peak wavelength at 300K and 20K respectively. It can be observed by comparing (a-b) that there is a shift in wavelength in some regions of the monolayer upon cooling to 20K. The 760 nm monolayer peak observed uniformly at room temperature, red-shifts to ~ 820 nm everywhere except the region 2. This shift (approximately 80 nm) is a lot higher than expected from previously published results at low temperature, which show up to a 20 nm shift, between 300K and 20K²⁵. Additionally, the regions that shift to 820 nm do not have the same spectral signature; this can be seen in Figure 6.7c, where different regions in (b) are compared against each other. The edges of the flake (region 1) show a much broader emission than region 3 which is in a more central location. The monolayer peak at 780 nm can still be detected in both regions 1 and 3, but is lower in intensity relative to the 820 nm peaks. Huang, et al. [26], attribute long wavelength exciton-like peaks to “defect related localised state transitions.” It could be that the epoxy or the glycerol bath is introducing a residual impurity across the flake, which allows a localized state to form within the monolayers bandgap. If excitons were to fall into this state they would emit at a longer wavelength, which might explain the shift in the peaks observed at low temperatures. The pattern observed may therefore be related to how the epoxy/glycerol impurities has interacted with the monolayer, which might explain why edges show differences in emission, as the impurities may find it easier to intercalate into these areas. To further this idea a power and temperature dependence would need to be performed on these peaks, both before and after the application of a SIL. Tracking the peaks in this way would give a greater information into the origin of these long wavelength emissions.

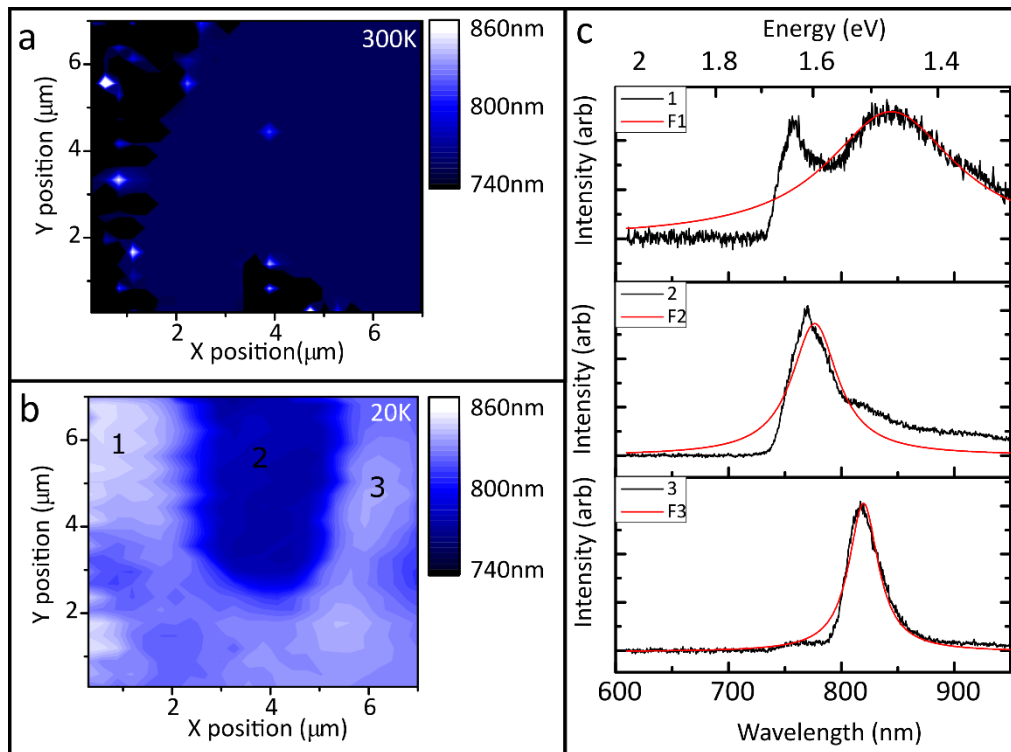


Figure 6.7 – (a-b): Peak wavelength map of the WSe_2 flake shown in Figure 6.6 at 300K and 20K respectively (c): Individual spectra from positions (1-3) marked in (b) with Lorentzian fits (F1-F3) showing how the peak wavelength in (b) are obtained.

6.3.3 Photoluminescence enhancement

One of the most important property of any SIL placed on a 2D material is its ability to increase the amount of light coupled into and out of the monolayer flake. When comparing Figure 6.6a to Figure 6.6b, there is a significant and uniform increase in the intensity of the flake (both maps were taken for the same laser excitation power).

Figure 6.8a, shows the measured PL spectra for an arbitrary point on the monolayer from figure 6.6a/b at $10\mu W$ of excitation power. Comparing the integrated intensity of the flake both before and after the application of a SIL a large enhancement of 300% is observed.

As described in earlier chapters, the theoretical enhancement of the SIL arises from increasing the solid angle of the emission that can be detected, arising from the SIL refracting light at the SIL-air boundary. A SIL with the dimensions stated above should increase the solid angle of light emitted vertically by 1.33x, however the SiO_2 layer will also reflect light back, creating a virtual source which will in turn be enhanced by the SIL. Calculating these values, we find that the solid angle of the reflected light would be increased by 3.15x, which when scaled to take account of the percentage of light that would be reflected and added to the vertical emission we get a total enhancement of 2.0x (100%) enhancement. This theoretical value is only half the power of the experimental results, and could be due to the value only considering the emission from the monolayer and not the effect

on the SIL on the excitation source. The laser used to excite the PL must pass through the SIL first, which as mentioned previously reduces the radius of excitation, subsequently increasing the power density. This change in power density can be approximated based on the change in spot size, and was calculated to be 2.4x higher with a SIL. This increase in relative power could explain why the observed increase is so much higher than expected. This could in future be looked at experimentally by forming a SIL over an electrically excited monolayer flake, since the excitation power would be completely unaffected by the SIL it should give a value much closer to the calculated value.

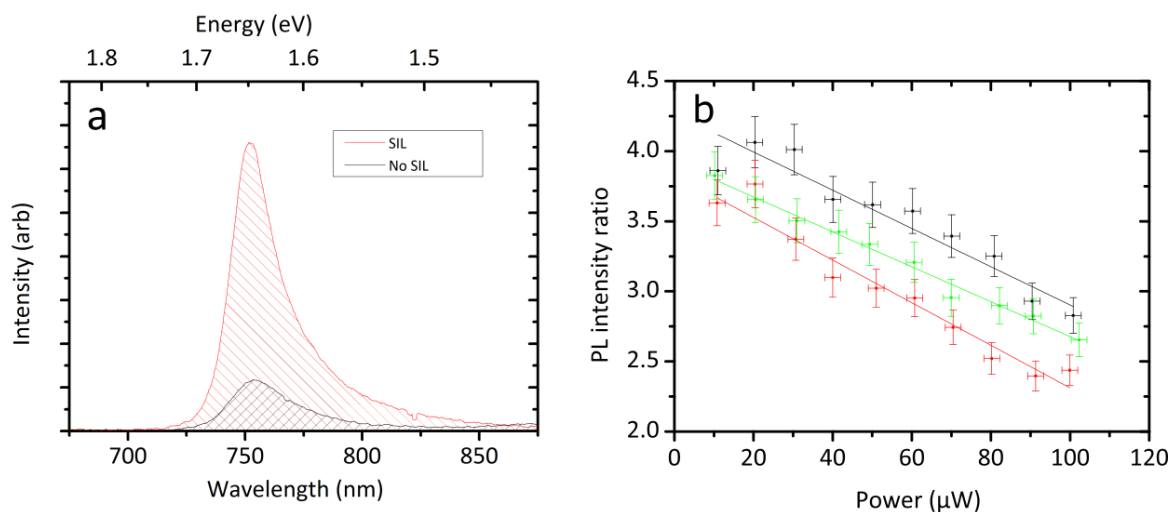


Figure 6.8 - Graphs showing example PL spectra for monolayer WSe_2 with and without a SIL for the same excitation power (a), and the power dependence of the intensity ratio of SIL to no SIL for three different positions on the monolayer (b).

The relative enhancement of the SIL varied with excitation power, this is shown in Figure 6.8b where the ratio between SIL to no SIL is plotted vs. excitation power for different monolayer positions. The reduction in the intensity with power might be caused due to the increased power from the smaller spot size, which can reduce the relative PL intensity through charge screening effects, leading to an overall reduction of relative intensity with power. A decreased spot size could also cause an increase in localised heating of both the epoxy and the flake, which may affect both the emission of the monolayer and the optical properties of the SIL due to thermal effects. One explanation for these effects that can be discounted is doping and strain from the epoxy, as similar WSe_2 monolayers show no enhancement in their PL when they are coated with a film of cured epoxy, rather than a SIL (Figure 6.9).

6.3.4 Issues with Molybdenum Disulphide (MoS_2)

Another heavily researched TMD material is MoS_2 , primarily due to its abundance thanks to it being commonly used as an industrial lubricant²⁷. To study the SILs applicability to other TMDs a SIL was mounted onto a MoS_2 flake using the same methods as previously used for WSe_2 and can be seen in Figure 6.2a. Upon performing photoluminescence measurements, very little signal was observed and

after repeating with a different sample and SIL it became clear that this was caused by the application of the SIL. To investigate this further a 1.5 μm thick layer of epoxy was spin-coated onto another monolayer of MoS_2 and PL taken before and after the application and can be seen in Figure 6.9a. Simply spinning and curing epoxy onto the surface of MoS_2 causes its PL to become heavily suppressed, with an order of magnitude reduction of the peak coupled with a red shift of 8nm. If we compare this to WSe_2 (Figure 6.9b) with the same thickness of film, there is no change in the peak intensity when applying the epoxy, however there was observed a blue shift and a slight reduction in the peak width. Blue shift of the WSe_2 peak is indicative of possible n-type doping²⁸, which increases the number of additional electrons, and as consequence enhancing the charged excitons (trions) and reducing the neutral exciton peak²⁹. The effect of doping may explain the observed changes in monolayer intensities. Since WSe_2 is p-type with high hole mobilities³⁰ and shows ambipolar behaviour³¹. A slight increase in negative charge provided by dopants in the epoxy, is unlikely to have a large effect on the PL, due to it being cancelled by the positively charged environment. Mechanically exfoliated MoS_2 is known to be naturally n-type arising from point defects in its crystal structure²⁹, this means that further increasing the negative charge will cause quenching of the PL, as observed by Mouri, et al. [32] who show not only quenching for MoS_2 but also a slight red shift similar to that observed in Figure 6.9.

If the epoxy is n-type doping it could be possible to treat the sample with a p-type dopant e.g. TCNQ³² or azobenzene molecules²⁹, before applying the epoxy to help neutralise any point charge defects in the sheet, and counteract the excess electrons from the epoxy. An alternative approach could be to functionalise the surface with covalent molecules^{8,9} which should help enhance the flake and may serve as a barrier to prevent the epoxy from introducing dopants into the flake.

Another explanation for the quenching of the MoS_2 PL could be due to compressive strain rising from the curing of the epoxy. It has been previously shown that compressive strain can alter the bandgap of MoS_2 from direct to indirect³³, this would be expected to quench the PL emission. The compressive strain values needed to induce a shift from direct to indirect bandgaps for MoS_2 and WSe_2 are 0.5% and 1.5% respectively³⁴. Since the threshold for WSe_2 is higher than MoS_2 , the epoxy may have induced enough compressive strain to change the bandgap in MoS_2 , but not in WSe_2 .

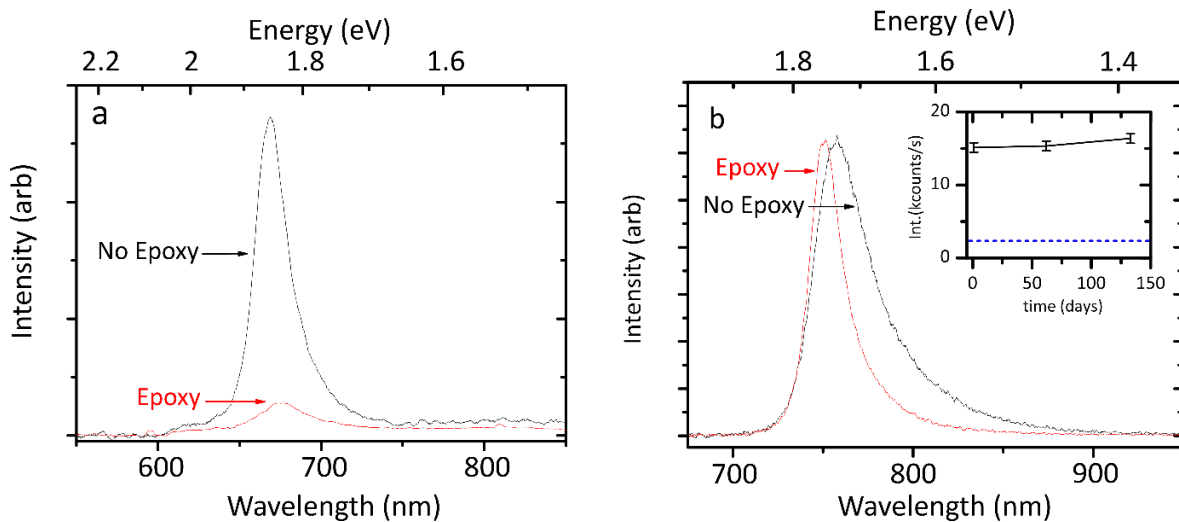


Figure 6.9 – PL spectra of (a) MoS_2 ; and (b) WSe_2 before and after the application of a thin film of cured epoxy; **Inset:** graph demonstrating the lack of degradation from aging due to the epoxy SIL, the dashed blue line shows the peak intensity before application of the SIL.

6.3.5 Increase in longevity

The epoxy used to encapsulate the flake has an additional advantage of sealing the TMD material from air, which could increase the longevity of the monolayer flake. Under ambient conditions it is well known that TMD monolayers degrade due to oxidation and introduction of organic contaminants¹⁶, which can make them tricky materials to work with due to time constraints. To test the stability of our monolayers under the epoxy SILs, the WSe_2 flake shown in Figure 6.5 was left in ambient conditions for a 6 month time period. The PL peak intensity over this time period is shown in Figure 6.9b (inset) where, within the uncertainty of the system the intensity remained constant; this combined with no visual change demonstrate that no significant degradation occurred.

6.4 Conclusions

In this chapter, we showed that UV-curable epoxy formed solid immersion lenses can be fabricated and mounted onto multiple semiconductor structures which are not suitable for more traditional glass SILs, improving their resolution and increasing their light output. It was demonstrated that these SILs can be applied to 2D materials fully encapsulating and protecting them from the environment, with a WSe_2 flake showing a 250-300% improvement in its photoluminescence, and magnifying the flake by 1.8x. The SILs show they are very temperature stable with thermal cycling to 20K not appearing to affect the SIL or the monolayer underneath it.

The mounting of the epoxy SILs had some effects on the PL emission of the TMD monolayer, blue-shifting the wavelength of the WSe_2 peak at room temperature, causing large positional dependence shifts at low temperature, and quenching the PL of MoS_2 . It is likely that all these effects are linked

and arise from impurities in either the epoxy or the glycerol, however the epoxy is much more likely due to it containing a mixture of unknown material. The UV epoxy we were using (Norland Optical Adhesive) has a composition that is a trade secret and it is not possible to find out exactly what chemicals it is made from, however comparing the effects of these impurities to literature it is likely that epoxy is donating electrons to the monolayer (n-doping). Further study of these samples is needed to confirm this as being the cause, and strain of the monolayer could still be a factor, however this doping can potentially be controlled to avoid it causing PL quenching.

Epoxy SILs have the potential to be an excellent cheap enabling technology for WSe₂ based optoelectronic devices such as LED's. The SILs in this study would likely increase light output of a LED by 100%, however by tuning the SIL to a perfect s-SIL there is the potential to theoretically create a 400% increase. The great advantage of this method of light extraction is that it will interact in an accumulative manner with any other emission increasing methods such as photonic crystal cavities, or plasmonic structures. A great example of the potential would be to take the single photon source made by Palacios-Berraquero, et al. [3], transfer the single photon source to a plasmonic array/photonic crystal cavity, then place a SIL over the top to create a bright single photon source based on silicon, in a relatively affordable packaging.

6.5 Further work

6.5.1 Increasing the emission of 2D materials

In this chapter, the problem of low light emission from TMD's was addressed by increasing the collection efficiency via the use of an epoxy based SIL. However, for a surface emitter a SIL does not aid in recovering light lost to the substrate, nor does it physically increase the amount of light emitted by the TMD's. Providing the emission is omnidirectional the SIL's will interact with the emitted light multiplicity, meaning that any method that increases the rate of emission will combine with the SIL to make a significant increase in light collected. This could be essential to the development of efficient 2D based emitting devices and single photon LED's.

There are multiple different methods that could be used to increase the light output of 2D materials ranging from simple solutions such as growing DBR mirror pairs below the monolayer, to more complex solutions such as using either nanocavities³⁵ or plasmonic trenches¹¹ to increase the absorption of the pump light that normally goes through the 2D material and gets lost to the silicon.

Plasmonic structures are especially interesting as they are capable of both enhancing the absorption of the pump laser and creating a Purcell enhancement by modifying the local electric field around the emitter. Recent reports have shown plasmonic nanogaps enhancing PL by up to 20,000 times that of an equivalent flake on a Si substrate¹¹. Combining a WSe₂ flake on a gold plasmonic grid with an epoxy SIL should dramatically increase light emission from suspended regions of the WSe₂ flake. This could be especially effective at enhancing defect states in WSe₂, by deliberately tuning the plasmonic gap to the wavelength of the defects states (typically 720-780 nm^{20,21}), the spontaneous emission can be enhanced. The extra light emission from this can then be enhanced further by placing an epoxy SIL over the top of the flake to improve the amount of light collected. These defect states have been shown to have good single photon emission with values of ^{3,20,21,36}. They can also be site controlled by locally modifying the strain of the sheet³⁶ making them a very attractive single photon source, with a great integration potential with silicon.

Preliminary work was performed to try and fabricate gold plasmonic nano-trenches that have a plasmonic-gap resonance tuned to somewhere between 720 and 780 nm. The overall goal of this work would be to place a WSe₂ flake on-top and see if the plasmonic trenches can enhance the PL of the defect states at cryogenic temperatures. Simulations on similar structures in literature, have shown that trench widths of 7-12 nm³⁷ and a pitch size of 200 nm¹¹ for a 100 nm thick film of gold should create a plasmonic mode in the defect wavelength range. These literature values were used as a rough guideline for some initial fabrication, and 150 nm of gold was evaporated onto a Si wafer with a 300 nm SiO₂ layer. Electron beam physical vapour deposition (EBPVD) was chosen over thermal evaporation due to it being performed under a higher vacuum which helps to reduce

impurities that can act as sources of non-radiative scattering of plasmon-polaritons. A thin 10 nm layer of Ti was evaporated onto the Si wafer before the gold to assist in adhesion to the SiO₂.

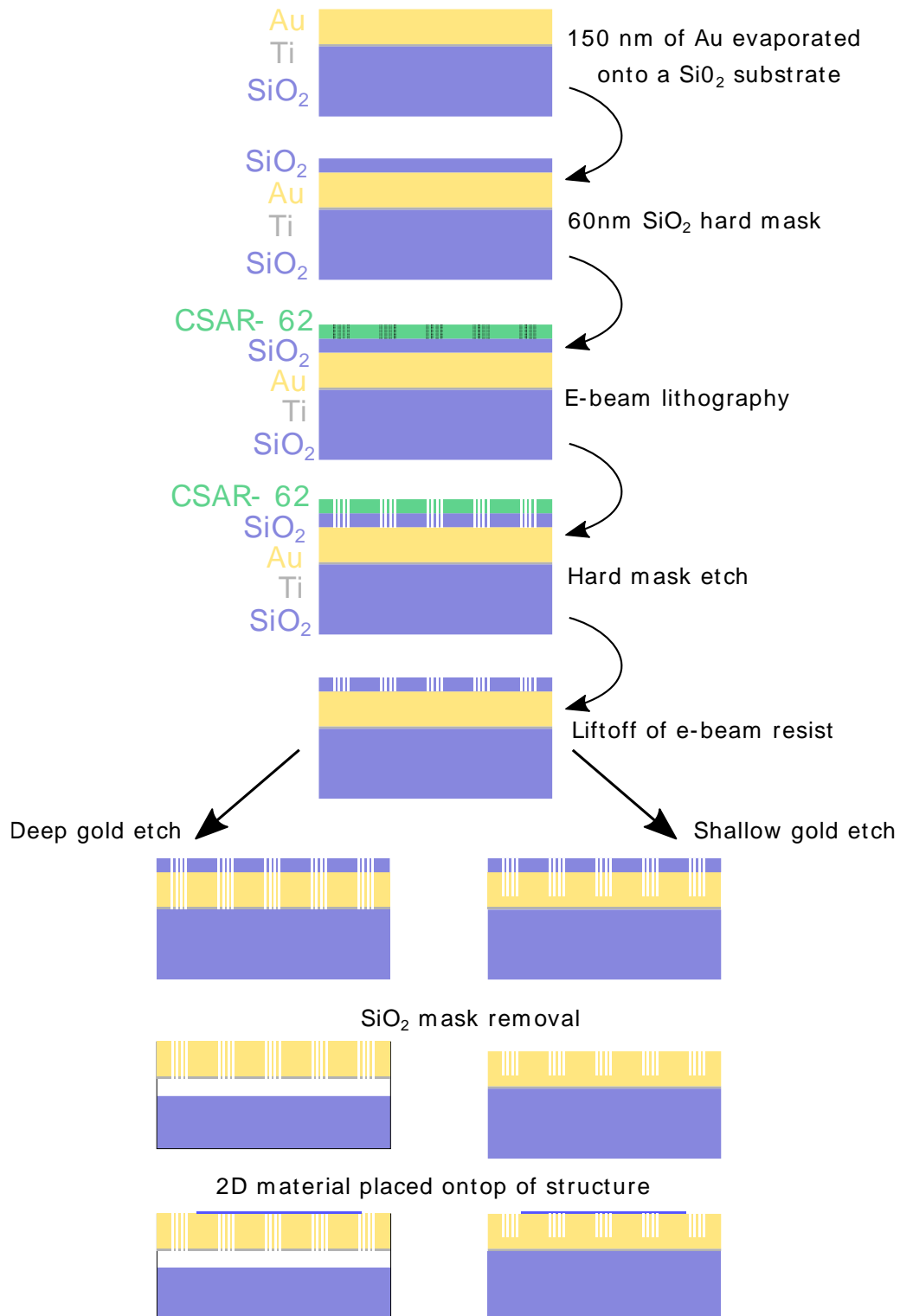


Figure 7.1: Diagram showing the fabrication steps used to create gold plasmonic nano-trenches.

The fabrication process of etching arrays of gold trenches into 150 nm of EBPVD evaporated gold is presented in Figure 7.1. A 60nm hard mask of SiO₂ is deposited on-top of the gold using plasma enhanced chemical vapour deposition (PECVD), followed by a layer of e-beam resist (CSAR 62). The e-beam resist was diluted using anisole by 1:5 and spun at 500 rpm for 5s, 1000 rpm for 5s and 6000 rpm for 60s, creating a uniform resist across the sample with a thickness of approximately 50nm. This is an important step as the plasmon resonance is highly dependent on the width of the trenches,³⁸ the scale of which (10 nm) is pushing the limit of the electron beam lithography (EBL) systems resolution (JEOL-JBX-5500ZD). Therefore, a very thin resist is required so that low dosages can be used to limit proximity effects from scattered electrons; this will provide a much more accurate structure than if a more conventional 80 nm thick resist was used. The CSAR 62 resist was also selected over other EBL resists such as PMMA due to its high dosage sensitivity, overall this allowed dosages < 100 $\mu\text{C}/\text{cm}^2$ to be used and developed successfully. Development itself was performed using o-Xylene for 90s combined with very gentle agitation using an ultrasonic bath to allow the developed resist to be removed more easily from the very small trenches; the sample is then rinsed in IPA to stop further development.

To create the hard mask the e-beam lithography system exposed arrays of parallel trenches with a pitch of 200 nm and varying widths from 8-20 nm. After development the hard mask was then etched for 2 mins in an RIE plasma using a SiO₂ etching recipe consisting of CHF₃ and O₂³⁹.

To etch the gold a highly isotropic yet selective etch was required, as the sidewalls need to be ideally as vertical as possible for optimum plasmon confinement. Work done by Siegfried, et al. [38] suggest that plasmon gap resonance is suppressed in vertical trench depths < 60 nm, and that for an optimal resonance in a 10 nm wide trench, verticality should be maintained for 100 nm. Therefore, to etch the gold a Cl₂ + Ar based plasma was developed for the ICP-RIE based off ICP based recipes from literature^{40,41}. The gas ratio of Cl₂:Ar was 1:3, the Ar provides a deep anisotropic etch whereas the Cl₂ provides selectivity and most importantly combines with Au ions to create volatile compounds which can be easily removed from the plasma. One of the biggest challenges of etching gold is to prevent redeposition onto the surface, due to reactive species not forming a vapour. To prevent this, the chamber was heated to 160°C and a low chamber pressure of 5 mT was maintained throughout the etch. The full etch recipe is given in Table 7.1, the selectivity of etching SiO₂ : Au was 2:5 and the etch rate was 12 nm min⁻¹.

After etching, the SiO₂ can be removed using a buffered oxide etch solution which consists of HF, NH₄F and H₂O in the respective ratio 1:7:12. There is also the possibility to suspend these structures at this point if the ICP-RIE was intentionally used to etch through the gold, due to the Au being deposited on SiO₂. The advantage of suspending the structure is it allows it to be easily removed from the substrate to allow absorption measurements to be performed to find the plasmonic mode.

Figure 7.2 shows SEM and AFM images of some initially fabricated gold nano-trench structures, these trenches were patterned to be 20 nm in width. It can be seen in (a) and (b) that the trenches are wider than expected ~ 40 nm and show a 10-20 nm fluctuation in width. This most likely arose from the EBL step, as this increase in width was also observed in the SiO₂ mask. There are multiple approaches that can be attempted to solve this problem, the most effective would be to use a more sensitive resist to allow lower e-beam dosages thus reducing electron scattering. Carefully optimising the development may also help, as well as performing better proximity correction on the EBL file, to allow more a uniform dosage across the sample.

ICP-RIE Au etch Recipe	
Cl₂	10 sccm
Ar	15 sccm
Chamber pressure	5 mTorr
Strike pressure	50 mTorr
RIE power (strike power)	25 (50) W
ICP power (strike power)	20 (30) W
Chamber Temperature	160°C
DC bias	154 V
Etch rate	12 nm min ⁻¹
Selectivity SiO₂	2:5

Table 7.1: ICP-RIE parameters for slow anisotropic etching of gold with a SiO₂ hard mask

AFM results in (d) demonstrate that the trenches show good verticality, the triangular feature observed is the shape of the tip of the AFM, indicating that for at least 50 nm the trench sidewalls are sufficiently vertical that the AFM cannot detect them. Of course, there is the possibility of overetching, however without some cross-sectional measurements this would be difficult to confirm. It can also be seen that the gold looks rough and there appears to be a lot of grain boundaries. This could potentially be improved by rapidly annealing the gold structures, whilst encapsulated in HSQ to prevent any deformation in the structures shape⁴².

At the time of writing this thesis this is the current point that this work has reached, however the next stage will involve shining light through different widths of trenches to see if we can detect any absorption of the light that might correspond to gap-plasmon modes. This should allow us to perfect the design so the final structure can be fabricated and a WSe₂ flake can be transferred on-top of the gold, along with an epoxy-SIL, ready for low temperature PL measurements.

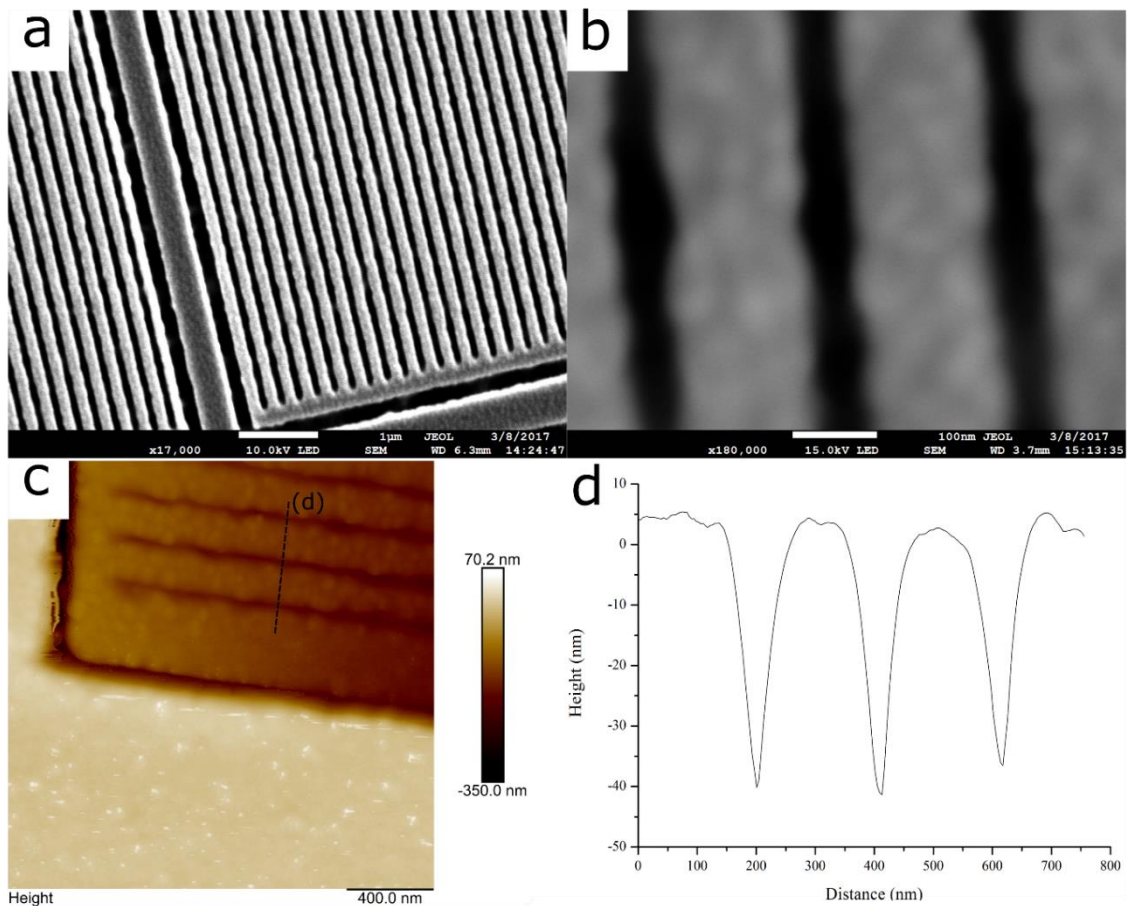
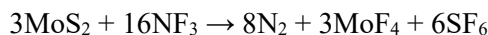
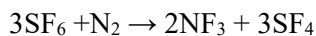


Figure 7.2: Images of fabricated gold trench arrays (**a**, **b**) showing SEM images, (**c**) showing an AFM scan of the same area, and (**d**) showing the height in the highlighted region

6.5.2 Etching TMD's

Transition metal dichalcogenides (TMD's) have highly layer dependent properties; the addition of a single atomic layer on-top of a monolayer is enough to change the band structure from direct to indirect, greatly reducing the intensity of the TMD and significantly shifting its wavelength. For some applications thicker structures can be more preferable, e.g. creating site controlled single photon emitters³⁶. However, most methods used to exfoliate/grow TMD's are inherently random making it difficult to control both the thickness and lateral size of an individual flake. One method that could be used to overcome this is to grow a slightly thick structure (e.g. a bilayer) then controllably etch the flake in a plasma to reduce its thickness⁴³, this can potentially be combined with lithography to create only monolayers in predefined areas. The ability to laterally control the thickness of a TMD through etching could enable some interesting applications, which could be anything from forming large monolayers, to etching lateral heterojunctions.

Xiao, et al. [44] presented a method to etch MoS₂ using an ICP plasma which slowly removes layers in a controllable way without causing ion impact damage to the sheet. The recipe used SF₆ and N₂ to create NF₃ by the following reaction:



In this piece of work we used the above etch chemistry to attempt to etch Tungsten disulphide (WS₂), to monolayer using an ICP-RIE. WS₂ is interesting for this study as its PL tends to be very bright compared to other TMDs^{45,46} such as MoS₂ making it more suitable for devices emitting light.

ICP-RIE WS₂ etch Recipe	
SF₆	0.5 sccm
N₂	35 sccm
Chamber pressure	30 mTorr
Strike pressure	50 mTorr
RIE power (strike power)	2 (10) W
ICP power (strike power)	15 (150) W
Chamber Temperature	13°C
DC bias	0 V
Etch rate	0.1 layer min ⁻¹

Table 7.2: ICP-RIE parameters for WS₂ bilayer to monolayer etch

Initial studies using an ICP-RIE showed that the etch rate of WS₂ could be reduced to a remarkably slow rate of 0.1 layers/min, simply by controlling the flow of nitrogen. The parameters for this etch on the ICP-RIE are shown in Table 7.2, the selectivity of the etch over the SiO₂ substrate is not known, however despite this no change in SiO₂ thickness has so far been observed.

A WS₂ bilayer flake etched in this way is presented in Figure 7.3, where the flakes photoluminescence and physical appearance under a microscope is presented both before (a) and after (b) etching. The etching of a monolayer is clearly visible in the PL maps, with the monolayer in the top left of (a) being etched away in (b), whilst the bilayer gets substantially brighter due to it being reduced to monolayer and gaining a more direct bandgap. This shift to monolayer is clearly evident in the individual PL spectra shown in (c), with the increase in intensity accompanied by a shift in wavelength to just under 630 nm, very similar to CVD grown monolayers in literature⁴⁷. This is also supported by the Raman spectra in (d) which again matches what has been observed for bilayer/monolayer in literature⁴⁸. However, when observing the intensity between (a) and (b) it is

clear that the etched monolayer's PL is only half as intense as the original monolayer observed in the top left of (a). There could be many reasons for this, such as the plasma starting to etch away parts of the monolayer sheet, or defects being created in the sheet due to the plasma which then acts as sources of non-radiative recombination.

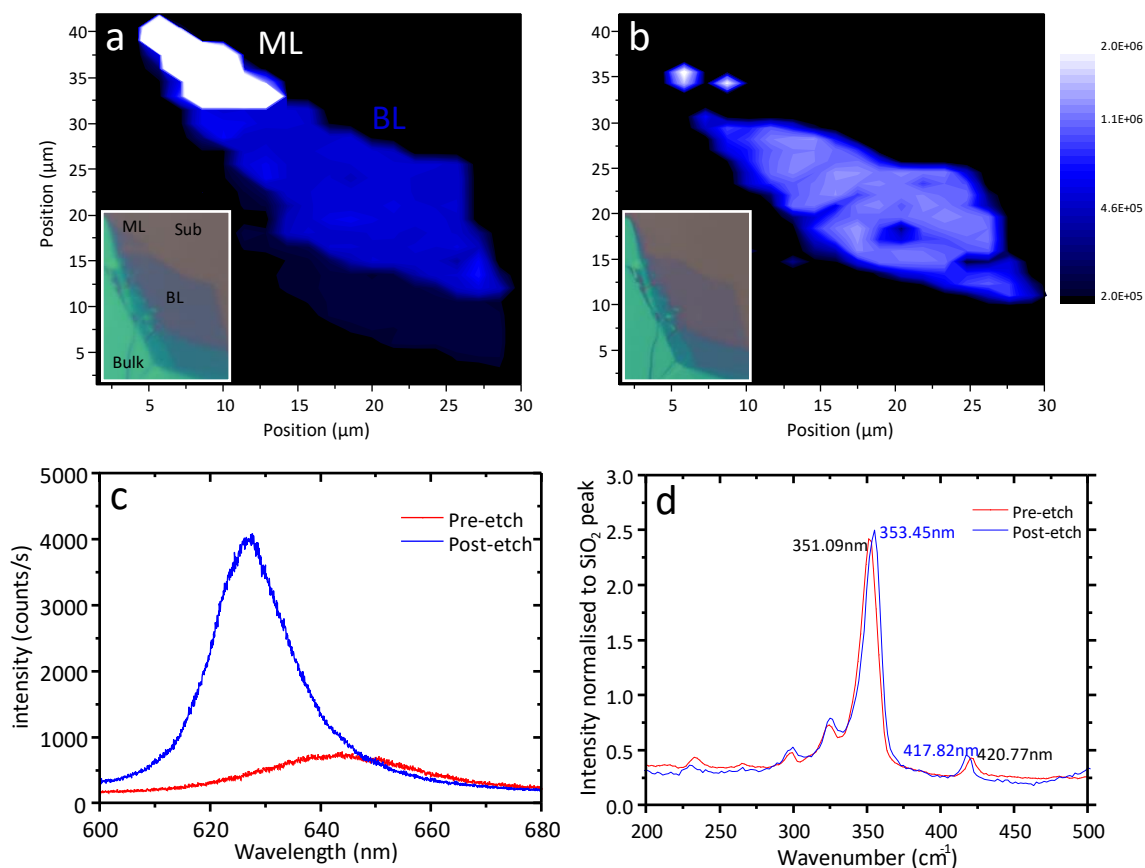


Figure 7.3: The top row show PL maps and their microscope image (inset) of a bilayer flake of WS₂ pre-etch (a) and post-etch (b). The bottom row shows the PL spectra (c) and Raman spectra (d) of the flake, both before and after etching.

To fully understand the effect etching has on the monolayer, AFM measurements were performed on several different bilayer WS₂ flakes that were etched to monolayer; one of these scans is presented in Figure 7.4. In this AFM image it is clear that the plasma etch is causing the deposition of an unknown substance onto the substrate. More detailed scans on the monolayer suggest that the roughness has increased a similar amount to the substrate suggesting that this deposition is uniform across the sample. Etching performed on MoS₂ using the same chemistry and machine did not show any traces of this deposition, suggesting that tungsten might be the source of this deposition. Tungsten hexafluoride has a vapour pressure under room temperature so can be ruled out as the source of the deposition⁴⁹, however tungsten nitride has a vapour pressure of 646°C⁵⁰ and is much

more likely as the etch recipe has an excess of nitrogen in the chamber. To remove this a change to the etch gasses are required, which likely involves reducing the nitrogen and increasing the fluorine content of the plasma to promote the tungsten to react with the fluorine to form WF_6 which can be more easily removed, however this will most likely dramatically increase the etch rate. An alternative approach is to add a small amount of oxygen into the plasma to promote WOF_4 formation, which from literature has a vapour pressure of $187.5^\circ C^{49}$, which can be reached in the ICP-RIE. If the deposition issue can be solved this etch recipe could be a valuable tool for the processing of WS_2 , with lateral heterostructures of monolayer-bilayer possible by simple lithography and plasma etch techniques. These structures have shown increased amount of interest recently⁵¹⁻⁵⁴ due to their abrupt interfaces having interesting properties such as type-I quantum wells. It may therefore be possible to create some innovative new structures such as lateral resonant tunnelling diodes (RTD's), out of WS_2 by utilising this etching method.

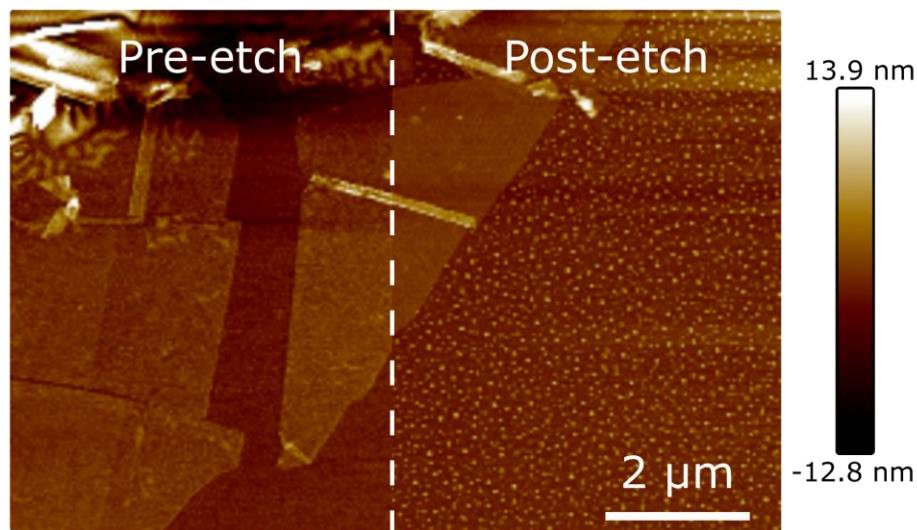


Figure 7.4: AFM scans of a bilayer before (left) and after (right) being etched to a monolayer

6.6 References

- 1 Withers, F. *et al.* Light-emitting diodes by band-structure engineering in van derWaals heterostructures. *Nature Mater* **14**, 301 - 306, (2015).
- 2 Buscema, M., Steele, G. A., van der Zant, H. S. J. & Castellanos-Gomez, A. The effect of the substrate on the Raman and photoluminescence emission of single-layer MoS₂. *Nano Research* **7**, 561-571, (2014).
- 3 Palacios-Berraquero, C. *et al.* Atomically thin quantum light-emitting diodes. *Nat. Commun.* **7**, 12978, (2016).
- 4 Amani, M. *et al.* Near-unity photoluminescence quantum yield in MoS₂. *Science* **350**, 1064, (2015).
- 5 Gauck, H., Gfroerer, T. H., Renn, M. J., Cornell, E. A. & Bertness, K. A. External radiative quantum efficiency of 96% from a GaAs / GaInP heterostructure. *Applied Physics A* **64**, 143-147, (1997).
- 6 Schnitzer, I., Yablonovitch, E., Caneau, C. & Gmitter, T. J. Ultrahigh spontaneous emission quantum efficiency, 99.7% internally and 72% externally, from AlGaAs/GaAs/AlGaAs double heterostructures. *Applied Physics Letters* **62**, 131-133, (1993).
- 7 Gisin, N., Ribordy, G., Tittel, W. & Zbinden, H. Quantum cryptography. *Reviews of Modern Physics* **74**, 145-195, (2002).
- 8 Presolski, S. & Pumera, M. Covalent functionalization of MoS₂. *Materials Today* **19**, 140-145, (2016).
- 9 Voiry, D. *et al.* Covalent functionalization of monolayered transition metal dichalcogenides by phase engineering. *Nat Chem* **7**, 45-49, (2015).
- 10 Sobhani, A. *et al.* Enhancing the photocurrent and photoluminescence of single crystal monolayer MoS₂ with resonant plasmonic nanoshells. *Applied Physics Letters* **104**, 031112, (2014).
- 11 Wang, Z. *et al.* Giant photoluminescence enhancement in tungsten-diselenide-gold plasmonic hybrid structures. *Nat Commun* **7**, (2016).
- 12 Liu, X. *et al.* Strong light-matter coupling in two-dimensional atomic crystals. *Nat Photon* **9**, 30-34, (2015).
- 13 Gan, X. *et al.* Controlling the spontaneous emission rate of monolayer MoS₂ in a photonic crystal nanocavity. *Applied Physics Letters* **103**, 181119, (2013).
- 14 Noori, Y. J. *et al.* Photonic Crystals for Enhanced Light Extraction from 2D Materials. *ACS Photonics* **3**, 2515-2520, (2016).
- 15 Woodhead, C. S. *et al.* Increasing the light extraction and longevity of TMDC monolayers using liquid formed micro-lenses. *2D Materials* **4**, 015032, (2017).
- 16 Gao, J. *et al.* Aging of Transition Metal Dichalcogenide Monolayers. *ACS Nano* **10**, 2628-2635, (2016).

- 17 Blodgett, K. B. Films Built by Depositing Successive Monomolecular Layers on a Solid Surface. *Journal of the American Chemical Society* **57**, 1007-1022, (1935).
- 18 Dimastrodonato, V., Mereni, L. O., Young, R. J. & Pelucchi, E. Growth and structural characterization of pyramidal site-controlled quantum dots with high uniformity and spectral purity. *physica status solidi (b)* **247**, 1862-1866, (2010).
- 19 Trojak, O. J., Suk In Park, Jin Dong Song & Sapienza, L. Metallic nanorings for broadband, enhanced extraction of light from solid-state emitters. (2017).
- 20 Koperski, M. *et al.* Single photon emitters in exfoliated WSe₂ structures. *Nat Nano* **10**, 503-506, (2015).
- 21 Srivastava, A. *et al.* Optically active quantum dots in monolayer WSe₂. *Nat Nano* **10**, 491-496, (2015).
- 22 Eisaman, M. D., Fan, J., Migdall, A. & Polyakov, S. V. Invited Review Article: Single-photon sources and detectors. *Review of Scientific Instruments* **82**, 071101, (2011).
- 23 Serrels, K. A. *et al.* Solid immersion lens applications for nanophotonic devices. *NANOP* **2**, 021854-021829, (2008).
- 24 Moehl, S., Zhao, H., Don, B. D., Wachter, S. & Kalt, H. Solid immersion lens-enhanced nanophotoluminescence: Principle and applications. *J. Appl. Phys.* **93**, 6265-6272, (2003).
- 25 Yan, T., Qiao, X., Liu, X., Tan, P. & Zhang, X. Photoluminescence properties and exciton dynamics in monolayer WSe₂. *Applied Physics Letters* **105**, 101901, (2014).
- 26 Huang, J., Hoang, T. B. & Mikkelsen, M. H. Probing the origin of excitonic states in monolayer WSe₂. *Scientific Reports* **6**, 22414, (2016).
- 27 Eda, G. *et al.* Photoluminescence from Chemically Exfoliated MoS₂. *Nano Letters* **11**, 5111-5116, (2011).
- 28 Tosun, M. *et al.* Air-Stable n-Doping of WSe₂ by Anion Vacancy Formation with Mild Plasma Treatment. *ACS Nano* **10**, 6853-6860, (2016).
- 29 Li, J. *et al.* Tuning the optical emission of MoS₂ nanosheets using proximal photoswitchable azobenzene molecules. *Applied Physics Letters* **105**, 241116, (2014).
- 30 Podzorov, V., Gershenson, M. E., Kloc, C., Zeis, R. & Bucher, E. High-mobility field-effect transistors based on transition metal dichalcogenides. *Applied Physics Letters* **84**, 3301-3303, (2004).
- 31 Allain, A. & Kis, A. Electron and Hole Mobilities in Single-Layer WSe₂. *ACS Nano* **8**, 7180-7185, (2014).
- 32 Mouri, S., Miyauchi, Y. & Matsuda, K. Tunable Photoluminescence of Monolayer MoS₂ via Chemical Doping. *Nano Letters* **13**, 5944-5948, (2013).
- 33 Scalise, E., Houssa, M., Pourtois, G., Afanas'ev, V. & Stesmans, A. Strain-induced semiconductor to metal transition in the two-dimensional honeycomb structure of MoS₂. *Nano Research* **5**, 43-48, (2012).
- 34 Amin, B., Kaloni, T. P. & Schwingenschlogl, U. Strain engineering of WS₂, WSe₂, and WTe₂. *Rsc Adv* **4**, 34561-34565, (2014).

- 35 Corey, J. *et al.* MoS₂ monolayers on nanocavities: enhancement in light–matter interaction. *2D Materials* **3**, 025017, (2016).
- 36 Branny, A., Kumar, S., Proux, R. & Gerardot, B. D. Deterministic strain-induced arrays of quantum emitters in a two-dimensional semiconductor. **8**, 15053, (2017).
- 37 Duan, H., Hu, H., Kumar, K., Shen, Z. & Yang, J. K. W. Direct and Reliable Patterning of Plasmonic Nanostructures with Sub-10-nm Gaps. *ACS Nano* **5**, 7593-7600, (2011).
- 38 Siegfried, T., Ekinici, Y., Martin, O. J. F. & Sigg, H. Gap Plasmons and Near-Field Enhancement in Closely Packed Sub-10 nm Gap Resonators. *Nano Letters* **13**, 5449-5453, (2013).
- 39 Metzler, M. *Reactive Ion Etch (RIE) of Silicon Dioxide (SiO₂) with Trifluoromethane and Oxygen (CHF₃/O₂)*, <http://repository.upenn.edu/scn_tooldata/38/> (2016).
- 40 Green, T. A. Gold etching for microfabrication. *Gold Bulletin* **47**, 205-216, (2014).
- 41 Efremov, A. M., Kim, D.-P. & Kim, C.-I. Etching characteristics and mechanism of Au thin films in inductively coupled Cl₂/Ar plasma. *Journal of Vacuum Science & Technology A: Vacuum, Surfaces, and Films* **21**, 1837-1842, (2003).
- 42 Bosman, M. *et al.* Encapsulated Annealing: Enhancing the Plasmon Quality Factor in Lithographically–Defined Nanostructures. *Scientific Reports* **4**, 5537, (2014).
- 43 Liu, Y. *et al.* Layer-by-Layer Thinning of MoS₂ by Plasma. *ACS Nano* **7**, 4202-4209, (2013).
- 44 Xiao, S. *et al.* Atomic-layer soft plasma etching of MoS₂. *Scientific Reports* **6**, 19945, (2016).
- 45 Gutiérrez, H. R. *et al.* Extraordinary Room-Temperature Photoluminescence in Triangular WS₂ Monolayers. *Nano Letters* **13**, 3447-3454, (2013).
- 46 Kaplan, D. *et al.* Excitation intensity dependence of photoluminescence from monolayers of MoS₂ and WS₂/MoS₂ heterostructures. *2D Materials* **3**, (2016).
- 47 McCreary, K. M., Hanbicki, A. T., Jernigan, G. G., Culbertson, J. C. & Jonker, B. T. Synthesis of Large-Area WS₂ monolayers with Exceptional Photoluminescence. **6**, 19159, (2016).
- 48 Berkdemir, A. *et al.* Identification of individual and few layers of WS₂ using Raman Spectroscopy. *Scientific Reports* **3**, 1755, (2013).
- 49 Cardinaud, C., Peignon, M.-C. & Tessier, P.-Y. Plasma etching: principles, mechanisms, application to micro- and nano-technologies. *Applied Surface Science* **164**, 72-83, (2000).
- 50 Agency, U. S. E. P. United States Environmental Protection Agency. Tungsten nitride (WN). <<https://comptox.epa.gov/dashboard/dsstoxdb/results?formula=1&isotopes=1&search=NW>> (2017).
- 51 Li, M.-Y. *et al.* Epitaxial growth of a monolayer WSe₂–MoS₂ lateral p-n junction with an atomically sharp interface. *Science* **349**, 524, (2015).
- 52 Guo, Y. & Robertson, J. Band engineering in transition metal dichalcogenides: Stacked versus lateral heterostructures. *Applied Physics Letters* **108**, 233104, (2016).

- 53 Gong, Y. *et al.* Vertical and in-plane heterostructures from WS₂/MoS₂ monolayers. *Nat Mater* **13**, 1135-1142, (2014).
- 54 Duan, X. *et al.* Lateral epitaxial growth of two-dimensional layered semiconductor heterojunctions. *Nat Nano* **9**, 1024-1030, (2014).

Chapter 7

Conclusions

7.1 Conclusions

In this work three different solid-state emitters were studied using micro-photoluminescence. The room temperature emission and near infra-red (NIR) wavelength of each of these emitters, makes them attractive as potential sources of single photons. However, these emitters have relatively low efficiencies; with the quantum dot (QD) samples showing high spectral broadening due to their type-II band alignment, and 2D materials having low internal efficiencies, making individual excitons difficult to observe. Several different techniques such as solid immersion lenses (SILs), aperture masks and micropillars were employed to enhance their light emission, and isolate their individual exciton transitions.

The first type of emitter studied was embedded GaSb/GaAs quantum rings (QR) emitting at 1200 - 1300 nm. These structures have a type-II band alignment with tightly confined holes and more loosely confined electrons in their centre. Isolation of individual exciton transitions in micro-photoluminescence (μ PL) was found to be challenging due to the density and broad emission of these structures. A glass super solid immersion lens (s-SIL) combined with a gold aperture mask was placed onto the surface to increase the numerical aperture, and reduce the excitation and emission area simultaneously. Using these methods individual exciton-like emission with linewidths as small as 200 μ eV were detected at low excitation powers. The observation of individual exciton peaks enabled us to understand their contribution to the peak centre of mass (COM) power dependent blueshift often observed in these structures. It was found that the individual exciton peaks emission does not shift with increasing excitation powers, suggesting that in this range of excitation power (five orders of magnitude) band bending does not provide a major contribution to the observed COM blueshift. Instead the cause is attributed to an increase of the coulomb attraction between the electrons and holes, resulting in an increased confinement, and thus a higher emission energy when the exciton recombines. This agrees with several other papers from literature which all attribute band bending to be a minor effect¹⁻⁴.

The excitons long lifetime in QRs make them an obvious candidate for use in memories, however what might be less obvious is their potential use as an active medium in lasers. The long carrier lifetime in the quantum dots should make it easier to maintain a population inversion relative to a type-I quantum dot, and increases the probability that an exciton recombines via stimulated emission rather than spontaneous emission or a non-radiative process. However, for other optical applications such as single photon sources this low spontaneous emission rate is detrimental to their performance. One method that could be used to improve this would be to grow DBR mirrors both above and below the active region to create a cavity which can then be etched into micropillars. These pillars would have two effects; the first would be to reduce the area of excitation so fewer QDs are excited at once, allowing for an improvement in the isolation of individual exciton lines. The second effect is the cavity should provide a Purcell enhancement in the light emission which should help to reduce the time it takes for the excitons to recombine, reducing the long lifetimes created by the type-II band alignment.

The second emitter studied consisted of an active region containing InAs/GaAs QDs capped with GaAsSb to red-shift emission to 1400 - 1600 nm. They possessed a type-II band alignment similar to the GaSb/GaAs QRs, but with carriers confined in a different way, with electrons being tightly confined in the InAs dot and the holes delocalised in the GaAsSb capping layer. The novel approach in this experiment was to grow an identical active region on both a silicon wafer and on a GaAs wafer, to analyse the effectiveness of these structures on Silicon. The Silicon grown sample contained sets of super lattices called defect filter layers (DFLs) which help to remove dislocations in the crystal that form from the lattice mismatch of GaAs and Silicon. Upon performing macro-PL it was found that the QD peak on Si was observable but reduced in intensity by an order of magnitude compared to the GaAs. This combined with lack of the wetting layer PL peak indicated that some dislocations were still present, but not enough to suppress QD emission.

For the first time, we observed single quantum dot emission at 1500 nm from QDs grown on both Silicon and GaAs substrates. These sharp lines were isolated using 1 μm diameter micropillars, which helped to reduce the number of excited dots by reducing the excitation area. Linewidths from 1 - 5 meV were observed for both the GaAs and the silicon sample, which indicates that the main source of broadening arises from the active region growth rather than from the silicon. However, the silicon peaks were on average broader due to a ten-fold increase in excitation required to produce the same intensity as observed in the GaAs grown sample. Some pillars showed greatly reduced counts, indicating dislocations were present in sufficient number to decrease the radiative recombination of carriers.

These samples had similarities with the GaSb/GaAs QR structures, especially in their power dependent blueshift which showed a very similar pattern. Individual exciton peaks stayed relatively

constant in wavelength when excitation power increased, whereas the ensemble peak strongly blueshifted. It is therefore likely that the main contribution to the blueshift in this structure is also capacitive charging due to the coulomb interaction, but with the electron-electron interaction this time being dominant. From the TEM images in Figure 5.2a it is possible that the GaAsSb cap is loosely confining holes due to the ring like structure that has formed around the dot. This could be providing an environment akin to an inverse QR with the holes being loosely confined in the lobes of this ring, and electrons tightly confined in the centre. Overall these QDs have excellent applications as a light source for quantum telecoms, and show better promise than the QRs due to their C-band emission, and easy integration into Si based QKD on-chip devices⁵. However, individual excitons do need to be better isolated so lifetime and autocorrelation measurements can be performed, allowing their viability as a single photon source can be fully assessed. A more optimised MBE growth of the active region to reduce the QD density would greatly help towards this goal. Additionally, growing DBR's around the active region to create a cavity would help to increase the radiative recombination of carriers through the Purcell effect.

The final solid-state structure studied was a 2D monolayer flake of tungsten diselenide (WSe_2) mechanically exfoliated onto a silicon/silicon dioxide (Si/SiO_2) substrate. This material, like the two previously mentioned QD structures, emits at room temperature. It additionally contains defect states that at low temperature have been shown to exhibit single photon emission. Monolayer WSe_2 has advantages as a light emitter over semiconductor QD systems previously discussed, due to them being fully compatible with silicon, being very cheap and versatile to fabricate, and having unique spin-orbit interactions. However, WSe_2 has a very poor quantum yield with low absorption of light, and omnidirectional emission making it highly inefficient compared to III-V semiconductors. To help solve this issue we attempted to increase the coupling of light into/out of the monolayer using a SIL formed from liquid UV curable epoxy. The fabrication of the SIL in this way does not cause any damage to the monolayer, and helps to protect it from the ambient environment which can cause degradation of the structure and a drop in PL intensity. SILs fabricated on-top of WSe_2 monolayers showed 250-300% improvement in the PL intensity at room temperature, and magnified the monolayer by 1.8x. The wavelength of emission of the WSe_2 was largely unaffected with only a slight blueshift detected, however when applied to MoS_2 a quenching of the PL was observed. It was therefore suggested that the epoxy was either slightly n-doping the material, or was straining the monolayer upon curing. There are many ways addressing this issue; changing the composition of the epoxy may help prevent doping, or if this isn't possible a thin coating with an index matched polymer such as PMMA could be applied before mounting the SIL. Additionally, since performing this work new epoxies with higher refractive indices than used in the above work have become

available, which should greatly increase a SIL's enhancement by focusing a larger solid angle into the collection optics.

Epoxy SILs have great integration potential with any surface; as the epoxy is formed in a liquid state, there is no risk of damage or air gaps when mounting. Their only limitation is the wettability of the surface they are deposited on, as the surface needs to be reasonably hydrophobic to allow high contact angled lenses such as s-SILs to be formed. One way around this limitation might be to treat the surface with a chemical designed to increase hydrophobicity. An example of such a chemical is 1H, 1H, 2H, 2H-Perfluorooctyltriethoxysilane^{6,7} however cheaper substances such as basic fatty acids⁸ could also be used to ensure that the most optimised lens is always dispensed.

Overall this work has presented three different room temperature emitters each with a different emission wavelength in the NIR range. Each material system has the capability to emit single photons, but each suffers from either a poor internal efficiency or spectra too dense to observe individual excitons. For each structure, we presented methods that can be used to overcome these issues, enabling an improvement in the optical PL response. These optical improvements could enable each of these emitters to be integrated into silicon photonic circuitry, to enable on chip technology such as classical networks⁹ as well as QKD¹⁰.

7.2 References

- 1 Müller-Kirsch, L. *et al.* Many-particle effects in type II quantum dots. *Applied Physics Letters* **78**, 1418-1420, (2001).
- 2 Hodgson, P. D. *et al.* Blueshifts of the emission energy in type-II quantum dot and quantum ring nanostructures. *J. Appl. Phys.* **114**, 073519, (2013).
- 3 Young, R. J. *et al.* Optical observation of single-carrier charging in type-II quantum ring ensembles. *Applied Physics Letters* **100**, 082104, (2012).
- 4 Hayne, M. *et al.* Electron localization by self-assembled GaSb/GaAs quantum dots. *Applied Physics Letters* **82**, 4355-4357, (2003).
- 5 Sibson, P. *et al.* Chip-based quantum key distribution. *Nat. Commun.* **8**, (2017).
- 6 Zhang, F. *et al.* Preparation of superhydrophobic films on titanium as effective corrosion barriers. *Applied Surface Science* **257**, 2587-2591, (2011).
- 7 Li, Y., Li, L. & Sun, J. Bioinspired Self-Healing Superhydrophobic Coatings. *Angewandte Chemie International Edition* **49**, 6129-6133, (2010).
- 8 Hu, Z., Zen, X., Gong, J. & Deng, Y. Water resistance improvement of paper by superhydrophobic modification with microsized CaCO₃ and fatty acid coating. *Colloids and Surfaces A: Physicochemical and Engineering Aspects* **351**, 65-70, (2009).
- 9 Nicopoulos, C. *Network-on-chip architectures : a holistic design exploration.* (Dordrecht : Springer, 2009).
- 10 Autebert, C. *et al.* Multi-user quantum key distribution with entangled photons from an AlGaAs chip. *Quantum Science and Technology* **1**, 01LT02, (2016).

Glossary of terms/abbreviations

Active region: An intrinsically doped region of an optical device (usually a laser) where carriers are injected into. The active region usually contains a light emitting semiconductor structure which will capture the carriers where they can recombine to produce photons.

CVD (Chemical Vapour Deposition): A method of growing crystalline materials by forming chemical vapours using a furnace, then channelling these vapours over a substrate allowing them to condense and form triangular crystalline structures.

DFLS (Defect Filter Layers): DFLs are sets of strained superlattices used to reduce the defects in a crystal, by bending propagating dislocations so that they meet and annihilate each other.

Dielectric constant/relative permittivity: A material dependent property that describes the amount of resistance encountered when forming an electric field in a material, relative to a vacuum.

EBL(Electron Beam Lithography): A patterning technique where an electron sensitive resist is exposed to a beam of electrons to create a pattern which has a resolution down to 10nm.

EDX/EDS (Energy-Dispersive X-ray Spectroscopy): A technique used to characterise the elemental composition of a material exciting an atoms by promoting an electron from the inner shell into free space, then observing the elements unique x-ray which it's atom emits due to outer electrons de-exciting into their ground state.

Fermi Level (ϵ_f): The fermi level is a hypothetical electron energy that usually exists in the bandgap, at zero kelvin all the states are filled up to the fermi level.

Fermi-Dirac function ($F(\epsilon)$): This function describes the probability that an electron at a given energy state will be occupied at a given temperature.

GaAs (Gallium Arsenide): A crystalline semiconductor often used as a substrate for III-V MBE growth. Its bluey-black in appearance, very fragile and has a bandgap of 1.424 eV at 300K.

III-V Material: A compound made from elements from group III and V of the periodic table such as GaAs, InAs, AlSb etc.

ME (Mechanical exfoliation): The process of thinning down a large bulk crystal of a 2D material using a piece of adhesive tape, then transferring the layer from the tape onto the desired substrate.

Micropillar: A small cylindrical pillar around a micron is diameter, etched into a semiconductor, and commonly used to create cavities for lasers.

NIR (Near Infra-Red): Electromagnetic radiation at wavelengths between 700 – 2500nm.

Photon: A single particle of light with zero mass, which are the elementary particle of electromagnetism.

Piezo (piezoelectric acuator): A stack of ceramic plates that use their piezoelectric effect to expand in response to being charged. This width change can be submicron, enabling very fine movements of a system.

PL/ μ PL (Photoluminescence): Using light (normally a laser) to create excite a material with a bandgap so it emits light.

QD (Quantum Dot): A small island of semiconductor that is only a few nm in all directions, often embedded in a different semiconductor. This creates an energy well that can confine excitons in all 3 dimensions and give rise to atom-like emission.

QKD (Quantum key distribution): A encryption scheme that uses fundamental quantum mechanics to create a secure key out of a stream of single photons.

QR (Quantum Ring): A quantum dot that has been capped in such a way that in explodes into a ring/doughnut shape. Holes become confined in the lobes of the ring and electrons outside making a spatial separation of carriers and a type-II structure.

QW (Quantum Well): A thin layer of semiconductor only a few nanometres in width sandwiched between two layers of material with a wider bandgap. Carriers can become confined leading to more discrete electronic and optical states.

QY (Quantum Yield): The ratio of the number photons absorbed by the material, to the amount of photons that the material emits.

Si (Silicon): A very highly abundant crystalline group IV semiconductor, used in nearly all modern-day electronics.

SIL/SILs (Solid Immersion Lenses): A small optical component that sits on the surface of a material and enhances the overall numerical aperture of a microscope system.

SPP (Surface plasmon polariton): Electromagnetic waves that travel along the surface of a metal-dielectric interface. They are generated by the coupling of electrical charge in the metal to photons in the air.

TMD (Transition Metal Dichalcogenide): This refers to a material that consists of a lattice of the formula MX_2 formed from a transition metal (M) e.g. Ti, Ta, W; with 2 chalcogen atoms from group VI (X) e.g. S, Se, Te.

θ_c (Contact angle): The internal angle a droplet makes to a surface it is in contact with.